

Rockefeller University

Digital Commons @ RU

Student Theses and Dissertations

2023

The Nanomechanics of Protocadherin 15, A Protein Essential for Human Hearing

Camila M. Villasante

Follow this and additional works at: https://digitalcommons.rockefeller.edu/student_theses_and_dissertations



Part of the Life Sciences Commons



THE NANOMECHANICS OF PROTOCADHERIN 15,
A PROTEIN ESSENTIAL FOR HUMAN HEARING

A Thesis Presented to the Faculty of
The Rockefeller University
in Partial Fulfillment of the Requirements for
the degree of Doctor of Philosophy

by
Camila M. Villasante
September 2023

© Copyright by Camila M. Villasante (2023)

The nanomechanics of protocadherin 15, a protein essential for human hearing

Camila M. Villasante
The Rockefeller University (2023)

Mechanical force controls the opening and closing of mechanotransductive ion channels atop the hair bundles in the inner ear. A mechanical element called the gating spring modulates the mechanotransduction channel's open probability by changing the force transmitted to the channels. The molecular identity of the gating spring is yet unconfirmed, but a leading candidate is the filamentous tip link connecting the mechanotransduction channel to the tallest neighboring stereocilium. The tip link is essential to mechanotransduction: when it is broken, mechanotransduction is abolished, and when it is allowed to regenerate, mechanotransduction returns. Each tip link comprises four protein molecules: a dimer of protocadherin 15 and a dimer of cadherin 23, both of which are stabilized by Ca^{2+} binding. Further underscoring the role of the tip link in hearing, there are numerous mutations of its constituent proteins that result in deafness. My thesis work has focused on protocadherin 15, the lower portion of the tip link that connects at its C-terminus to the mechanotransduction channel. I was interested in answering several questions: does protocadherin 15 have the appropriate properties to be a component of the gating spring? What factors control its mechanical response? What is its stiffness? How does it soften under force? And how do these answers change in the case of a deafness-causing mutation in protocadherin 15? In order to answer these questions, I used an optical-trap system with sub-nanometer spatial resolution and microsecond temporal resolution to investigate the mechanics of protocadherin 15 at a single-molecule level. To augment this approach I also undertook electron microscopic studies to investigate the structure of wildtype and mutated protocadherin 15. I found that both the mechanics and structure of protocadherin 15 are dependent on Ca^{2+} and that protocadherin 15 undergoes limited unfolding at a physiological level of Ca^{2+} . My

experimentally determined stiffness for protocadherin 15 accords with published values of the gating spring's stiffness, which implies that protocadherin 15 is able to modulate its stiffness without undergoing large unfolding events in physiological Ca^{2+} conditions. In the case of a point mutation that causes non-syndromic hearing loss, the structure of protocadherin 15 is more conformationally heterogeneous, and the protein undergoes frequent unfolding events at all levels of Ca^{2+} . The frequent unfolding events suggest that the mutated protocadherin 15 has lost the ability to maintain appropriate tension under physiological forces, which could prevent the proper opening of the mechanotransduction channel and result in deafness for those with this mutation. This work shows that the maintenance of appropriate tension in the gating spring is critical to the appropriate conveyance of force to the mechanotransduction channel.

To my family

ACKNOWLEDGMENTS

I first want to thank my parents. To my mom I owe the beginnings of my interest in science, born out of her stories studying infectious diseases in the jungles of Indonesia, the mountains of Perú, and the deserts of Egypt. To my dad I owe a desire to think about problems creatively. Thank you both for supporting me always. I also want to thank Denis, who makes every day happier, no matter how my experiments go. Thank you for believing in me always.

In college I became interested in biophysics, a field which had seemed intimidating to me at the outset. I would like to thank Drs. Carolyn Fitch and Bertrand García-Moreno for encouraging me to take a leap of faith and switch majors. I would also like to thank Drs. Hesam Motlagh, James Rives, and Joseph Rehfus for mentoring me in the laboratory and getting me interested in the wonderful world of optical tweezers.

At Rockefeller, the environment in the Hudspeth laboratory has been instrumental to my growth (and happiness) as a scientist. I first want to thank Dr. Tobias Bartsch, who not only built the photonic force microscope used in this text but was also an excellent teacher and rigorous scientist who I emulate. Thank you for always taking the time to answer my questions. I am very grateful. Along with me in those early days were Drs. Daniel Firester and Ahmed Touré, whose presence made the trials and tribulations back then less tedious. I would like to thank Brian Fabella, who not only always knew how to fix software and machine problems (start by turning it off and on again), but has also been a great friend. Upstairs, both Masha Vologodskaja and Lana Norris kept us all in check, functioning, and in budget. Thank you both for everything you do.

About a year and a half before the end of my PhD, graduate student Xinyue Deng joined the group and became interested in this project. She has not only been a wonderful colleague—she is a deep thinker and excellent scientist—but a true friend as well. Thank you for your insights, and I am excited to see what you will do during your PhD.

To the downstairs lab crew, in particular Drs. Rodrigo ‘Gogui’ Alonso, Francesco Gianoli, and Yuval Edri, thank you for your help along the way, for keeping things light-hearted, and for your friendship.

I am grateful for the scientific insights and friendship of the upstairs lab crew, in particular Emily Atlas, Nicolas Vélez-Angel, Rohan Roy, and Caleb Reagor. Thank you for helping me troubleshoot things and giving great advice.

During my PhD I forayed into the world of transmission electron microscopy, so I thank Drs. Amalia Pasolli and Anurag Sharma from the Electron Microscopy Resource Center on campus for their patient guidance using the TEM.

I also want to thank Vadim Sherman from the High Energy Physics Instrument Shop, who manufactured the precision-machined parts I used in my experiments.

I would like to thank Dr. Gilman Dionne at Columbia University for assisting with designing the location of the cysteine residues discussed in Chapter 5.

I am very grateful for being able to work with Dr. Joel Cohen over the past year. Joel has been an incredibly insightful presence, bringing his expertise in population genetics and statistics into this project to much benefit. Joel, thank you for always asking great questions and making me think more deeply.

To my committee members—Drs. Olga Boudker, Shixin Liu, and Eric Siggia—thank you for your guidance throughout these past years. I appreciate your insights and questions. I particularly want to thank my external examiner, Dr. Marcos Sotomayor, for making the journey from Ohio to be here in person for my defense.

I want to thank the MD-PhD program administration for their support over the years, in particular Dr. Catharine Boothroyd for always knowing the answer and for making things run, and also Drs. Katherine Hsu, Olaf Andersen, and Benjamin Levitt, as well as Hanna Silvast and Renee Horton, for all that they do for the program. Thank you also to the MD-PhD entering class of 2017—you know who you are—for making this long journey a fun one. Additionally I want to thank the Rockefeller Dean’s Office staff, in particular Marta Delgado, Kristen Cullen, Tasnia Islam, and Mercedes Harris.

Last but not least, I want to thank Jim for everything over the past four years. I remember becoming interested in the group after hearing a lecture by Jim while in medical school. I was not only impressed by the science but also the way that Jim *talked* about the science, and I wanted to be able to talk like him. So, Jim, thank you for teaching me how to better speak and write about science. Your ‘Jim-isms’ will always follow me wherever I go. Thank you for also teaching me how to be a better scientist and how to think creatively about experiments—I hope to one day know a small portion of all of the science, mathematics, medicine, *etc.* that you know. And, of course, thank you for instilling in me a love of the New York Times crossword. I hope to one day be able to figure out the Thursday trick in my head as you can.

TABLE OF CONTENTS

ACKNOWLEDGMENTS	iv
TABLE OF CONTENTS	vii
LIST OF FIGURES	x
LIST OF ABBREVIATIONS	xii
CHAPTER 1. Introduction	1
1.1 Introduction to mammalian hearing	1
1.2 Hair cells are the sensory receptors of sound	2
1.3 Fast and slow adaptation	5
1.4 The mechanotransduction channel complex	5
1.5 The gating spring	7
1.6 The tip link	9
1.6.1 Protocadherin 15	11
1.7 Deafness mutations in PCDH15	13
1.7.1 Usher syndrome	13
1.7.2 Non-syndromic deafness.....	14
1.8 Optical tweezers	14
CHAPTER 2. The photonic force microscope	19
2.1 Experimental apparatus	19
2.2 Position detection	24
2.3 A freely diffusing particle	26
2.4 Motion of a particle in an optical trap	26
2.5 Calibration of the position detector	27
2.6 Force production and calibration of the force-producing laser	29
2.7 Considerations for the molecular anchors	31
2.8 Thermal force probing	36
2.9 Stiffness and behavior of the molecular anchors alone	40
2.10 Materials and methods	41
2.10.1 Pedestal-bead functionalization	41
2.10.2 Sample preparation for single-molecule experimentation	43
2.10.3 Photonic-force microscope	45
2.10.4 Force-ramp experiments	47
2.10.5 Control of non-specific bead interactions	48

2.10.6 Determination of the zero position of extension	49
2.10.7 Statistics of tether formation	49
2.10.8 Identifying conformational changes	50
CHAPTER 3. Ca²⁺ sensitivity of PCDH15 under physiological forces	51
3.1 Previous work: Monomeric PCDH15 exhibits Ca²⁺ dependence	51
3.2 Construction of dimeric PCDH15	55
3.3 Materials and methods	56
3.3.1 Plasmid design	56
3.3.2 Protein purification	56
3.3.3 Negative staining transmission electron microscopy	58
3.3.4 Fitting force ramp data using a saturation model with an enthalpic stiffness term	58
3.3.5 Calculation of the enthalpic stiffness	59
3.4 Results	60
3.4.1 Transmission electron microscopy studies of PCDH15 across three representative Ca ²⁺ concentrations	60
3.4.2 PCDH15 at saturating Ca ²⁺	63
3.4.3 PCDH15 at a physiological Ca ²⁺ concentration	67
3.4.4 PCDH15 in the absence of Ca ²⁺	69
3.4.5 Enthalpic stiffness of PCDH15	72
CHAPTER 4. Mechanics of a PCDH15 non-syndromic hearing loss mutation	74
4.1 Background	74
4.2 Materials and methods	77
4.2.1 Plasmid design	77
4.3 Results	77
4.3.1 Negative-staining transmission electron microscopic studies of PCDH15 V507D	77
4.3.2 PCDH15 V507D at a saturating level of Ca ²⁺	79
4.3.3 PCDH15 V507D at a physiological concentration of Ca ²⁺	83
4.3.4 PCDH15 V507D in the absence of Ca ²⁺	84
4.3.5 Enthalpic stiffness of PCDH15 V507D	87
CHAPTER 5. Investigations into the mechanism of tension regulation in PCDH15	89
5.1 Background	89
5.2 Materials and methods	91
5.2.1 Plasmid design of monomeric PCDH15 with disulfide bonds in each EC domain	91
5.2.2 Plasmid design of shortened monomeric PCDH15	91
5.3 A monomeric PCDH15 construct to probe the role of EC domain unfolding	92

5.4 Creation of a shortened PCDH15 construct to explore the role of EC domain unfolding.....	94
CHAPTER 6. Discussion of results	98
6.1 Comparing the behavior of wild-type and V507D PCDH15	98
6.1.1 Saturating Ca ²⁺	98
6.1.2 Physiological Ca ²⁺	103
6.1.3 Absence of Ca ²⁺	108
6.2 Deafness-causing mutations in the tip link and therapeutic strategies	112
6.3 Proposed mechanism of deafness with PCDH15 V507D	114
BIBLIOGRAPHY	118
APPENDIX A: Additional completed works.....	130

LIST OF FIGURES

Figure 1. The mechanotransduction of sound occurs in the cochlea, at the level of the hair cells.....	2
Figure 2. The structure of the hair bundles allows for mechanotransduction to occur when the bundle is deflected towards its tallest edge.	4
Figure 3. The mechanotransduction complex comprises several proteins.....	7
Figure 4. An elastic gating spring controls the opening of the mechanotransductive ion channels atop each stereocilium.	8
Figure 5. The tip link comprises protocadherin 15 and cadherin 23, two Ca ²⁺ - binding cadherin family proteins.....	10
Figure 6. The mechanism of optical trapping depends on the particle size.....	16
Figure 7. Optical trap and illustrative results.....	21
Figure 8. Illustrative force stimulus and position traces.	23
Figure 9. Position detection by a quadrant photodiode.	25
Figure 10. Position detector sensitivities.	28
Figure 11. Force is produced by displacing the force-producing optical trap and modulating its spring constant.	30
Figure 12. Apparatus and control experiments.....	35
Figure 13. Diffusion of a probe bead tethered by molecular anchors.....	37
Figure 14. Thermal force probing.	39
Figure 15. Behavior of the molecular anchors in the absence of PCDH15.	41
Figure 16. Optical beam paths of the photonic force microscope.	47
Figure 17. Creation of monomeric PCDH15.....	52
Figure 18. The behavior of monomeric PCDH15 was Ca ²⁺ -dependent.....	54
Figure 19. A PCDH15 construct to ensure proper force distribution during optical trap experiments.	55
Figure 20. Transmission electron microscopy of PCDH15 dimers revealed structural differences across Ca ²⁺ concentrations.....	62
Figure 21. Summary of the response of dimeric PCDH15 to physiological forces across three important Ca ²⁺ concentrations.....	64
Figure 22. A saturation model with an enthalpic stiffness term can be used to fit segmented cycles to determine the size of unfolding events.	66
Figure 23. PCDH15 exhibited numerous unfolding behaviors across relevant Ca ²⁺ concentrations.	71
Figure 24. The V507D hearing loss mutation is at the site of a highly conserved valine in a β -sheet in EC5.....	76
Figure 25. Transmission electron microscopy of PCDH15 V507D showed a high degree of conformational heterogeneity across three important Ca ²⁺ concentrations.....	79
Figure 26. PCDH15 V507D exhibited rich unfolding events across relevant Ca ²⁺ concentrations.	82
Figure 27. PCDH15 V507D displayed a variety of unfolding events across important concentrations of Ca ²⁺	86
Figure 28. The inter-domain linker regions have differential Ca ²⁺ -binding properties. ...	90

Figure 29. Creation of a monomeric PCDH15 construct with internal disulfide bonds in each EC domain.	93
Figure 30. TEM showed that the monomeric PCDH15 construct with internal disulfide bonds behaved in unexpected ways.	94
Figure 31. Proposed shortened constructs to avoid self-circularization.	96
Figure 32. Comparison of wild-type and V507D PCDH15 at a saturating level of Ca ²⁺	99
Figure 33. PCDH15 V507D at a saturating level of Ca ²⁺ was more extensible and unfolded more frequently than the wild type.	101
Figure 34. Wild-type PCDH15 underwent smaller magnitudes of unfolding events at saturating Ca ²⁺ compared to V507D.	103
Figure 35. At a physiological level of Ca ²⁺ , both the wild-type and V507D PCDH15 showed separation between the strands of the dimer on TEM.	104
Figure 36. At a physiological concentration of Ca ²⁺ , V507D unfolded more frequently than the wild-type PCDH15.	105
Figure 37. PCDH15 V507D underwent a larger variety and a higher magnitude of unfolding events at a physiological Ca ²⁺ compared to the wild type.	107
Figure 38. TEM imaging showed that both wild-type and V507D PCDH15 were conformationally heterogenous in the absence of Ca ²⁺	108
Figure 39. In the absence of Ca ²⁺ , both the wild-type and V507D PCH15 exhibited a rich variety of unfolding behavior, though V507D was much more extended at baseline than the wild type.	110
Figure 40. Wild-type PCDH15 had smaller magnitudes of unfolding events in the absence of Ca ²⁺ compared to V507D.	111
Figure 41. Proposed mechanism of deafness in PCDH15 V507D.	115

LIST OF ABBREVIATIONS

CDH23: Cadherin 23
DFNB23: Non-syndromic autosomal recessive deafness type 23
EC: Extracellular cadherin
IHC: Inner hair cell
LHFPL5: Lipoma HMGIC fusion partner-like 5
MET: Mechanotransduction
MSD: Mean squared displacement
OHC: Outer hair cell
PCDH15: Protocadherin 15
PFM: Photonic force microscope
PICA: PCDH15-interacting channel-associated
QPD: Quadrant photodiode
TEM: Transmission electron microscopy
TMC: Transmembrane channel-like protein
TMIE: Transmembrane inner ear-expressed protein
USH1F: Usher syndrome type 1F

CHAPTER 1. Introduction

1.1 Introduction to mammalian hearing

When sound waves travel through the air to the ear, they first enter the external ear canal and reverberate on the tympanic membrane, resulting in movement in the middle ear's three ossicles: the malleus, incus, and stapes. The stapes directly contacts the oval window of the cochlea, one of the sensory organs of the inner ear (Figure 1A). The cochlea is a snail-shaped structure containing the machinery that transduces sound stimuli into neural signals. The cochlea comprises three compartments: the scala vestibuli, the scala media, and the scala tympani (Figure 1B). When the stapes stimulates the oval window, the basilar membrane separating the scala media and the scala tympani is stimulated. The basilar membrane serves as a base for the organ of Corti, which contains the sensory receptors of hearing. The resulting displacement pattern on the basilar membrane takes the form of a traveling wave, which progresses from the base to the apex of the cochlea. The wave reaches a maximal amplitude at a particular location along the basilar membrane that is most sensitive to that particular characteristic frequency. The cochlea is organized in a tonotopic manner, with locations at its base being most sensitive to high frequencies (up to 20 kHz), and the area at its apex being most sensitive to low frequencies (as low as 20 Hz)¹ (Figure 1C).

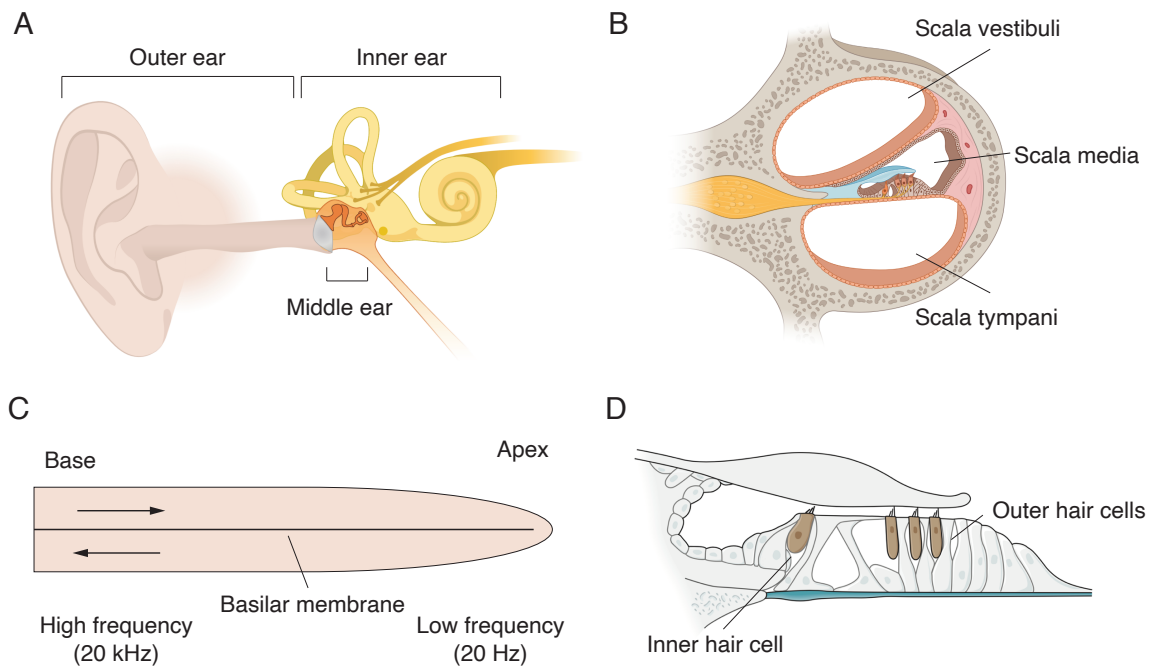


Figure 1. The mechanotransduction of sound occurs in the cochlea, at the level of the hair cells.

(A) Sound enters the ear through the external auditory meatus before hitting the tympanic membrane and resulting in the movement of the middle ear ossicles. When it stimulates the oval window of the cochlea in the inner ear, the stapes then transforms the sound wave in air into a traveling fluid wave. (B) The cochlea comprises three fluid-filled compartments: the scala vestibuli, scala media, and scala tympani. The organ of Corti is located in the endolymph-filled scala media. (C) The traveling wave enters the base of the cochlea at the oval window and travels to the apex. The base of the cochlea is most sensitive to high frequencies, whereas the apex is most attuned to low frequencies. (D) Within the organ of Corti lie the hair cells, the sensory receptors of hearing. There is one row of inner hair cells and three rows of outer hair cells. *Figures adapted from BioRender and Principles of Neural Science.*

1.2 Hair cells are the sensory receptors of sound

Within the organ of Corti are two types of hair cells: a single row of inner hair cells, which are responsible for transducing sound stimuli into neural signals, and three rows of outer hair cells, which amplify the incoming sound stimuli (Figure 1D). The hair bundles of inner hair cells are arranged linearly whereas those of outer hair

cells have a V-shape (Figure 2A). The inner hair cells are predominantly innervated by afferent nerve fibers and the outer hair cells by efferent fibers. A hair cell is called so due to its hair bundle, a cluster of tens to hundreds of actin-filled stereocilia protruding from the cell's apical surface. The stereocilia within the hair bundle are organized in order of increasing height: at the front of the hair bundle reside the shortest stereocilia, and the rows proceed in order of increasing height as they progress towards the back of the hair bundle, where the tallest stereocilia stand (Figure 2B). In addition, in immature hair cells there is a kinocilium at the tallest edge of the hair bundle, but it recedes by the time hair cell maturation is complete¹. Within each stereocilium is a bundle of crosslinked actin fibers, which serve to stiffen the stereocilium. When stimulated, the stereocilia within a hair bundle pivot as a unit, in part due to the basal tapering of each stereocilium as it inserts into the hair cell apical surface, but also due to lateral links that join adjacent stereocilia¹.

The opening of the mechano-electrical transduction (MET) channel permits the influx of cations from the endolymphatic fluid surrounding the hair bundles into the hair cell. At rest, about 10 - 50 % of these channels are open. When a hair bundle is stimulated by being pushed towards its tall edge, more channels are opened, and the additional influx of cations depolarizes the hair cell (Figure 2C). The current is predominantly carried by K^+ ions. When the hair bundle is instead pushed towards its short edge, the channels close, resulting in hyperpolarization of the cell. The relationship of the receptor potential of the hair cell to hair bundle

deflection is sigmoidal (Figure 2D). The operating range of the hair cell corresponds to only about a 100 nm displacement of the hair bundle, meaning that larger deflections saturate the hair cell's response¹. But, within the operating range, the hair cell's response is graded: larger deflections produce larger receptor potentials.

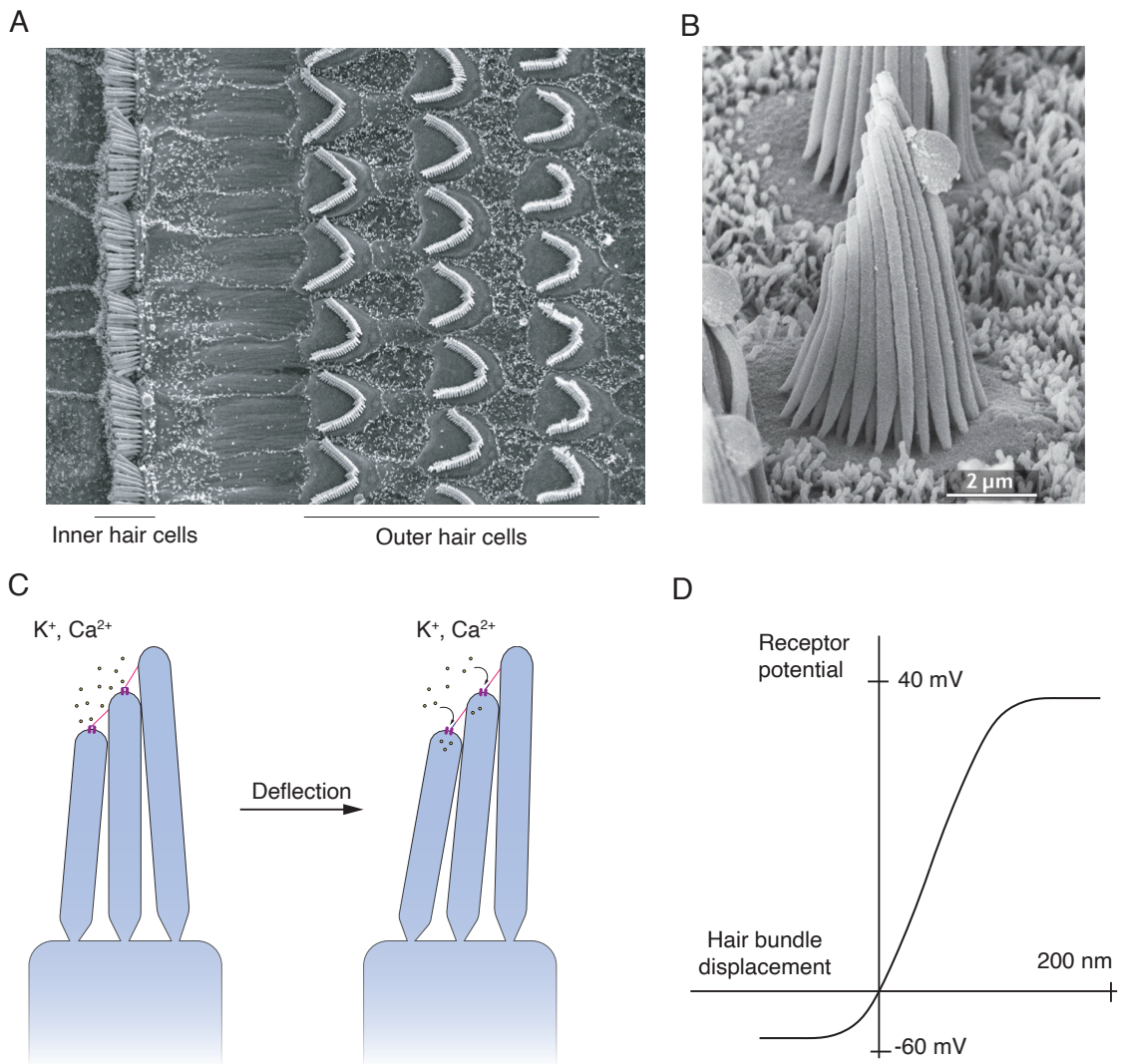


Figure 2. The structure of the hair bundles allows for mechanotransduction to occur when the bundle is deflected towards its tallest edge.

(A) The cochlea harbors one row of inner hair cells, each with a hair bundle arranged linearly, and three rows of outer hair cells, their hair bundles arranged in a V-shape. (B) Greater magnification of a hair bundle atop a bullfrog's hair cell

portrays its staircase-like structure: the shortest stereocilia occur at one edge of the hair bundle, and the stereocilia increase monotonically in height until the other edge of the hair bundle. In the bullfrog, and in immature mammalian hair bundles, the kinocilium stands at the tallest edge of the hair bundle. (C) When a hair bundle is deflected towards its tallest edge by a cochlear traveling wave, the mechanotransductive ion channels atop each stereocilium open, allowing ions to flow through the channels and depolarize the hair cell. (D) The relationship between hair bundle deflection and receptor potential is sigmoidal, and the operating range of the hair cell lies within its steep region. *Portions of this figure have been adapted from Principles of Neural Science.*

1.3 Fast and slow adaptation

If the hair bundle remains deflected for an extended period of time, such as in the presence of a constant stimulus, the channels begin to re-close. This process of adaptation maintains the responsiveness of hair cells on both fast (a millisecond or less) and slow (tens of milliseconds) timescales^{1,2}. Fast adaptation is thought to be mediated by the influx of Ca^{2+} ions through the MET channel, which results in stabilization of its closed conformation by Ca^{2+} binding^{1,2}. Slow adaptation is instead accomplished by relaxing the tension within the filamentous tip links connecting adjacent stereocilia³. This process is mediated by the proteins myosin 1c and myosin 7a, which connect the upper portion of the tip link to the actin core of the stereocilium^{1,4,5}. In response to a sustained stimulus, these motor molecules mediate the downward creep of the upper tip link density, which reduces the tension in the tip link and closes the MET channels.

1.4 The mechanotransduction channel complex

Experiments investigating the relationship between the transduction current and number of stereocilia per hair bundle suggest that there are two active MET

channels atop each stereocilium¹. The MET channel complex comprises several proteins (Figure 3). Transmembrane channel-like protein (TMC) is thought to be the primary pore-forming subunit of the MET complex⁶⁻⁸. TMC is localized to the tips of stereocilia, though it is absent in the tallest stereocilium, where transduction does not occur^{6,7}. Furthermore, mutations in its pore region residues decrease the channel's conductance, implicating it as the primary carrier of current through the MET complex^{7,9}. Both TMC1 and its paralog TMC2 are present in developing hair bundles, but only TMC1 is present in mature hair cells of the cochlea^{1,6,10}. Contacting TMC are the transmembrane inner ear-expressed gene (TMIE) and lipoma HMGIC fusion partner-like 5 (LHFPL5) proteins^{1,11}. It is not completely established what each component of the MET complex does, but several relations have been discovered. In the absence of TMIE, conductance through the channel is abolished, but in the absence of LHFPL5, conductance is not significantly affected^{9,12}. TMIE is essential to mechanotransduction, but not for MET complex assembly or development: in mice lacking TMIE, transduction is abolished even though all other components of the MET complex are present¹³. LHFPL5 interacts with the lower end of the tip link and TMC1, suggesting that transmission of force from the tip link to the MET complex occurs through LHFPL5^{11,14}. It also seems to have a yet-undefined role in tip link and channel assembly: in the absence of LHFPL5, PCDH15 does not efficiently localize to the stereociliary tips^{12,15}.

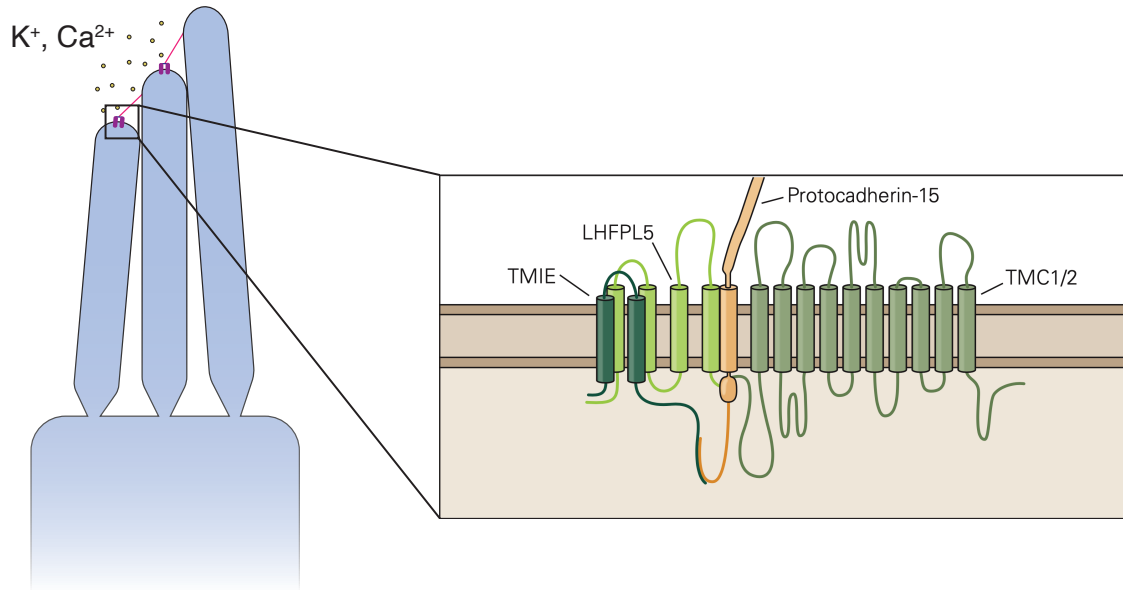


Figure 3. The mechanotransduction complex comprises several proteins. There are thought to be two active mechanotransduction channels per stereocilium. The inset shows the known components of the complex, which is thought to exist in two-fold symmetry. The lower end of the tip link intercalates with LHFPL5 and TMC1/2, suggesting a mechanism by which force can be transduced from deflection of the hair bundle to the ion channel. *Inset from Principles of Neural Science.*

1.5 The gating spring

The mechanotransduction of sound happens very rapidly, on the order of microseconds, much faster than the timescale for second messengers¹⁶. Unlike sensory cells that respond to membrane potential changes, hair cells respond directly to mechanical force. There are elastic elements called gating springs that are able to store mechanical energy to control the opening and closing of the MET channels¹⁷: when a stimulus begins to displace a hair bundle towards its tall edge, tension begins to build within the gating springs that are connected to the channels. When sufficient tension is stored within the gating springs, the channels open, resulting in a softening of the gating springs (Figure 4). Hair bundles are stiffest

along their axis of mechanosensitivity, which suggests that work must be done to an element along this axis in order to open the channels¹. Furthermore, when the MET channels open, their stiffness decreases, supporting the existence of a mechanical element associated with channel opening¹⁷. By means of variations in the physical properties of the gating spring, MET channels can have different opening probabilities and thus tune the sensitivity of the system to different stimuli.

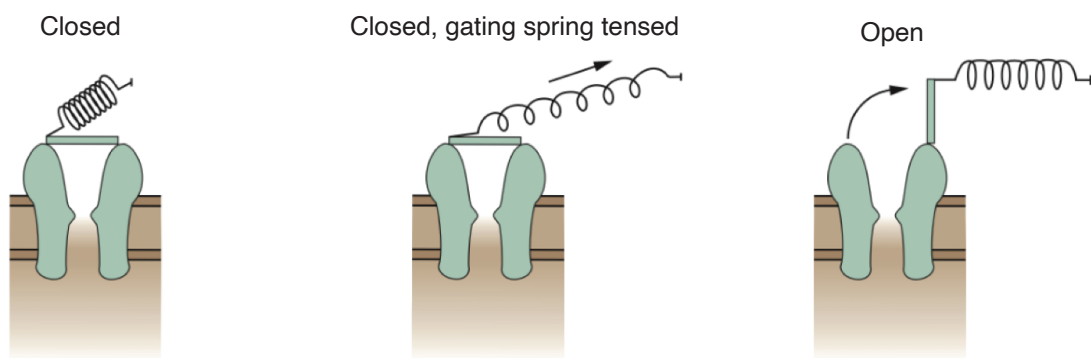


Figure 4. An elastic gating spring controls the opening of the mechanotransductive ion channels atop each stereocilium.

When the hair bundle is at rest, its ion channels are closed and the gating spring is relaxed. When the hair bundle begins to be deflected, its gating springs begin to tense. When sufficient tension is stored within the gating spring, the mechanotransduction channel opens. Owing to variations in the mechanical properties of the gating spring, the ion channels can have different opening probabilities. *Figure adapted from Principles of Neural Science.*

The filamentous tip link linking adjacent stereocilia is a leading candidate to be the gating spring. The tip link is a complex of proteins¹⁸ that links the MET complex of one stereocilium to the side of its tallest neighboring stereocilium. When the tip links are broken after addition of a Ca^{2+} chelator, mechanotransduction disappears¹⁹, and after they are allowed to regenerate on the timescale of hours,

mechanotransduction returns²⁰. When the tip links are disrupted, the hair bundle's stiffness also decreases²¹, which implies that the tip links can store mechanical energy, as the gating spring should. Additionally, because hair bundles are most sensitive to sound along their axis of mechanical sensitivity¹, tip links are a prime candidate for the gating spring due to their location linking adjacent stereocilia at the site of the MET complex. The stiffness of the gating spring has been measured to be on the order of 0.5-4 mN·m⁻¹ in a rat's cochlea²², a value that varies depending on whether the stiffness was measured in outer hair cells or inner hair cells and upon the location within the cochlea. Further underscoring the role of the tip link in hearing, there are hundreds of mutations within the tip link that result in human deafness²³⁻²⁶.

1.6 The tip link

The tip link complex spans approximately 150 nm and comprises a dimer of protocadherin 15 (PCDH15) at its lower end and a dimer of cadherin 23 (CDH23) at its upper end¹⁸ (Figure 5A). Both PCDH15 and CDH23 are part of the cadherin family of proteins, which includes diverse Ca²⁺-dependent cell adhesion proteins that transmit mechanical force^{27,28}. The two proteins interact with one another in a handshake, in which their two most N-terminal domains overlap in a Ca²⁺-dependent manner²⁹. Steered molecular dynamics simulations predict the handshake interaction will resist forces within the physiological range (up to 100 pN)²⁹, but recent single-molecule experiments have predicted the handshake to persist for only 8 s under physiological forces³⁰.

Both tip link proteins are constituted of extracellular cadherin (EC) domain repeats: PCDH15 comprises 11 EC domains and a membrane-proximal PCDH15-interacting channel-associated (PICA) domain, whereas CDH23 comprises 27 EC domains and one non-canonical 28th domain³¹. The EC domains of both proteins are sensitive to Ca²⁺ binding at their inter-domain linker regions³², which stabilizes both proteins to force. PCDH15 connects to the MET complex at its C-terminal end^{11,33} by interacting with both LHFPL5 and TMC 1 and TMC 2, directly implicating it in channel gating. CDH23 connects to the tallest neighboring stereocilium at its upper end, where it interacts with myosin 7a, myosin 1c, harmonin, and sans to interface with the actin skeleton of the stereocilium^{31,34,35}. At rest, the tension exerted on the tip link ranges from 2 pN to 20 pN, depending on the location within the cochlea²².

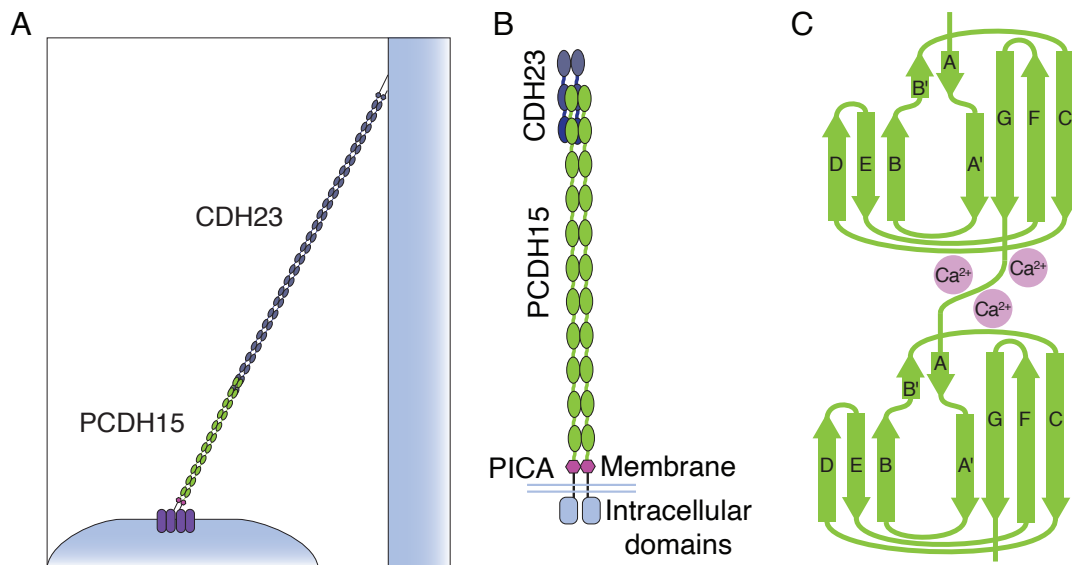


Figure 5. The tip link comprises protocadherin 15 and cadherin 23, two Ca²⁺-binding cadherin family proteins.

(A) A dimer of protocadherin 15 and a dimer of cadherin 23 interact in a 'handshake' interaction stabilized by Ca²⁺ binding to form the tip link connecting

adjacent stereocilia. (B) Protocadherin 15 comprises 11 EC domains as well as a membrane-proximal PICA domain, transmembrane domain, and cytoplasmic domain. Short inter-domain linker regions separate the individual domains. (C) Each EC domain is composed of seven β -sheet strands. Between domains, mediated by the linker region, up to three Ca^{2+} ions can bind to stabilize the structure of protocadherin 15.

1.6.1 Protocadherin 15

The rest of the text will focus on PCDH15, so I will now further describe its key physical properties. The *PCDH15* gene is located at 10q21 and there are three main splice isoforms of PCDH15 (CD1, CD2, and CD3) that differ only in their cytoplasmic domains^{36,37}. PCDH15 comprises 11 EC domains, a membrane-proximal PICA domain, a transmembrane domain, and a cytoplasmic domain (Figure 5B). PCDH15 dimerizes at EC 3 and the PICA domain³⁸.

Each of the 11 EC domains of PCDH15 follows a Greek key motif comprising seven β -sheets (Figure 5C) and, when folded, is approximately 4.5 nm in length²⁸. There are short inter-domain linker regions, which range from 1 nm to 3 nm in length³⁹, and, like most in the cadherin family, facilitate the binding of Ca^{2+} ions between domains⁴⁰. The linkers typically contain a conserved DXNDN motif, whereas the preceding EC domain contains DXE and XEX motifs and the succeeding EC domain contains DXD and XDX motifs⁴⁰. This means that Ca^{2+} not only binds to the linker regions, but also to the edges of the neighboring EC domains. As a result, Ca^{2+} stabilizes the structure of PCDH15 against unfolding. The Ca^{2+} -binding behavior varies with the linker region—some linkers bind no Ca^{2+} , whereas others bind one, two, or three Ca^{2+} ions⁴¹. The variability in Ca^{2+}

binding among the linker regions suggests that some regions are more prone to unfolding than others: if fewer than three Ca^{2+} ions are bound, the linker region and neighboring EC domains might unfold sooner than others at the same Ca^{2+} concentration when exposed to force.

PCDH15 also has numerous glycosylation sites along its length, and glycosylation residues have been observed in crystal structures of PCDH15⁴¹. Glycosylated residues may confer an additional degree of association between the two strands of the PCDH15 dimer, which could then affect the dynamics of PCDH15 in ways not predicted by the protein structure alone.

At the C-terminal end of PCDH15, adjacent to the plasma membrane, is the PICA domain. Its structure is distinct from that of the EC domains: it has a ferredoxin-like fold, comprising both α -helices and β -sheets⁴². Steered molecular dynamics simulations have predicted the PICA domain to unfold more easily than the EC domains⁴².

Following the PICA domain are the transmembrane and cytoplasmic domains of PCDH15. The cytoplasmic domain of PCDH15 binds to LHFPL5 and TMC1/2, suggesting a mechanism by which force can be transduced from the tip link to the MET complex^{11,33}. The three isoforms of PCDH15, which differ only in their cytoplasmic domains, have unclear functions. Mice without CD1 and CD3 form normal hair bundles, whereas those lacking CD2 are deaf⁴³. The cytoplasmic and transmembrane domains seem to be essential for mechanotransduction: in zebrafish lacking either the cytoplasmic or the transmembrane domain of PCDH15,

the tip links localize correctly to the stereociliary tips, but mechanotransduction does not occur⁴⁴.

1.7 Deafness mutations in PCDH15

There are hundreds of deafness-causing mutations within the tip link proteins, and many of them within PCDH15. These mutations can cause either non-syndromic deafness, which is deafness alone, or syndromic deafness, which is deafness accompanied by other deficits as a result of the same mutation.

1.7.1 Usher syndrome

Usher syndrome has a prevalence of between one in 16,000 and one in 50,000 and is characterized by varying degrees of deafness, blindness, and vestibular dysfunction that have different ages of onset^{23,45}. Usher syndrome is caused by mutations in various gene loci, such as those encoding the myosin 7a, harmonin, CDH23, and clarin-1 proteins in hair cells⁴⁵. Usher syndrome type 1F (USH1F) is caused by mutations in PCDH15 and results in deafness, retinitis pigmentosa, and vestibular dysfunction within the first ten years of life⁴⁵. Mutations in PCDH15 resulting in USH1F are predominantly nonsense mutations that result in a truncated version of PCDH15²³. In addition to being in the cochlea, PCDH15 also occurs in the tip links of the hair cells of the vestibular system. In the retina, PCDH15 forms links with CDH23, and together they link the outer segment to calyceal processes or interlink the calyceal processes⁴⁶. When PCDH15 is mutated in USH1F, the links in the vestibular system and the retina are disrupted enough to result in vestibular dysfunction and retinitis pigmentosa. The genetic

cause of USH1F makes it particularly amenable to gene therapy approaches with adeno-associated virus vectors (AAVs). Recently, there has been success in the use of shortened PCDH15 constructs in AAVs to rescue hearing in a mouse model of USH1F⁴⁷.

1.7.2 Non-syndromic deafness

There are numerous mutations in PCDH15 that do not result in USH1F, but rather in non-syndromic autosomal recessive deafness type 23 (DFNB23). These mutations have been of particular interest to me, for although PCDH15 is present in the vestibular system and the retina in addition to the ear, only hearing is affected in individuals with these mutations. This pattern suggests that something about the mutation precludes its normal function within the cochlea while allowing it to function normally within the vestibular system and the retina. These mutations tend to be missense mutations throughout the protein rather than nonsense or deletion mutations as in USH1F²³. I chose to study one of these mutations in my thesis work and will discuss it in a later chapter.

1.8 Optical tweezers

An optical tweezers is an apparatus used to manipulate particles using the beam of a highly focused laser. Forces on the order of piconewtons can be exerted on nanometer- or micrometer-sized particles to study fundamental processes of biology. Optical tweezers rely on the principles of optical trapping, which Arthur Ashkin discovered in the 1970s when he found that the radiation pressure of a laser could trap micron-sized latex spheres⁴⁸. Optical tweezers allow for the control

and measurement of both the force on and the displacement of a particle. Other single-molecule techniques, such as atomic force microscopy and magnetic tweezers, can perform similar tasks. However, magnetic tweezers are limited by their lack of sample manipulation⁴⁹, because the force field is homogenous and the particle cannot be as easily manipulated in three dimensions compared to other methods. Atomic force microscopy is limited by a lower force bound higher than the minimal forces involved in hearing. Therefore, optical tweezers are ideal for studying proteins involved in hearing within a physiological force range.

The mechanism of particle trapping depends on the size of a particle. If the particle is much smaller than the wavelength of the trapping laser, then the particle gets trapped because of the balance between the scattering force and the gradient force of the laser (Figure 6A). In the case of a non-uniform laser field, such as in a Gaussian laser beam, the particle becomes polarized and is attracted to the region of highest laser intensity, which is the center of the laser beam⁵⁰. This is called the gradient force acting on the particle. In contrast, the scattering force is a result of the photons of the laser beam pushing the particle along the direction of propagation⁵¹. For a particle to be stably trapped, the gradient force must exceed the scattering force. This condition is achieved by using a high-numerical-aperture objective lens to tightly focus the laser light. If the particle is much larger than the wavelength of light, ray optics can be used to describe the mechanism of trapping⁵⁰ (Figure 6B). When a particle is in a laser beam, the photons of the beam interact with the particle, resulting in force generation. By Newton's second law of motion,

$\vec{F} = \frac{d\vec{p}}{dt}$, where \vec{p} is the momentum of the particle or photon, the momentum of the photon causes an equal and opposite change in momentum of the trapped particle. The photons are either refracted by the particle, resulting in a force pulling the particle to the laser's focus, or reflected by the particle, resulting in a force pushing the particle along the path of the laser beam⁵⁰. For the particle to be stably trapped, these two forces must be in equilibrium with each other.

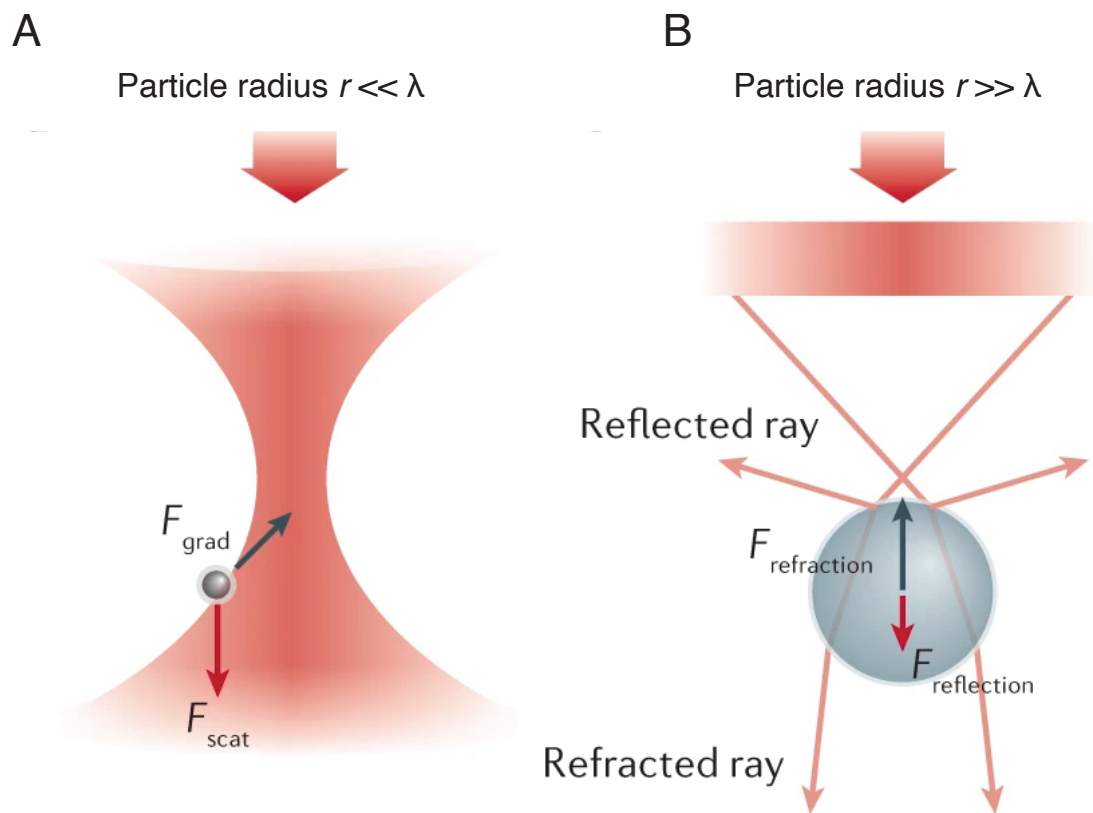


Figure 6. The mechanism of optical trapping depends on the particle size. (A) Particles much smaller than the wavelength of the trapping laser act as Rayleigh scatterers in the laser beam's field. In this regime, a particle is trapped in the laser by gradient force (F_{grad}) attracting the particle to the region of the highest intensity of the laser beam. The scattering force (F_{scat}) of the laser is a result of the laser beam's photons pushing the particle along the path of the beam. As long as $F_{grad} > F_{scat}$, the particle is trapped. (B) Particles much larger than the wavelength of the trapping laser are trapped as a result of the balance of the refractive force

($F_{refraction}$) and the reflective force ($F_{reflection}$) acting on the particle, following the conservation of momentum. *Figure adapted from Bustamante et al. (2021).*

The biomolecules of interest, such as protein or DNA, are often too small to be stably trapped in the beam of an optical trap. Therefore, they are attached to micrometer-sized beads, which can be easily manipulated within an optical trap. There are several common optical trapping geometries, each with its own benefits and limitations, and these geometries can be divided into single- and dual-trap set-ups. In single-trap set-ups, one end of the molecule of interest is tethered to a bead in the single optical trap while the other end is tethered either to a functionalized surface or to a second bead held stationary by some other method, such as in the suction of a pipette^{50,52}. In dual-trap set-ups, the molecule is strung between two beads, each held within an optical trap. The linkage of the biomolecule to the bead or surface on either end is usually accomplished by unique tethers on the two ends. Streptavidin-biotin and antibody-antigen linkages are often used due to the ease with which they can be incorporated into the system of interest and the affinity of their interactions⁵⁰.

Single-molecule techniques are powerful tools to understand how individual molecules function in biological contexts. Understanding how molecules work on a single-molecule level rather than in ensemble allows us to dissect the mechanisms of biological processes, detect sparsely-populated states, and observe intermediate states. Optical tweezers, in turn, is a single-molecule technique that allows for the direct measurement of the forces and extensions

involved in biological processes. This makes optical tweezers an insightful tool to probe the mechanics of PCDH15, a protein essential to human hearing.

CHAPTER 2. The photonic force microscope

Before proceeding to experimentation, we first had to validate the optical trapping system that I planned to use in future experiments. The photonic force microscope (PFM) used in this work was custom-built in the laboratory and modified as needed for the experiments described here. Because our PFM has microsecond temporal resolution and sub-nanometer spatial resolution, it is an appropriate system with which to study the proteins involved in mammalian hearing, which have lengths on the order of nanometers and can undergo rapid conformational changes.

2.1 Experimental apparatus

In a typical experiment, PCDH15 is tethered between two beads: at its C-terminus it is attached by a SpyTag-SpyCatcher bond to a pedestal bead covalently attached to a glass coverslip, and at its N-terminus it is linked through a biotin-streptavidin interaction to a probe bead in solution (Figure 7A). The molecular anchors that attached PCDH15 to the beads on either end are separated from the protein by short, unstructured peptides. Two lasers act upon the probe bead: a highly stable 1064 nm position-sensing laser, which detects the three-dimensional position of the probe bead and thus the extension of the construct, and an 852 nm force-producing laser, which exerts force on the probe bead and therefore also on the protein.

To explore the range of physiological forces that PCDH15 experiences in the ear⁵³, I conducted force-ramp experiments in which force was increased at a constant rate and then decreased back to a resting level of 1 pN, where it was held

for 2 s before the next cycle (Figure 8A). In these extension-relaxation cycles, the protein sometimes underwent conformational changes, such as unfolding events, which could be seen as steps in the end-to-end distance (Figures 7B and 8B). After a force-ramp cycle had been repeated up to hundreds of times on a single protein molecule, all the cycles could be displayed as a heatmap in which the lighter colors corresponded to highly occupied states and the darker colors represented trajectories that occurred only once or a handful of times (Figure 7C).

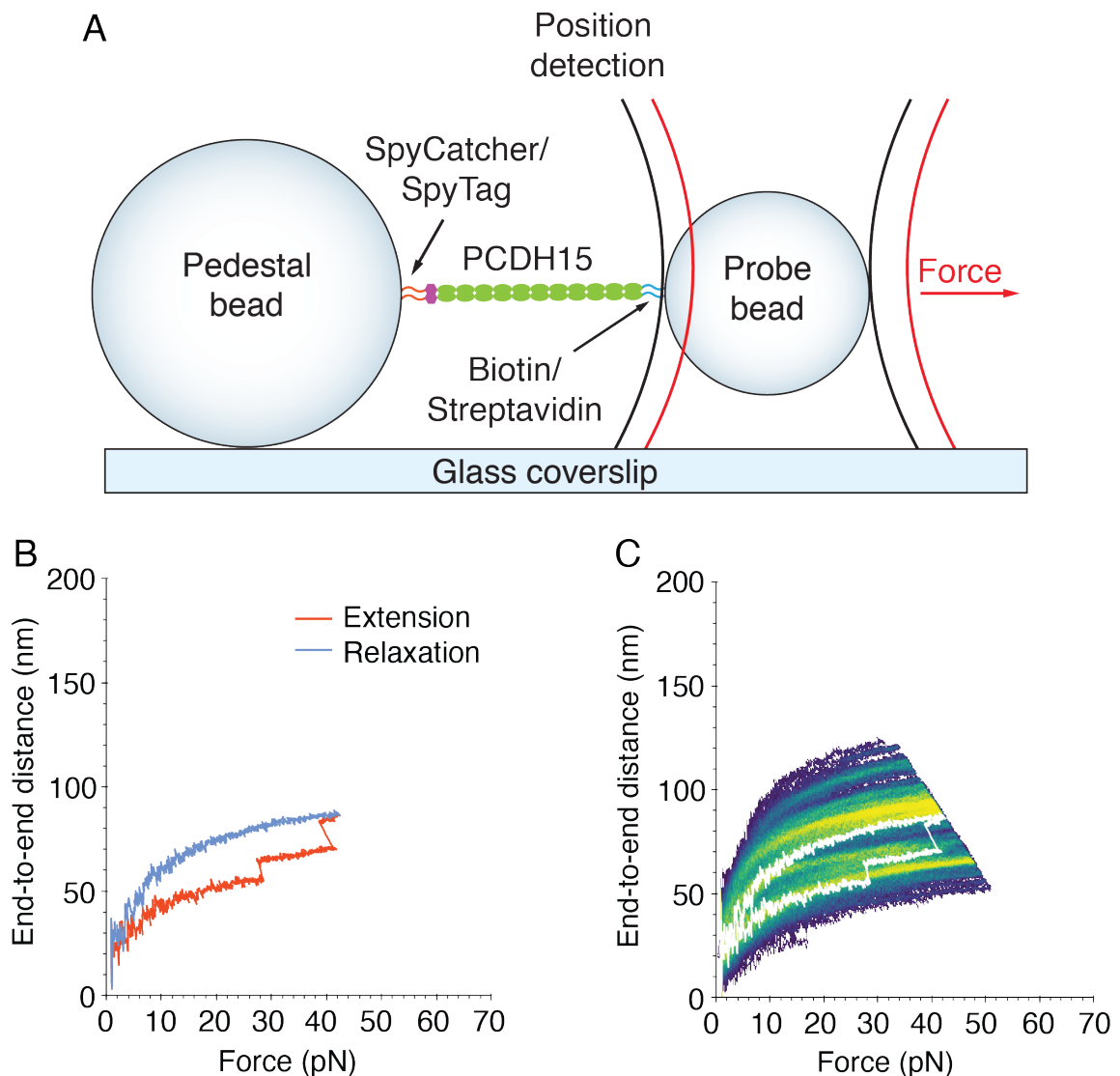


Figure 7. Optical trap and illustrative results.

(A) In our optical trap, the protein is tethered between two beads, and two lasers act upon the probe bead to measure the position of and exert force on the probe bead. Not drawn to scale. (B) A force-ramp experiment comprises the extension phase of the cycle, during which force is increased at a constant rate, and the relaxation phase of the cycle, in which force is decreased back to a given minimum. In these experiments, the minimum force is 1 pN and there are 2 s between successive force ramp cycles. Unfolding changes can be seen as sudden steps in an individual trajectory, such as the two observed in the extension phase of this force ramp cycle. (C) Repetition of the force ramp cycle hundreds of times on the same protein molecule yields a heatmap in which the brighter colors represent more highly occupied states. The heatmap overlays both extension and relaxation phases of every cycle. The exemplary cycle from Fig. 7B is shown overlaid in white.

The data shown here were taken in the absence of Ca^{2+} (with 1 mM EDTA). *Figure and caption adapted from Villasante et al. (2023)⁵⁴.*

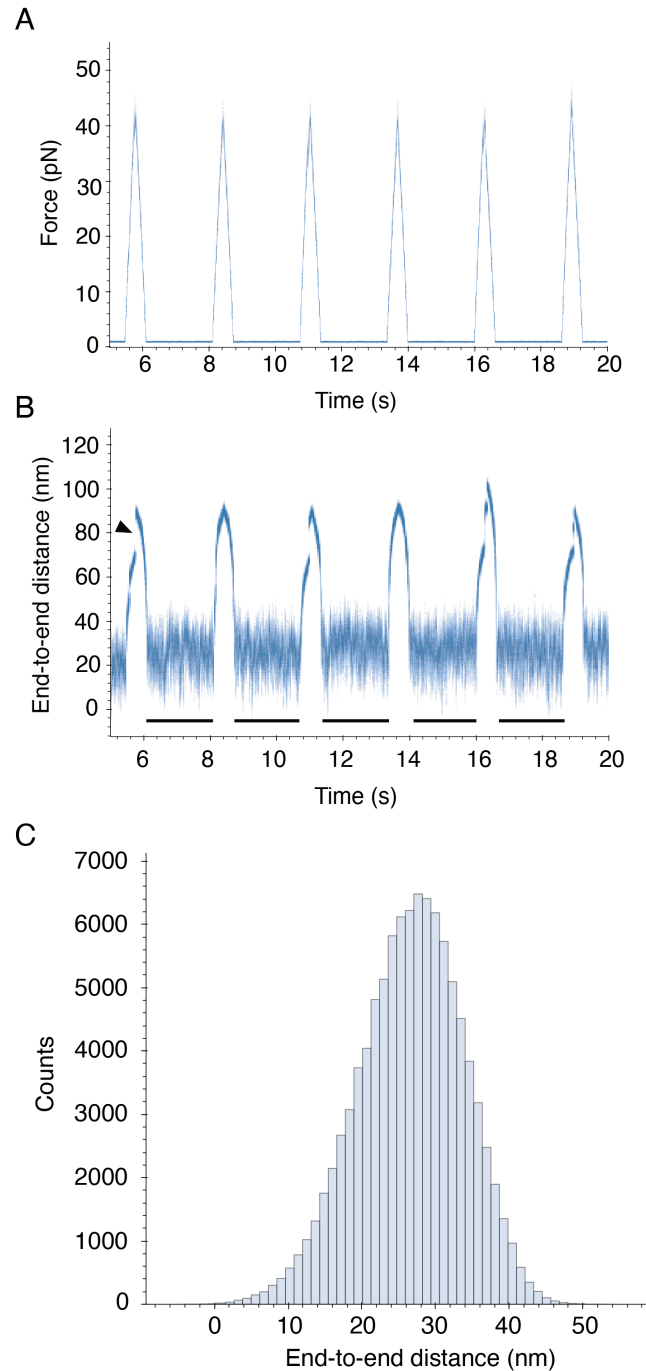


Figure 8. Illustrative force stimulus and position traces.

(A) During a force-ramp cycle, force is first applied at a constantly increasing level up to a given maximum by increasing the spring constant of the force-producing laser. Force is then decreased at the same rate until a minimum force of 1 pN is reached. There is a 2 s inter-ramp resting period during which the system is held at 1 pN. (B) The corresponding position traces show the end-to-end distance of the protein in response to the force stimulus. Occasional unfolding events during the force application portions of the cycle are seen as sudden changes in the end-

to-end distance. Black arrowhead indicates one such unfolding event. (C) The regions from *B* underlined in black correspond to the low-force inter-ramp regions. The end-to-end distance of PCDH15 at low force is approximately Gaussian-distributed. In this case, the average end-to-end distance during those five force-free regions is 26.6 ± 0.01 nm (mean \pm SEM; $n=999901$ data points). The data shown here were taken in the absence of Ca^{2+} (with 1 mM EDTA).

2.2 Position detection

The position of a bead within a laser's trap can be read out from a quadrant photodiode (QPD) positioned in the back focal plane of the condenser lens. When the bead lies in the beam of the laser, it scatters light from the laser beam. The interference patterns resulting from the interaction of the bead with the beam of the laser are transmitted onto the QPD (Figure 9). Movement of the bead in the *x*- and *y*-directions is reflected on the four quadrants of a QPD and can be calculated by measuring the voltage changes across them. The bead's axial position is a function of total signal intensity⁵⁵. The position signals S_x , S_y , and S_z can be found by relating the voltage signals Q_1 , Q_2 , Q_3 , and Q_4 from the four quadrants of the photodiode:

$$\begin{aligned}
 S_x &= (Q_1 + Q_3) - (Q_2 + Q_4) \\
 S_y &= (Q_1 + Q_2) - (Q_3 + Q_4) \\
 S_z &= Q_1 + Q_2 + Q_3 + Q_4
 \end{aligned}
 \tag{2.1}$$

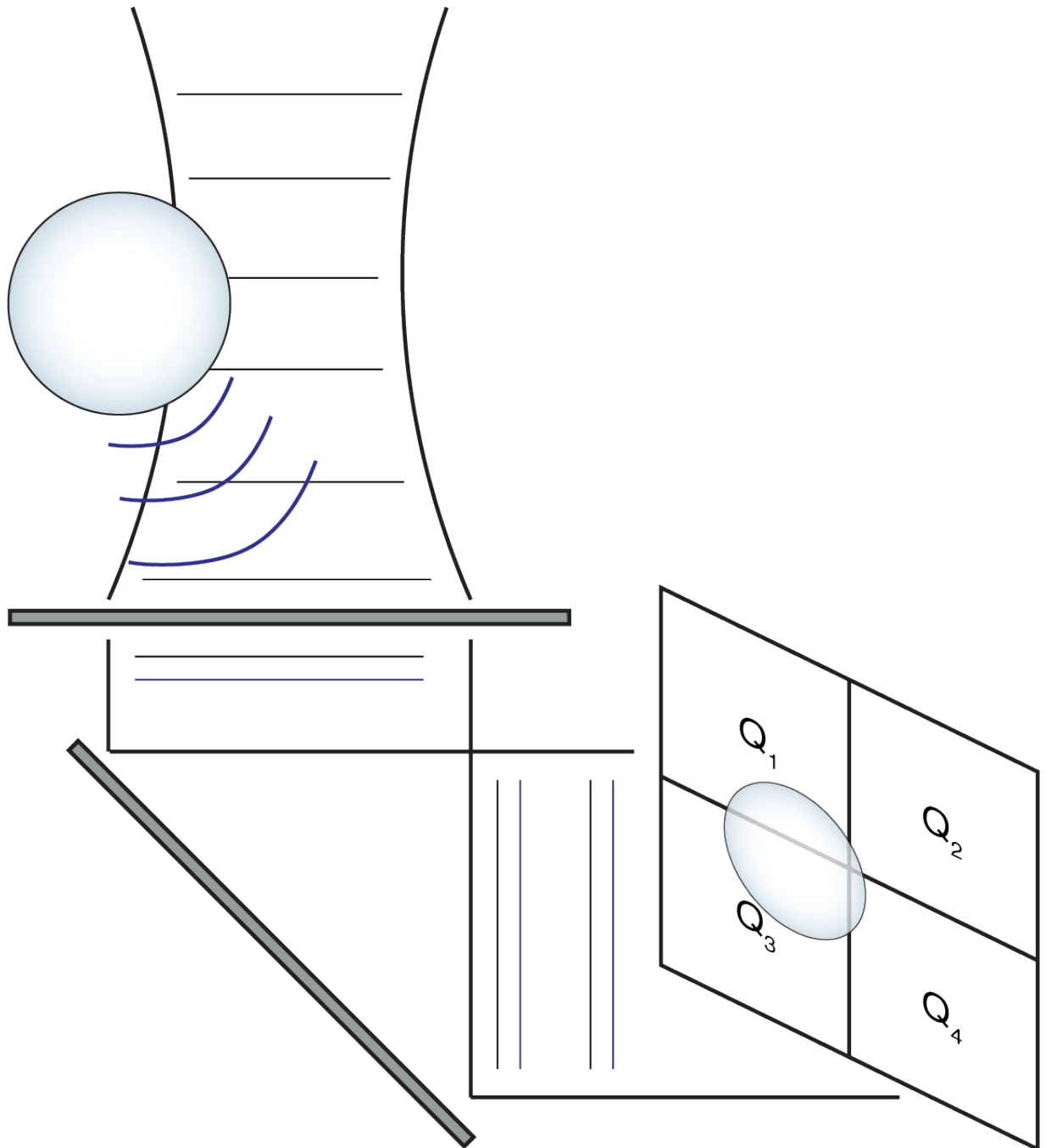


Figure 9. Position detection by a quadrant photodiode.

When a bead interferes with the beam of the position-sensing laser, it creates interference patterns that are captured by a quadrant photodiode placed in the back focal plane of the condenser lens. The x-, y-, and z-position of the bead can be calculated from the resulting voltage differences across the quadrants of the photodiode.

2.3 A freely diffusing particle

The diffusion of a probe bead can be described by the Langevin equation⁵⁶:

$$m\ddot{x} = -\gamma\dot{x} + \eta \quad (2.2)$$

in which m is the particle's mass, \ddot{x} is its acceleration, γ is its drag, \dot{x} is its velocity, and η is the stochastic force acting on the particle. The inertial term of the bead can be set to zero because the friction of the system is much larger than the inertia of the bead⁵⁷. This yields

$$0 = -\gamma\dot{x} + \eta, \quad (2.3)$$

from which we can then compute several useful quantities describing the motion of the bead in an optical trap, which will be described in the following sections.

The mean squared displacement (MSD) can be derived from the Langevin equation⁵⁸, resulting in the theoretical MSD of the particle in one dimension

$$MSD = 2Dt, \quad (2.4)$$

in which D is the local diffusion constant and t is the time interval. The diffusion constant D is given by the Stokes-Einstein relation⁵⁹

$$D = \frac{k_B T}{6\pi\mu R}, \quad (2.5)$$

In which k_B is the Boltzmann constant, T is the temperature, μ is the viscosity of the fluid, and R is the radius of the particle.

2.4 Motion of a particle in an optical trap

When the probe bead is in an optical trap, its motion is confined, and the particle is drawn towards the trap's center. The Langevin equation for its motion gains an additional term to describe the confining potential of the optical trap, becoming

$$m\ddot{x} = -\gamma\dot{x} - kx + \eta. \quad (2.6)$$

Here k is the spring constant of the optical trap confining the bead. The other variables are as in Equation 2.2. The expected relationship between MSD and time is linear in the case of Brownian motion, but when the bead is confined within an optical trap this relationship becomes nonlinear due to the trapping potential's influence on the position of the bead over time. If the timescale t is sufficiently short, less than the autocorrelation time $\tau = \gamma/2k$, then the bead's diffusion approximates free diffusion^{55,60}. If t exceeds the autocorrelation time, then the bead's diffusion is more circumscribed. In our system, t is shorter than the autocorrelation time, so these effects are unimportant.

2.5 Calibration of the position detector

We can next determine the sensitivity of the position detector. The relationship between the bead's position and the signal $S_{x,y,z}$ measured from the QPD is linear near the focus, and the sensitivity of the detector in each direction is given by the slope of the linear region of the signal in that direction (Figure 10A-C). This quantity can be measured by scanning over a bead immobilized on a glass coverslip in the PFM.

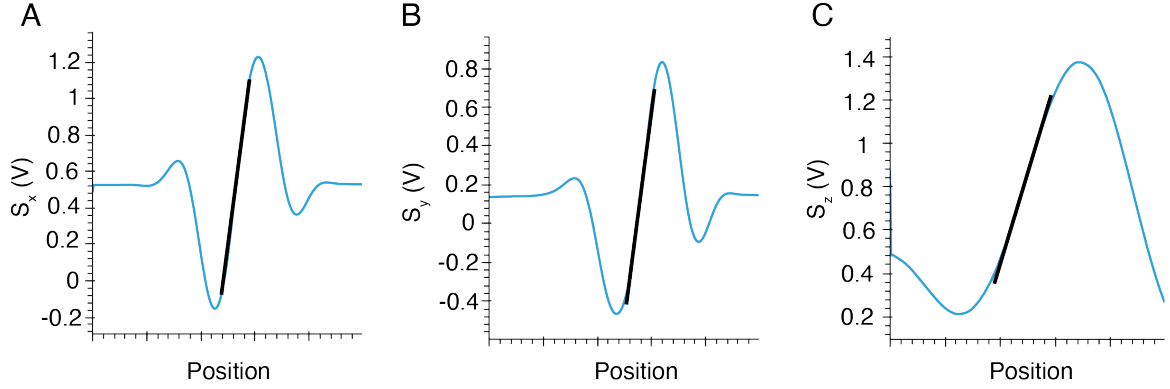


Figure 10. Position detector sensitivities.

An immobilized 1 μm probe bead was scanned through the focus of the position-sensing laser. The signals in the x-, y-, and z-directions are shown in A, B, and C respectively. The detector's sensitivity can be calculated from the linear regions of each response curve, indicated by the black line in each plot.

However, at a distance from the focus, away from the linear region of the detector response, it is necessary to correct for the nonlinear relationship between bead position and position-detector signal⁵⁵. In addition, for the determination of the detector sensitivities as in Figure 10, the bead has to be immobilized on a surface. In my experiments, the bead is trapped while in solution, so the determination of detector sensitivities must be done in an alternative way.

While the bead is in the optical trap, its local MSD is a function of the signal S

$$MSD_L(SX_0, t) = \frac{1}{N} \sum_{SX_0 - \delta SX < SX(t) < SX_0 + \delta SX} (SX(t' + t) - SX(t'))^2. \quad (2.7)$$

Here SX_0 is the signal in the x-direction corresponding to position x_0 , N is the number of position measurements, and t is the time lag⁵⁵. The relationship is identical in the y- and z-directions. We can then measure the sensitivity of the detector:

$$\partial_x SX|_{SX_0} = \sqrt{\frac{MSD_L(SX_0, t)}{2Dt}}. \quad (2.8)$$

The sensitivity of the detector is linear close to the center of the optical trap, but becomes nonlinear at its boundaries⁵⁵. By integrating the sensitivity of the detector in each dimension, we can extract the corrected position signals⁵⁵:

$$SX(t)_{corr} = \int \frac{1}{\partial_x SX|_{SX'}} dSX' + const. \quad (2.9)$$

The relationship is similar for the y - and z -directions.

2.6 Force production and calibration of the force-producing laser

The 852 nm force-producing laser exerts force on the probe bead and therefore on the attached protein molecule. Force is exerted on the probe bead by displacing the trap of the force-producing laser from that of the position-sensing laser (Figure 11). This results in the probe bead being pulled away from the center of the position-sensing laser's optical trap and instead towards the center of the force-producing laser's optical trap. This relationship is given by

$$F = k_{852}(\Delta L - x), \quad (2.10)$$

in which F is the force produced by the laser, k_{852} is the spring constant of the force-producing laser, ΔL is the displacement between the centers of the two traps, which is 200 nm, and x is the displacement of the bead towards the center of the force-producing optical trap. By changing the intensity of the laser beam, a Pockels cell in series with the laser's beam can modulate the spring constant k . In the course of a force ramp experiment on PCDH15, immediately following an unfolding event there is a transient decrease in force (Figure 7B). This transient results from the relation given in the above equation. When the displacement x increases due

to an unfolding event, the force F decreases until the spring constant k increases sufficiently to generate the same amount of force as before the unfolding event.

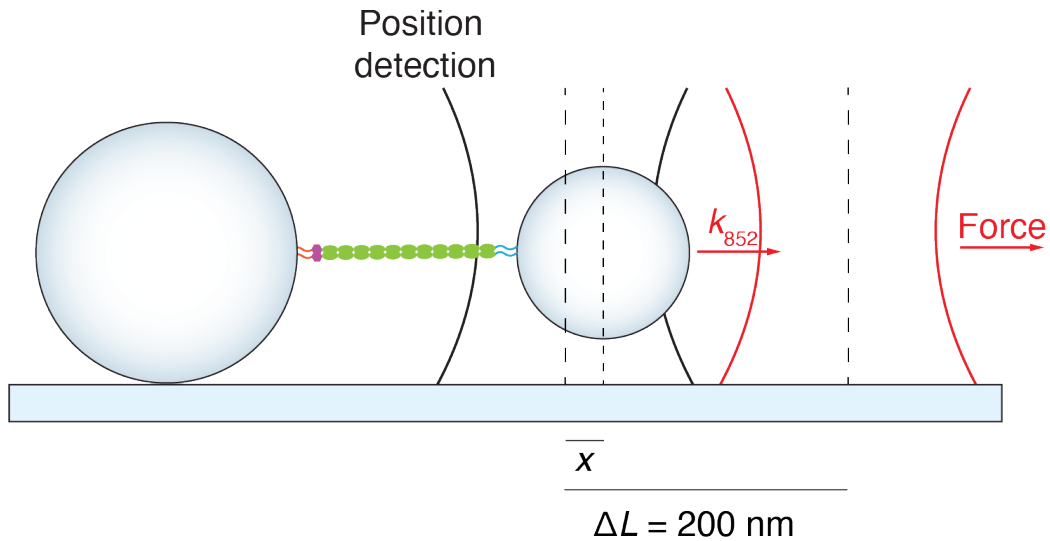


Figure 11. Force is produced by displacing the force-producing optical trap and modulating its spring constant.

When the center of the force-producing laser is displaced by 200 nm from the center of the position-detecting laser, force is exerted on the probe bead held within the position-detecting trap. The center of the probe bead is then pulled towards the force-producing trap (x). The force depends on the spring constant k_{852} of the force-producing laser.

The force produced by this laser depends on its spring constant, which depends on the intensity of the laser. A Pockels cell in the beam path of the laser modulates the intensity of the laser. The electro-optic crystal within the Pockels cell changes its shape upon voltage application, changing the birefringence of the crystal and modulating the polarization of the transmitted light⁶¹.

At each laser intensity level, a corresponding power spectral density of the bead's position over time can be derived from the Langevin equation⁶², yielding

$$P_k = \frac{D/2\pi^2}{f_c^2 + f_k^2}. \quad (2.11)$$

Here D is the diffusion constant and f_c is the corner frequency given by $f_c = \frac{K}{2\pi\gamma}$, in which K is the stiffness of the trap and $\gamma = 6\pi\rho\nu R$ is the bead's drag given by Stokes' law⁶², f_k is given by $f_k = \frac{k}{T_{msr}}$, in which k is an integer and T_{msr} is the measured time. The power spectral density decomposes the signal into its power components by frequency. By calculating the corner frequency at each laser intensity level, we can calculate the stiffness of the laser at each intensity. This allows us to determine the force produced by the 852 nm laser at a given intensity level.

2.7 Considerations for the molecular anchors

Portions of this section have been excerpted or adapted from Bartsch, Villasante, Hengel *et al.* (2021), which I co-wrote in association with the listed authors⁶⁰.

Before beginning experiments with PCDH15, I first had to test the system in the absence of PCDH15, with only the molecular anchors. This step allowed me to delineate the contribution of PCDH15 and the anchors separately, as well as to confirm that all parts of the PFM were functioning appropriately.

In optical trap experiments, the biomolecule of interest is usually too small to be directly manipulated by the beam of the laser. Instead, the biomolecule is commonly attached to a micrometer-sized bead that can be easily manipulated in an optical trap. To prevent nonspecific interactions between the biomolecule and the bead, this attachment is often mediated by long tethers of dsDNA⁵⁰. However,

the use of long tethers can conceal information about the properties and behavior of the molecule being studied. When force is applied to the bead in the laser's trap, it is dissipated through the linkers, which are softer, making it difficult to isolate the stiffness of the protein alone. This problem is magnified at higher loading rates of force application, which are necessary to study proteins involved in mammalian hearing, which operate in the range of 20 Hz to 20 kHz. This means that the protein does not have time to adequately respond to the force applied at these high rates because it is filtered through the softer linkers. The position of the biomolecule as a result of the force is then filtered with a time constant of γ/κ , in which γ is the bead's drag coefficient and κ is the confining potential on the bead, which includes the stiffness of the optical trap and those of the molecular attachments on the bead⁶⁰. Therefore, with long linkers, it is not possible to know the immediate position of the biomolecule. Instead, the position measured is the time-averaged end-to-end distance of the protein, which hides the rich conformational changes that the protein undergoes as a result of force.

To study processes that occur on rapid timescales, such as those of mammalian hearing, we needed to maximize the spatial and temporal resolution of our system. Some approaches have been taken to develop short and stiff linkers to better couple the movement of the bead within the laser beam to the attached protein. This approach has been previously accomplished by using rigid DNA 'origami' molecules⁶³ or short chemical spacers⁶⁴ as tethers. In our apparatus, PCDH15 has to be tethered specifically to beads on both ends, so unique tags

were required for each end: SpyCatcher/SpyTag on its C-terminus and biotin/streptavidin on its N-terminus. To link the functional tags to the protein itself, we employed short GSGSGS links on either end. Together, these components had an expected total length⁶⁵ of 11.4 nm. This expected value fits very well with my experimentally determined value for the average position of the anchors alone at the 1 pN resting force between force ramps, which is 11.8 ± 2.0 nm (mean \pm SEM; $N = 3$ datasets).

An issue with using short linkers to couple the protein to the beads on either end is that the beads, as well as the trapping potential on the probe bead, can influence the protein and position signal read out by the position-sensing laser. In addition to characterizing the stiffness and behavior of the anchors in the absence of PCDH15, we also had to correct for these effects. We developed a method to correct for the influence of the pedestal bead on the position signal of the probe bead⁶⁰. The probe bead's position signal within the optical trap is read out by interference patterns on a quadrant photodiode (Figure 12A). When a bead is close to another object, such as a pedestal bead, the position signal read on the quadrant photodiode includes the effects of the pedestal bead (Figure 12B). The total position is then

$$S_{total}(b_{pedestal}, b_{probe}) = S_{pedestal}(b_{pedestal}) + S_{probe}(b_{probe}). \quad (2.12)$$

Here $b_{pedestal}$ and b_{probe} are the position vectors of the pedestal and probe beads, respectively, and $S_{pedestal}$ and S_{probe} are the signals of the pedestal bead in the absence of the probe bead and of the probe bead in the absence of the pedestal

bead, respectively. In a typical experiment, the pedestal is fixed at least $1.5 \mu\text{m}$ from the focal spot of the position-sensing beam, a distance determined by the radii of the pedestal and probe. The probe's diffusion is confined by the beam's trapping potential and is centered on the focal spot. The pedestal's signal thus constitutes a constant offset added to the probe's signal. If the magnitude of this offset is known, it can be subtracted from the total signal to yield the signal of the probe alone⁶⁰.

To visualize the contributions of the two independent signals, we independently recorded the signals for displacements of the probe and the pedestal, then displayed them offset by $1.5 \mu\text{m}$ relative to one another (Figure 12C). This procedure reflected the case in which the probe was at the center of the position-sensing optical trap, defined as $x = 0$, and just touched the pedestal. If the signal S_{probe} was held constant by fixing the probe's displacement b_{probe} from the focus of the position-sensing trap, then the offset could be determined by monitoring how the measured total signal S_{total} changed as the pedestal was brought progressively closer to the focal spot. Holding b_{probe} constant by means of a second optical trap that strongly confined the probe at a displacement of 100 nm with respect to the focus of the position-sensing beam, we then recorded the total detector signal while the pedestal was so distant that its signal was negligible ($S_{pedestal} \approx 0$). This signal served as a reference. As we moved the pedestal toward the focal spot of the position-sensing beam while keeping the

probe confined at a constant position with the second trap, the deviation in S_{total} represented the signal $S_{pedestal}$ owing to the pedestal (Figure 12D).

To demonstrate that we could successfully correct for the influence of the pedestal, we next used the stimulus trap to hold the probe at the center of the position-sensing trap ($x=0$). We recorded the photodiode's total signal and recovered the position of the probe by subtracting the offset caused by the pedestal. The position signal after compensation was nearly zero (Figure 12E). If the offset correction was not performed and the total signal on the detector was calibrated without subtraction of the pedestal's influence, a significant systematic position error arose that depended sensitively on the distance between the pedestal and the center of the position-sensing optical trap.

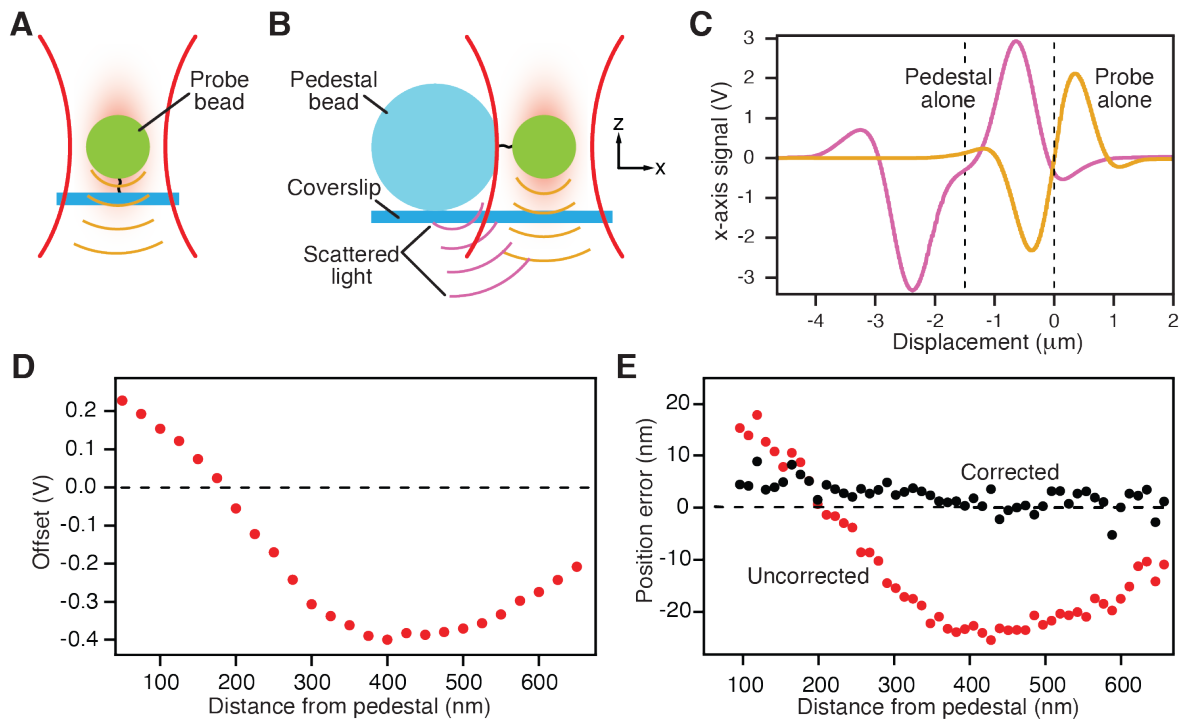


Figure 12. Apparatus and control experiments.

(A) When a probe bead is held in an optical trap (red), its position can be measured along three axes by capturing transmitted and forward-scattered light (orange) on

a quadrant photodiode. (B) A stationary pedestal, to which one end of a filamentous protein is attached, scatters a small fraction of the incident light (purple) and contaminates the desired signal for the probe. (C) Control measurements show the signals as a function of offset position due to the probe alone and to the pedestal alone. The two signals have been offset by $1.5\ \mu\text{m}$ (dashed lines) to simulate the configuration during an actual experiment. (D) With the probe fixed in place, moving the pedestal nearby produces a spurious offset signal. The dashed line shows the reference signal for the probe far from the pedestal. (E) The systematic error in position measurements owing to the pedestal is reduced by the compensation procedure to a few nanometers. *Caption and figure from Bartsch, Villasante, Hengel, et al. (2021).*

2.8 Thermal force probing

The probability density of the diffusion of the probe bead when weakly confined by the 1064 nm position-sensing laser follows a Boltzmann distribution. The movement of the bead in the trap is driven by thermal energy, and if we record the movement of the bead in the trap over a period of time, we can calculate properties of the optical trap, such as its stiffness, and learn more about how the probe bead interacts with its environment—for example, in the case of being deep in solution, close to a pedestal bead, or tethered by PCDH15 or molecular anchors. This approach is called thermal force probing^{66,67}. We can record the diffusion of a probe bead in an optical trap in three dimensions (Figure 13A-D).

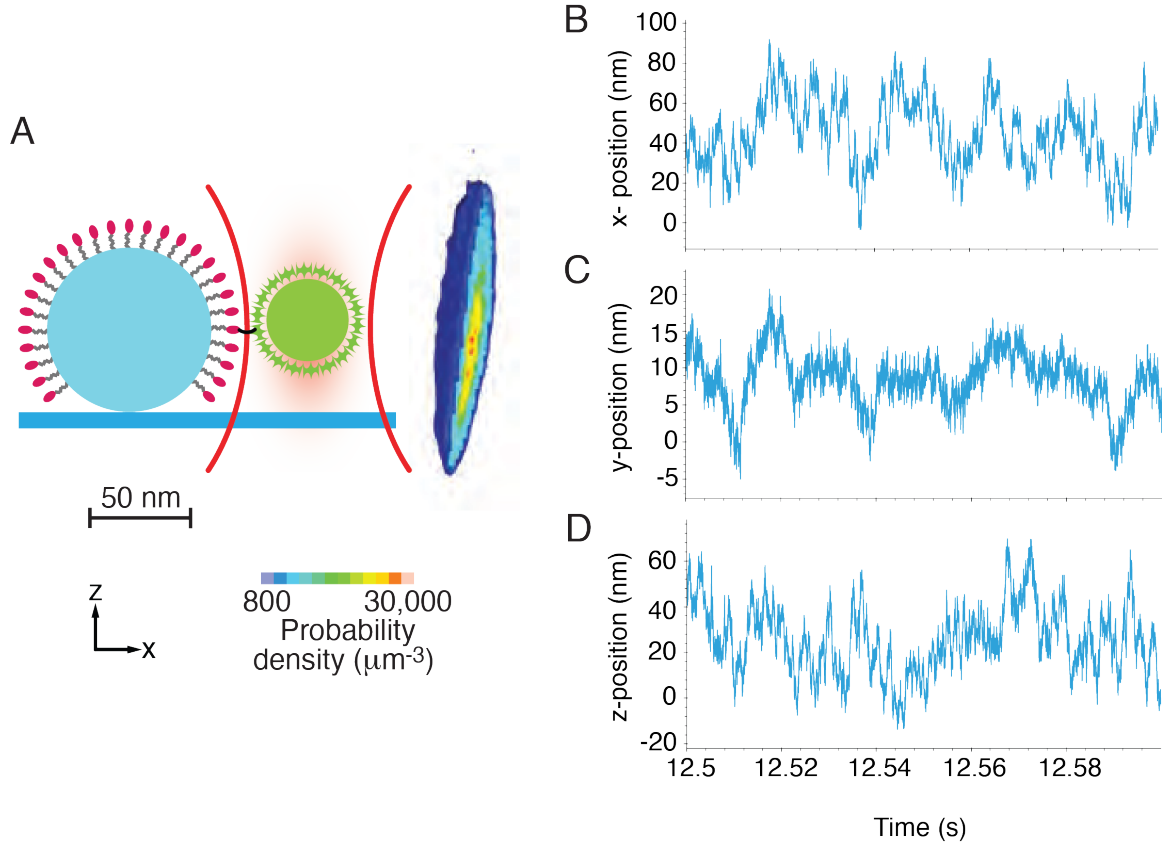


Figure 13. Diffusion of a probe bead tethered by molecular anchors.

(A) When the probe bead is tethered to a pedestal bead by the molecular anchors alone, its diffusion profile is restricted. *Figure adapted from Bartsch, Villasante, Hengel, et al. 2021.* (B, C, D) The x -, y -, and z -positions of the bead attached to the anchors alone at resting force (1 pN) can be recorded.

We can generate probability densities corresponding to the bead's position in the x -, y -, and z -directions, which follow the Boltzmann distribution

$$p(x, y, z) = A \cdot e^{-\frac{E(x,y,z)}{k_B T}}, \quad (2.13)$$

in which $p(x,y,z)$ is the probability density of the bead's position in direction x , y , or z , A is a constant, $E(x,y,z)$ is the optical trap's energy landscape in direction x , y , or z , k_B is the Boltzmann constant, and T is temperature. From the probability density of the probe bead's position in the optical trap in three dimensions, we can depict how often it visits various positions. Its probability density in three

dimensions is ovoid—the trapping potentials of the laser in the x - and y -directions are approximately equivalent, but the trapping potential in the z -direction is weaker owing to the shallower slope of gradient force in the z -direction⁶⁸.

When the probe bead is deep in solution, it is able to freely diffuse within the trapping potential of the laser (Figure 14A). But when the probe bead is brought next to a pedestal bead, such as during the course of an experiment, its diffusion becomes restricted owing to the presence of the pedestal bead on one side (Figure 14B). When a molecular tether comprising PCDH15 forms between the probe and pedestal beads, the diffusion of the probe bead is further restricted (Figure 14C). When the probe bead is bound to the pedestal bead by the molecular anchors alone, its diffusion is much further restricted owing to the lesser length of the anchors compared to PCDH15 alone (Figure 14D).

By solving Equation 2.13 for $E(x,y,z)$ we can generate the energy landscape of the optical trap in direction x , y , or z :

$$E(x, y, z) = -k_B T \ln[p(x, y, z)] \quad (2.14)$$

The corresponding energy profiles of the system change accordingly depending on whether the probe is untethered, tethered by PCDH15, or tethered by the molecular anchors alone (Figure 14E).

We can fit the energy landscape using the energy potential of a Hookean spring

$$U_{x,y,z} = \frac{1}{2}(k_x x^2 + k_y y^2 + k_z z^2), \quad (2.15)$$

in which $k_{x,y,z}$ is the spring constant of the optical trap in that particular direction. By solving for $k_{x,y,z}$ we can determine the spring constant of the position-sensing optical trap along one particular dimension.

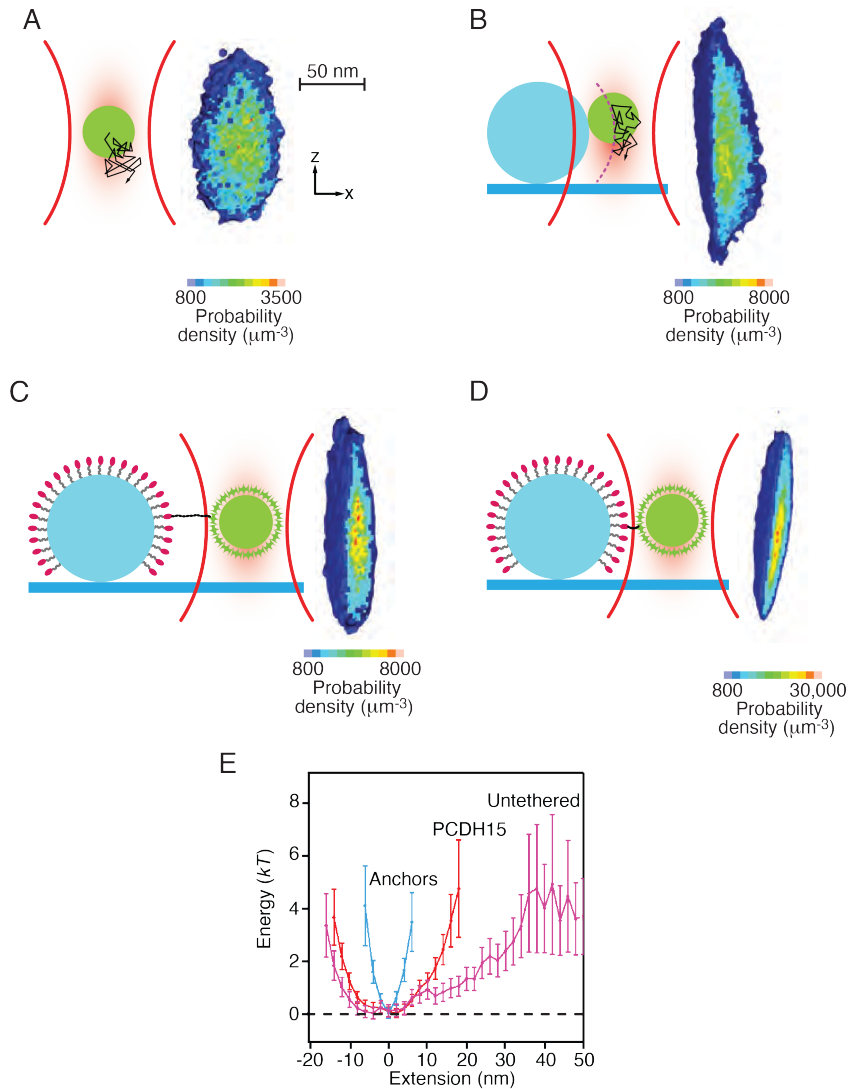


Figure 14. Thermal force probing.

(A) A schematic diagram (left) portrays the thermal diffusion of the probe in an optical trap. A section through the experimentally measured three-dimensional probability density (right) reveals the positions explored by the diffusing probe. Note the discrepancy in scale: the density distribution is magnified about 25X in comparison to the $1 \mu\text{m}$ probe. The arrangements, definitions of axes, and spatial scales are identical in the following three panels. (B) When the probe is brought into contact with the fixed pedestal, its diffusion is restricted. Flattening of the experimental probability density demarcates the surface of the pedestal.

(C), When the probe is affixed to the PEG-coated pedestal by a short linker, the linker further restricts diffusion of the probe. (D) In an actual experiment, the probe is attached to the pedestal by a PCDH15 monomer. The protein's extensibility allows the probe to explore a larger volume of space. (E) The experimentally determined probability distributions reflect the energy of the system for the probe at various positions. *Figure and caption adapted from Bartsch, Villasante, and Hengel et al. (2021).*

2.9 Stiffness and behavior of the molecular anchors alone

To investigate whether it is possible that PCDH15 and the tip link as a whole constitute a significant component of the gating spring, I had to determine the stiffness of PCDH15. In my optical trap experiments, PCDH15 was suspended between the pedestal and probe beads in series with the molecular anchors on either end. Therefore, it was necessary to first characterize the stiffness of the anchors alone to be able to distinguish it from the stiffness of PCDH15. Figure 15A shows an exemplary heatmap depicting the behavior of the molecular anchors alone during force ramps. The relationship between the extension and the applied force is linear over the experimental force range, implying that the entropic contribution to the extension of the anchors is minimal. This control experiment also confirms that no unfolding events originate from the molecular anchors, meaning that any unfolding events observed when PCDH15 lies in series with the molecular anchors must stem from PCDH15, not the anchors themselves. I could then characterize the stiffness of the molecular anchors as a function of force by finding the average inverse slope of the highly occupied state space of each dataset of the molecular anchors alone (Figure 15B).

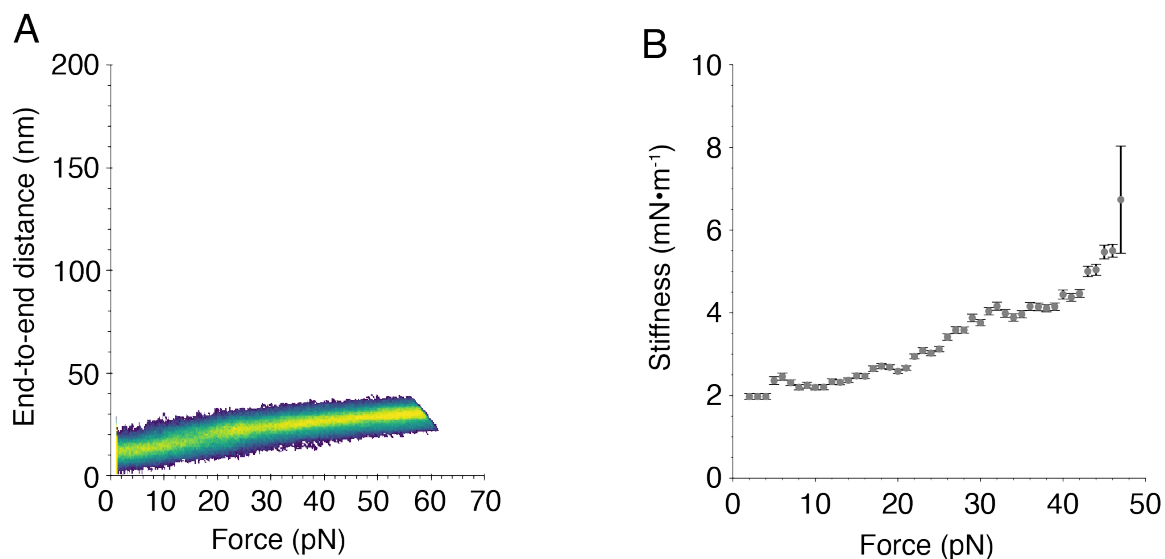


Figure 15. Behavior of the molecular anchors in the absence of PCDH15.

(A) A representative heatmap of the anchors alone shows that they exist in one conformational state. This behavior confirms that the anchors do not unfold within our experimental force range. (B) We determined the stiffness of the anchors as a function of force by finding the average inverse slope of the highly occupied state space of each dataset of the anchors alone (means \pm SEMs; $N = 3$). *Figure and caption from Villasante et al. (2023)⁵⁴.*

2.10 Materials and methods

Portions of this section have been excerpted from Villasante *et al.* (2023)⁵⁴ and Bartsch, Villasante, Hengel *et al.* (2021)⁶⁰, both of which I wrote in association with the listed co-authors.

2.10.1 Pedestal-bead functionalization

Pedestal beads had to be functionalized with SpyCatcher molecules in order to tether PCDH15 to them. First, 200 μ L of 1.5 μ m diameter amino silica particles (ASIP-15-10, Spherotech, Lake Forest, IL, USA) were washed twice in borax buffer (50 mM sodium tetraborate decahydrate, pH 8.5; B-9876, Sigma Aldrich), and resuspended in 100 μ L of borax buffer. The beads were incubated with rotation for one hour in order to deprotonate the amino groups on the surface of the beads.

Then 7 mg of SM(PEG)₁₂ (22112, ThermoFisher Scientific, Waltham, MA, USA) was combined with 60 µL borax buffer, added to the beads solution, and incubated with rotation for 30 minutes. After this, the beads were washed thrice with a HEPES-buffered saline solution (HBSS; 20 mM HEPES and 100 mM NaCl at pH 7.4) before being resuspended in HBSS to a final volume of 250 µL. Meanwhile, 0.5 mg of SpyCatcher (EOX004, Kerfast, Boston, MA, USA) was reduced with 120 µL immobilized TCEP disulfide reducing gel (77712, ThermoFisher Scientific, Waltham, MA, USA) for one hour with rotation. The supernatant was then removed and mixed with 100 mg/mL sulfhydryl-blocked bovine serum albumin (100-35, Lee Biosolutions, Maryland Heights, MO, USA). The beads and SpyCatcher protein were mixed and incubated with rotation at 4 °C overnight so that the maleimide residues on the pedestal beads could react with the cysteines in the SpyCatcher. The next morning, the beads were then washed thrice with HBSS and then 1 M L-cysteine was added and incubated while rotating for at least one hour to quench the maleimide groups. The beads were then washed thrice with HBSS and resuspended.

To ensure that SpyCatcher was successfully attached to the beads, we tested the functionalization with a dot-blot procedure. Beads were spotted onto a nitrocellulose membrane and allowed to dry. The peptide **Biotin-AviTag-GGGSGGS-SpyTag**, which comprises the anchors without PCDH15^{60,65}, was then spotted onto the beads, followed by incubation in horseradish peroxidase (HRP)-conjugated streptavidin (SA10001, ThermoFisher Scientific, Waltham, MA,

USA). Binding of the biotinylated peptide to the pedestal beads indicated successful functionalization.

2.10.2 Sample preparation for single-molecule experimentation

Each experiment was performed in a rectangular channel formed by two glass coverslips mounted onto a titanium chamber. The upper coverslip was a 22 mm x 22 mm #1.5 glass coverslip functionalized with *n*-hydroxysuccinimide (custom order, PolyAn, Berlin, Germany) whereas the lower was a circular, 35 mm-diameter #1.5 glass coverslip (custom order, Thorlabs, Newton, NJ, USA). Before performing an experiment, we needed to covalently attach the pedestals to the upper coverslip. This was accomplished by diluting the pedestal beads in a HEPES-buffered saline solution (HBSS; 20 mM HEPES and 100 mM NaCl at pH 7.4) and pipetting the bead solution onto the functionalized coverslip, where the amines in the SpyCatcher groups covalently bound to the *n*-hydroxysuccinimide on the coverslip. The beads were allowed to react for 5 min before any unbound beads were forcefully washed off with HBSS. A thin layer of residual liquid ensured that the surface did not dry. The chamber was then sealed by securing the lower coverslip with vacuum grease. After allowing the beads to react for at least 30 min, we added a blocking buffer solution containing 10 mg/mL sulfhydryl-blocked bovine serum albumin (100-35, Lee Biosolutions, Maryland Heights, MO, USA), 150 mM KCl, 10 mM HEPES, and either 3 mM CaCl₂, 20 μM CaCl₂, or 1 mM EDTA, depending upon the particular experiment, to reduce non-

specific binding. The chambers were blocked overnight at 4 °C and experiments were performed the following day.

The samples were incubated with protein prior to experimentation as previously described⁶⁵. In brief, protein was diluted into a blocking buffer solution containing 10 mg/mL sulfhydryl-blocked bovine serum albumin (100-35, Lee Biosolutions, Maryland Heights, MO, USA), 150 mM KCl, 10 mM HEPES, and either 3 mM CaCl₂, 20 μM CaCl₂, or 1 mM EDTA, depending upon the particular experiment, and flowed into the experimental chamber. The protein was allowed to incubate for 1 hr at 4 °C to allow the SpyTag on the protein to bind to SpyCatcher groups on the pedestal beads within the chamber.

Streptavidin-coated polystyrene beads 1 μm in diameter (CP01004, Bangs Laboratories Inc., Fishers, IN, USA), which we termed probe beads, were washed three times in the blocking buffer solution to remove additives from the bead storage solution. After any unbound protein had been washed from the pedestal beads with an excess of blocking buffer solution, we flowed into the chamber a solution containing probe beads and an oxygen-scavenging system. The oxygen-scavenging system, which comprised 18 mM D-glucose, 1000 U/mL pyranose oxidase, and 500 kU/mL catalase (P4234 and 219261 respectively, Millipore Sigma, Burlington, MA, USA), protected against the phototoxic effects of singlet oxygen and maintained a constant pH in the sample chamber. The chamber was then sealed with vacuum grease to prevent evaporation during an experiment.

2.10.3 Photonic-force microscope

The photonic-force microscope used in these studies, with sub-nanometer spatial resolution and microsecond temporal resolution, has been described in detail^{60,65}. Its beampath is illustrated in Figure 16. The force-producing beam (magenta), which originates from a 400 mW 852 nm laser (DL852-400, CrystaLaser, Reno, NV, USA), first passes through a Faraday isolator (IO-3D-850-VLP, Thorlabs Inc., Newton, NJ, USA) to prevent reflection from light back into the laser. The light traverses two wave plates to polarize the beam in the perpendicular direction before reaching a polarizing beam-splitting cube that removes any light that is incorrectly polarized. A Pockels cell (Laser Modulators LM 13, 8450-202-301-5, Qioptiq, Feldkirchen, Germany) permits adjustment of the beam's intensity and thus of the holding force acting on the probe bead. After passing through a beam expander (GBE05-B, Thorlabs), the beam is cleaned with another polarizing beam-splitting cube that directs inappropriately polarized light into a dump. A non-polarizing beamsplitting cube reflects 10 % of the beam to a photodiode (Öffner MSR Technik, Plankstadt, Germany) that measures the laser's power and allows determination of the optical trap's spring constant. After passing through a shutter, the beam reaches a beam steering lens that allows positioning in the plane of the specimen with a piezoelectrical nanopositioning stage (P-282.30, Physik Instrumente GmbH, Karlsruhe, Germany). A dichroic mirror (ZT775sp-2p-UF3, Chroma Technology Corporation, Bellow Falls, VT, USA) then directs the beam into the main optical path, where it traverses an upper objective lens and impinges

upon the specimen. After exerting force on the probe bead, the beam is captured by a lower objective lens, reflected by a dichroic mirror, and intercepted by an 852 nm filter.

The position-measurement beam (red) from a 500 mW 1064 nm laser (Mephisto, Coherent, CA, USA) passes through a Faraday isolator, a beam expander (Sill Optics GmbH, Wendelstein, Germany), a neutral-density filter (Thorlabs) to attenuate the power, and a shutter. A dichroic mirror then joins this beam with the 852 nm force-producing beam. After traversing the upper objective lens (OL UPSAPO 60XW, NA 1.2, Olympus Corporation, Tokyo, Japan), the specimen, and the lower objective lens (LUMPLFLN 60XW, Olympus), the position-sensing beam is reflected from a dichroic mirror and passed through a filter (FF01-937/LP-25, Semrock Inc., Rochester, NY, USA) that transmits only light from the 1064 nm laser. After passing through a reverse telescope to reduce its size, the beam impinges on a quadrant photodiode (Öffner MSR Technik, Plankstadt, Germany).

The observation path (green) originates from a light-emitting diode, passes through a condenser lens, and enters the main optical path. After traversing the objective lenses and specimen, the light is transmitted by the dichroic mirrors associated with the two laser-beam paths and is focussed by a tube lens (Achromate VIS, G322246000, Qioptiq) onto the active surface of the water-cooled CMOS camera (pco.edge 5.5, PCO-TECH Inc., Romulus, MI, USA).

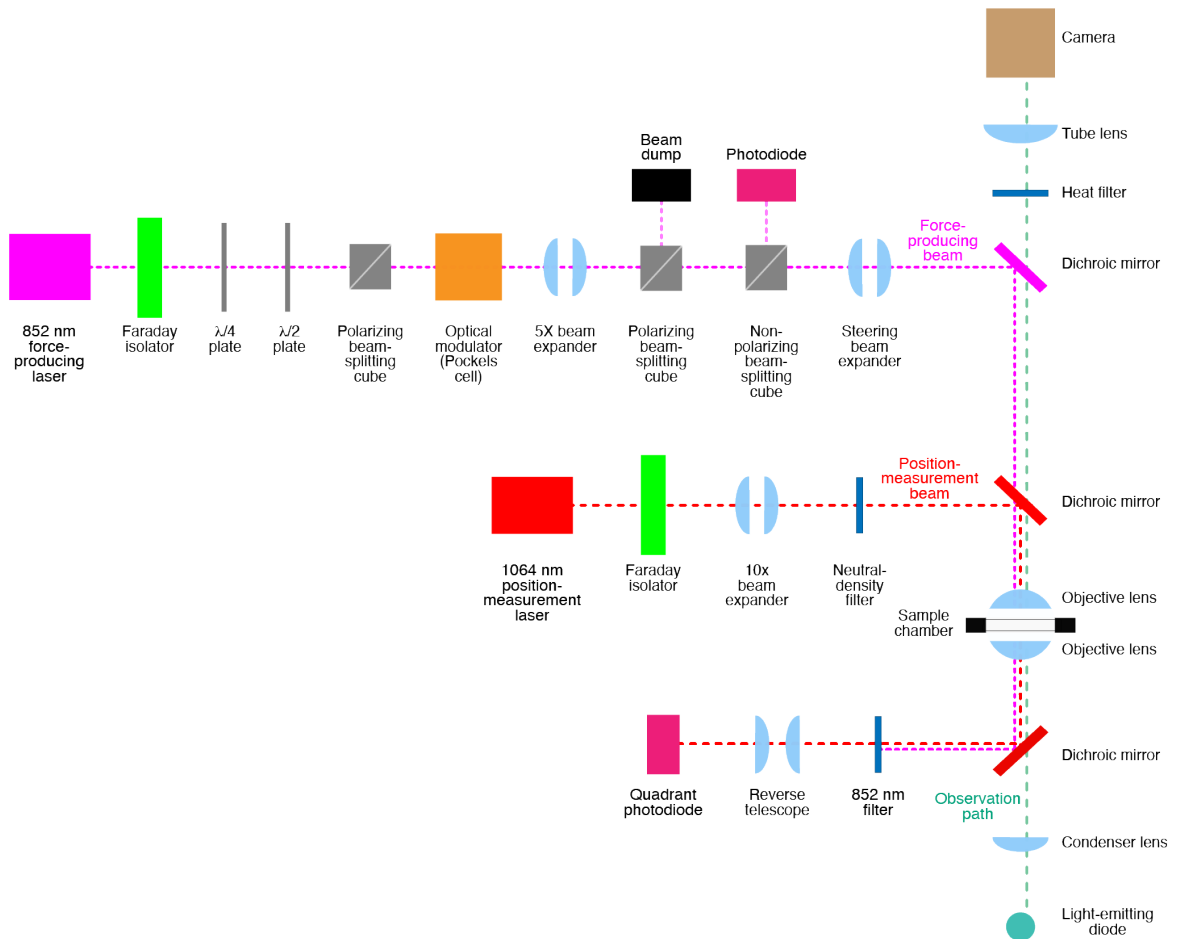


Figure 16. Optical beam paths of the photonic force microscope.

The beam path of the 852-nm force-producing laser is depicted in magenta, the path of the 1064-nm position-measurement laser is shown in red, and the optical observation path is shown in green. The shutter in the 852 nm laser path is located in between the steering beam expander and the dichroic mirror.

2.10.4 Force-ramp experiments

We started each experiment by trapping a probe bead deep in solution with the 1064 nm position-sensing laser. We next calibrated the stiffness of the force-producing laser and the sensitivity of the position detector as described above. The probe bead was brought 250 μm from the surface of the functionalized coverslip so that the equators of the pedestal and probe beads were at the same height. We

brought the probe bead close to the pedestal bead and performed an offset calculation to account for the influence of the pedestal bead on the position signal of the probe bead⁶⁰. The probe bead was then allowed to diffuse along the edge of the pedestal bead. If a tether formed, the diffusion profile of the probe bead became severely constricted⁶⁰.

Before beginning data collection, we initiated drift correction by focusing the camera on a single pedestal bead elsewhere in the field of view, but far from the tether. By tracking the movement of this distant pedestal bead, we could correct the position of the nano-positioning stage upon which the sample chamber was mounted. The optical trap of the force-producing laser was displaced by 200 nm along the axis of force application, and a brief pulse of force was delivered to the tether to break any non-specific bonds. We then initiated the force-ramp protocol, which applied force at constant increasing and decreasing rates during the respective extension and relaxation phases of each cycle. The extension and relaxation phases each lasted 0.35 s. Between successive cycles, the construct was held for 2 s at a low resting force of 1 pN to allow time for the protein to refold. The loading rate of force application was approximately $150 \text{ pN}\cdot\text{s}^{-1}$. The signals from the position-sensing and force-producing lasers were sampled at a frequency of 100 kHz.

2.10.5 Control of non-specific bead interactions

For appropriate interpretation of single molecule data, it was important to ensure that the probe and pedestal beads did not adhere to one another non-specifically.

We therefore tested whether the streptavidin-coated probe beads (CP01004, Bangs Laboratories, Fishers, IN, USA) would bind to the SpyCatcher-coated pedestal beads. Out of 33 attempts at tether formation over three experiments on different days, none resulted in a tether. This result largely excluded the possibility that we were measuring non-specific bead interactions.

2.10.6 Determination of the zero position of extension

To accurately determine the extension of the protein in series with the molecular anchors, we first had to determine the zero position of extension. For each dataset, we concatenated the position signals when the construct was held at a low force of 1 pN during the inter-ramp periods. The position signals at this low resting force were approximately Gaussian in distribution, so we set the zero position to be three standard deviations below the mean position of the construct at low resting force.

2.10.7 Statistics of tether formation

We wished to minimize the possibility that the data we recorded corresponded to multiple protein tethers. To accomplish this, we modeled the formation of tethers as a Poisson process to calculate the probability of forming only one tether during a given interval. The probability of an event happening k times in an interval is given by

$$P(k) = \frac{\lambda^k e^{-\lambda}}{k!}, k = 0, 1, 2, \dots \quad (2.16)$$

Here λ is the mean number of tethers in the interval, which we could not measure directly. To have 90 % probability of getting a single tether when a (single or multiple) tether is formed, we first solved for λ in the following relation:

$$\frac{P(k = 1)}{P(k > 0)} = \frac{\lambda e^{-\lambda}}{1 - e^{-\lambda}} = 0.9. \quad (2.17)$$

We obtained $\lambda = 0.207$. We then used $\lambda = 0.207$ to calculate the probability of forming a possible tether, $P(k > 0)$, regardless of number of actual tethers:

$$P(k > 0) = 1 - e^{-\lambda}. \quad (2.18)$$

The result is $P(k > 0) = 0.187$. In sum, if 18.7 % of tethering attempts result in the formation of at least one tether, the probability of this tether being a single tether is 90 %. We therefore adjusted the concentration of protein empirically so that roughly one in five binding attempts resulted in a tether.

2.10.8 Identifying conformational changes

The algorithm for conformational change detection was previously described in detail⁶⁵. Each dataset was first split into single cycles, and each cycle further split into its constituent extension and relaxation phases. The data were then smoothed using a Savitzky-Golay filter with a window of 101 points, reducing the resolution of the data from 10 μ s to 1 ms. A conformational change was then detected at point i in the data if

$$|\langle x \rangle_{before} - \langle x \rangle_{after}| > 4 \frac{\sigma_{before} + \sigma_{after}}{2}, \quad (2.19)$$

in which $\langle x \rangle_{before}$ and $\langle x \rangle_{after}$ are the average extension values of a window of 1000 points before and after point i , respectively, and σ_{before} and σ_{after} are the corresponding standard deviations. If the difference in the average extensions before and after point i exceeded four times the average standard deviations of the position before and after point i , then a conformational change was called.

CHAPTER 3. Ca²⁺ sensitivity of PCDH15 under physiological forces

PCDH15 exists as a dimer in the tip link, connecting to the MET complex at its C-terminus and to CDH23 at its N-terminus. Its structure is sensitive to Ca²⁺: the short linker regions intervening between its constituent domains can bind up to three ions of Ca²⁺. These ions not only bind to the linker regions, but also have contacts with the neighboring domains that stabilize the structure against unfolding. The concentration of Ca²⁺ in the cochlear endolymph^{69–71} is approximately 20 μM, a value much lower than that in the rest of the body⁷², and the dissociation constant of Ca²⁺ at the linker regions is in the range of tens to hundreds of micromolar^{41,73}. I was therefore interested in exploring the role of Ca²⁺ in the modulation of PCDH15 mechanics.

3.1 Previous work: Monomeric PCDH15 exhibits Ca²⁺ dependence

Previous work by members of our group examined the Ca²⁺ dependence of a monomeric murine PCDH15 construct to force⁶⁵ using the PFM described in Chapter 2. In that work, a point mutation was introduced into EC3 to disrupt the dimerization interface³⁸ and the PICA domain was removed (Figure 17) to yield a monomer of PCDH15.

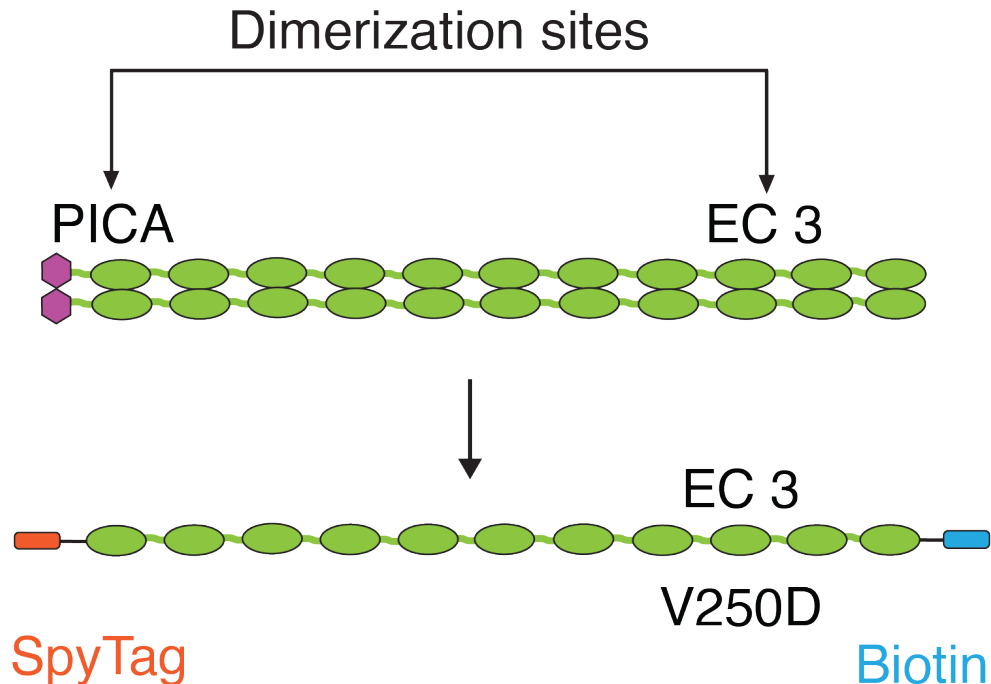


Figure 17. Creation of monomeric PCDH15.

To create monomeric PCDH15, the dimerization sites at the PICA and EC3 domains were disrupted by removing the PICA domain and introducing a point mutation, V250D, into EC3 to disrupt the dimerization interface³⁸.

The mechanics of monomeric PCDH15 were examined at three representative Ca^{2+} levels: 3 mM, a saturating concentration of Ca^{2+} meant to occupy all available Ca^{2+} binding sites; 20 μM , a physiological Ca^{2+} concentration^{69,70}; and in the absence of Ca^{2+} but in the presence of 1 mM EDTA, a Ca^{2+} chelator. At a saturating level of Ca^{2+} , two types of unfolding events were commonly seen⁶⁵, one resulting in an extension of 4.0 ± 0.2 nm and the other resulting in an extension of 15.8 ± 0.7 nm (Figure 18 A, D, G). Both events were less than the length expected for unfolding of one full EC domain, which would be in the range of 33 to 45 nm, depending on the domain. At a physiological concentration of Ca^{2+} , 20 μM , an additional class of unfolding was observed: the unfolding of an entire EC domain,

which resulted in an extension of 35 ± 1 nm (Figure 18 B, E, H). In the complete absence of Ca^{2+} , a class of unfolding events corresponding to EC domain unfolding were also observed along with other unassigned changes in end-to-end distance (Figure 18 C, F, I) .

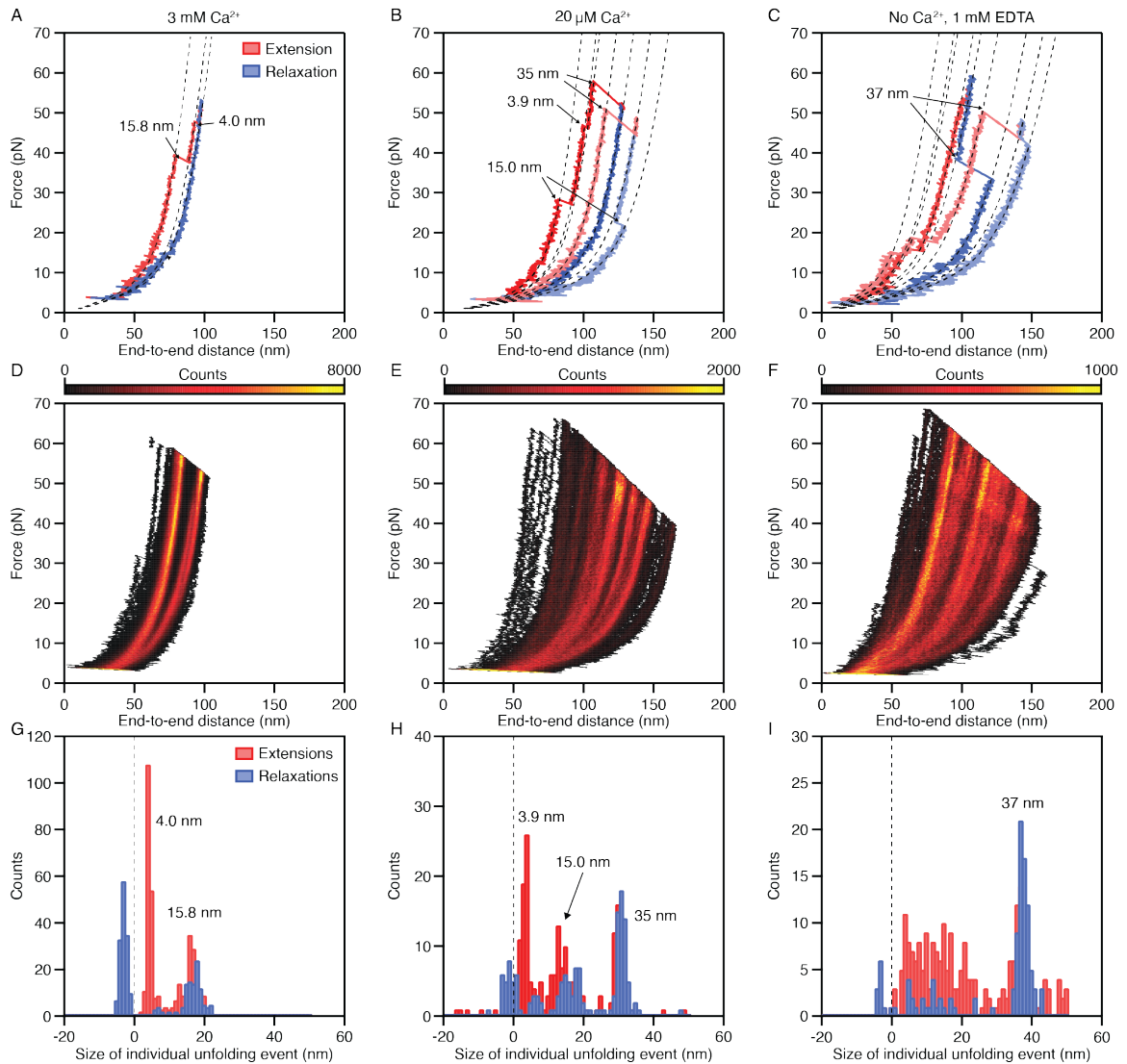


Figure 18. The behavior of monomeric PCDH15 was Ca^{2+} -dependent.

(A-C) Illustrative single-cycle trajectories from monomeric PCDH15 show how the unfolding behavior changes with Ca^{2+} concentration. Similar classes of unfolding can be seen across the different conditions. Note that the data presentation differs from elsewhere in this text: the end-to-end distance and force axes are transposed, and the heatmap color scheme is different. (D-F) Illustrative heatmaps at each concentration of Ca^{2+} convey the increasing conformational heterogeneity and classes of unfolding events as the Ca^{2+} concentration is decreased. (G-I) At each level of Ca^{2+} , analysis of the size of individual unfolding events that occur show that certain sizes of unfolding events occur throughout the different Ca^{2+} conditions. *Figure adapted from Bartsch et al. (2019).*

3.2 Construction of dimeric PCDH15

Because of the importance of Ca^{2+} for the structure of PCDH15 and because of the clear Ca^{2+} dependence of the response of PCDH15 monomers to force, I wanted to investigate whether dimeric PCDH15, as it exists within the cochlea, exhibits a similar Ca^{2+} dependence. PCDH15 naturally dimerizes at EC3 and the PICA domain. To ensure that force was distributed equally across both strands of the PCDH15 dimer, we devised a construct in which the two strands of PCDH15 are attached to one another at each end by paired disulfide bonds derived from the Fc hinge region of human immunoglobulin⁷⁴. I then performed force ramp experiments on PCDH15 dimers across the three representative Ca^{2+} concentrations in which the monomer experiments were performed in. We used the murine PCDH15 sequence expressed from mammalian cells to preserve post-translational modifications as they would occur in humans, such as glycosylation.

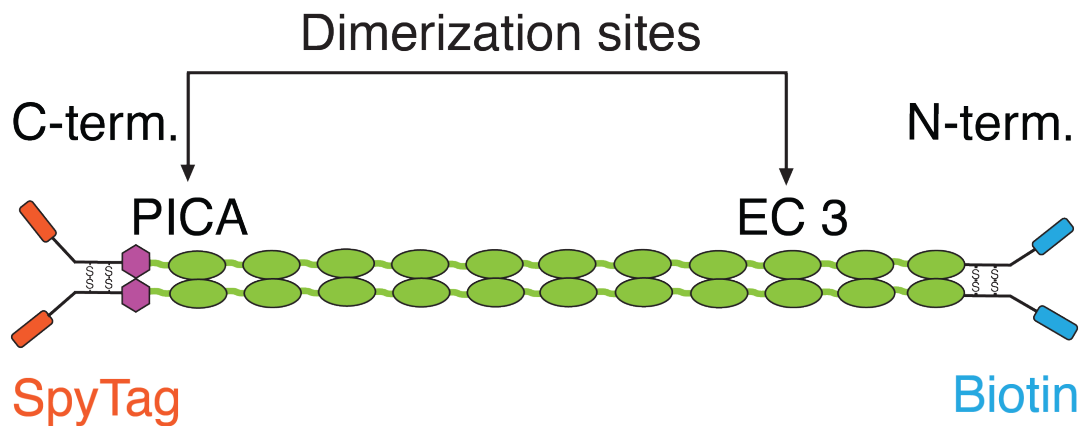


Figure 19. A PCDH15 construct to ensure proper force distribution during optical trap experiments.

We added paired disulfide bonds from the Fc hinge region of IgG to the N- and C-termini of PCDH15. This arrangement ensures that force is distributed evenly across both strands of the dimer, no matter how the functional tags attach to the beads at either end.

3.3 Materials and methods

Portions of this section have been excerpted from Villasante *et al.* (2023), which I wrote in association with the listed co-authors⁵⁴.

3.3.1 Plasmid design

Constructed by Gibson assembly⁶⁵, the wild-type PCDH15 plasmid was organized as: **signal peptide-QYDDDWQYED-AviTag-IgG hinge region-GSGSGS-PCDH15 (EC1-11 and PICA)-GSGSGS-IgG hinge region-SpyTag-8xHis**, in which the sequence QYDDDWQYED represents the first ten amino-acid residues of PCDH15. We used isoform 1 from *Mus musculus* (UniProt entry Q99PJ1) as the PCDH15 sequence. The native signaling peptide and the first ten residues ensured proper cellular trafficking of PCDH15 for export to the membrane. The AviTag had the sequence **GLNDIFEAQKIEWHE**. The human IgG hinge region⁷⁴ had the sequence **DKHTCPCPPELLGGP** and ensured that the two strands of the dimer bound each other so that force would be distributed evenly across both strands during experiments with the optical trap. The first ten amino acids of our EC1 sequence were **QYDDDWQYED** and the last ten amino acids of our PICA sequence were **RGESLGYTEG**. The SpyTag⁷⁵ had sequence **AHIVMVDAYKPTK**.

3.3.2 Protein purification

FreeStyle 293F cells (R79007, ThermoFisher Scientific, Waltham, MA, USA) were grown at 37 °C, 150 rpm, 8 % CO₂ in FreeStyle 293 expression medium with 0.1 % antibiotic and antimycotic (12338018 and 15240096, ThermoFisher Scientific,

Waltham, MA, USA). When the cultures reached a density of 0.8-1.0 million cells per milliliter, they were transfected by mixing Opti-MEM I reduced serum medium (31985062, ThermoFisher Scientific, Waltham, MA, USA) with PEI MAX (24765-100, Polysciences, Inc., Warrington, PA, USA) and 250 µg plasmid per 500 mL of medium. The transfected cells were then grown for 7 d.

The supernatant was harvested by centrifugation and filtered through a 0.22 µm PES filter (S2GPU05RE, Millipore Sigma, Burlington, MA, USA). Protein was purified from the supernatant by a two-step protocol. First, the supernatant was mixed with Ni Sepharose 6 Fast Flow resin (17531801, Cytiva, Marlborough, MA, USA) and incubated for 30 min. The beads were then loaded onto a chromatography column (7372522, Bio-Rad, Hercules, CA, USA) and washed with ten column volumes of wash buffer solution (150 mM NaCl, 10 mM Tris-HCl, 20 mM imidazole, and 3 mM CaCl₂ at pH 7.4). The protein was eluted from the resin using elution buffer solution (150 mM NaCl, 10 mM Tris-HCl, 250 mM imidazole, and 3 mM CaCl₂ at pH 7.4). The peak fractions were pooled, dialyzed into imidazole-free wash buffer, and concentrated to 500 µL. The sample was run over a Superdex 200 10/300 GL size-exclusion column (28990944, Cytiva, Marlborough, MA, USA) on an ÄKTA pure 25 L (29018224, Cytiva, Marlborough, MA, USA). The peak fractions were collected, pooled, concentrated, and run on an SDS-PAGE gel to verify size. The protein was biotinylated at the AviTag (BirA500 biotin-protein ligase reaction kit, Avidity, Aurora, CO, USA) and the biotinylation was confirmed by immunoblotting. The protein was diluted to 50%

with glycerol and aliquoted into single-use tubes and flash frozen in liquid nitrogen for storage at -80 °C for up to one year.

3.3.3 Negative staining transmission electron microscopy

For electron microscopic imaging we first rendered the formvar- and carbon-coated copper grid surfaces (FCF150-Cu-50, Electron Microscopy Sciences, Hatfield, PA, USA) hydrophilic using a glow-discharge system. All grids were then processed within an hour of glow-discharge treatment. The protein of interest was diluted to 0.005 mg/mL and applied to the hydrophilic surface of the grid for 30 s. The grid was then touched sequentially to three drops of water, with blotting of the grid's edge after each drop. Finally, each grid was touched sequentially to two drops of 20 mM uranyl formate stain (22450, Electron Microscopy Sciences, Hatfield, PA, USA) and held 20 s at the last drop. Excess liquid was removed from the grid surface by vacuum. The grids were imaged using a FEI TECNAI G2 Spirit BioTwin transmission electron microscope (ThermoFisher Scientific) with an AMT BioSprint29 29 Megapixel camera system (Woburn, MA, USA) at the Rockefeller University's Electron Microscopy Resource Center.

3.3.4 Fitting force ramp data using a saturation model with an enthalpic stiffness term

To quantify unfolding changes, we used a saturation model⁷⁶ with a Hookean spring term to model the data. In this model, the entropic extension of PCDH15 is given by the first, saturable term and the enthalpic stiffness limit is given by the second term, the extension of a Hookean spring:

$$x = \frac{x_E}{1 + \frac{F_{HALF}}{F}} + \frac{F}{K}. \quad (3.1)$$

Here the maximal entropic extension of PCDH15 is given by x_E ; F_{HALF} is the force at which entropic extension is halfway complete. The contribution of enthalpic stiffness is given by the second term, the extension of a linear spring of stiffness K under force F . The enthalpic spring constant K was determined for each Ca^{2+} concentration by averaging the inverse spatial derivatives at forces exceeding 30 pN for every cycle in all datasets in a particular condition. This process is described in detail in Section 3.3.5.

To compute the size of the unfolding events, each force-ramp cycle was first split into extension and relaxation phases, then further segmented by the unfolding events that occurred. The first segment, before any unfolding occurred, was fit for x_E and f_{HALF} , with K set to the average value for the condition to which the dataset belonged. For the subsequent segments within the same phase of a cycle, f_{HALF} was held constant at its first segment value while fitting for x_E alone. The size of the unfolding events could then be found by finding the difference between the x_E values of successive segments.

3.3.5 Calculation of the enthalpic stiffness

Only portions of cycles before any unfolding occurred were considered in order to calculate the enthalpic stiffness of the fully folded protein. To exclude the effects of entropic stiffness, we examined only data at 30 pN and above after observing that extension was linear in a high-force range. We calculated the average line profile through the segment and excluded any segments corresponding to less

than 5 pN in length. The average line profile was further smoothed using a first-order Savitzky-Golay filter with a window matching the length of the segment. To find the average enthalpic stiffness values, we calculated the inverse spatial gradient of the smoothed segment and removed outliers that were greater than or less than 1.5 times the inter-quartile range. We averaged over all cycles in all datasets corresponding to each construct and condition. The resultant stiffness values corresponded to the entire construct—the protein in series with the molecular anchors tethering it to the beads at each end, which could be decomposed into its constituent parts using the following equation:

$$\frac{1}{k_{CONSTRUCT}} = \frac{1}{k_{ANCHORS}} + \frac{1}{k_{PCDH15}}. \quad (3.2)$$

Solving for k_{PCDH15} , we could calculate the stiffness of PCDH15 alone, and we obtained values of $40.6 \pm 10.3 \text{ mN}\cdot\text{m}^{-1}$ (mean \pm SEM; $N = 5$ datasets; $n = 990$ segments), $6.2 \pm 0.4 \text{ mN}\cdot\text{m}^{-1}$ (mean \pm SEM; $N = 4$ datasets; $n = 587$ segments), and $5.7 \pm 0.3 \text{ mN}\cdot\text{m}^{-1}$ (mean \pm SEM; $N = 6$ datasets; $n = 252$ segments) for wild-type PCDH15 at saturating (3 mM Ca^{2+}), physiological ($20 \text{ }\mu\text{M Ca}^{2+}$), and no Ca^{2+} (1 mM EDTA), respectively.

3.4 Results

3.4.1 Transmission electron microscopy studies of PCDH15 across three representative Ca^{2+} concentrations

After purifying PCDH15, I performed negative staining transmission electron microscopy (TEM). This allowed me to assess the quality of each batch of purified

protein, as well as examine how the structure of PCDH15 changed depending on the concentration of Ca^{2+} within the buffer.

At a saturating concentration of Ca^{2+} , 3 mM, PCDH15 exists predominantly as rigid-appearing dimers (Figure 20A). There is a small gap between the two strands, likely owing to the dimerization sites at EC3 and the PICA domain, which could allow the intervening region to diffuse about (Figure 20D). Otherwise, the two strands appear very closely associated with each other at this level of Ca^{2+} . However, when the Ca^{2+} is lowered to a physiological level of 20 μM , the two strands of the dimer bow apart, creating a larger gap between them (Figure 20B). This gap likely reflects the increased conformational heterogeneity of PCDH15 as a result of the loss of some of the stabilizing effect of Ca^{2+} binding to the inter-domain linker regions. When Ca^{2+} is removed completely from the solution but when a Ca^{2+} chelator is added (1 mM EDTA), the two strands of the dimer separate even more than at physiological Ca^{2+} , creating an even larger gap between them and causing the PCDH15 molecules to appear almost circular (Figure 20C). This large gap between the two strands suggests that in the complete absence of Ca^{2+} , PCDH15 is able to explore a wider range of conformational states than it is at higher levels of Ca^{2+} .

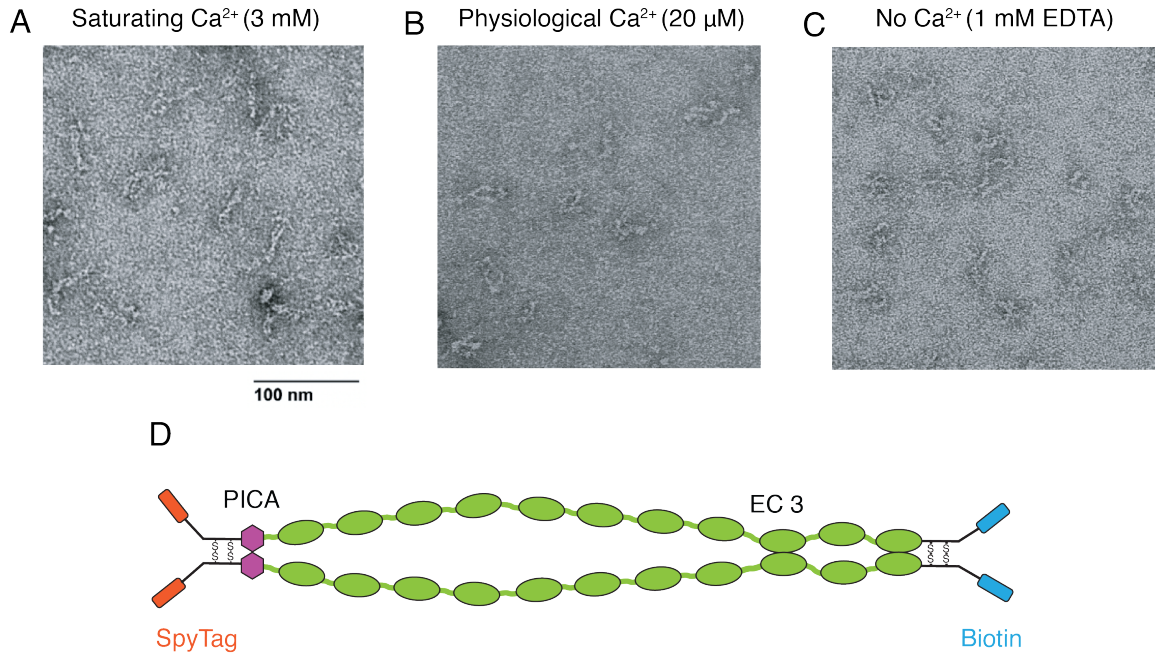


Figure 20. Transmission electron microscopy of PCDH15 dimers revealed structural differences across Ca^{2+} concentrations.

(A) At a saturating Ca^{2+} concentration, the PCDH15 dimers are predominantly linear and have a small gap between their strands. (B) In a physiological level of Ca^{2+} , the gap between the two strands of the dimer is enlarged. (C) In the absence of Ca^{2+} , the two strands of the dimer bow outwards from each other even more than at higher levels of Ca^{2+} . (D) The gaps seen on TEM images likely result from the arrangement of the dimerization sites of PCDH15. The portion of the protein between EC3 and the PICA domain is not held together, so it likely exhibits conformational degrees of freedom that depend on Ca^{2+} concentration.

These results show a clear dependence of PCDH15 structure on Ca^{2+} concentration. The depletion of Ca^{2+} from the inter-domain linker regions likely results in increased flexibility of the linkers and allows the EC domains more degrees of freedom to rotate about one another. The two strands of the dimer can consequently separate from each other increasingly as the Ca^{2+} is decreased. The dependence of PCDH15 structure on the Ca^{2+} concentration seen by transmission electron microscopy suggests that PCDH15 also has a functional Ca^{2+} dependence when examined using the optical trap.

3.4.2 PCDH15 at saturating Ca^{2+}

Parts of this section have been adapted from Villasante *et al.* (2023), which I wrote in association with the listed co-authors⁵⁴.

As exhibited both by the representative cycles (Figure 21A-C) and by the single bright branch on a representative heatmap (Figure 21D), PCDH15 underwent little unfolding at a saturating level of Ca^{2+} . At low forces, PCDH15 extended easily in response to applied force, a behavior that reflected entropic elasticity owing to the straightening of the molecule's thermal undulations. At higher forces, after most entropic degrees of freedom had been pulled out, the relationship between the end-to-end distance and the applied force became nearly linear. The remaining extensibility represented the enthalpic, or Hookean, stiffness of PCDH15.

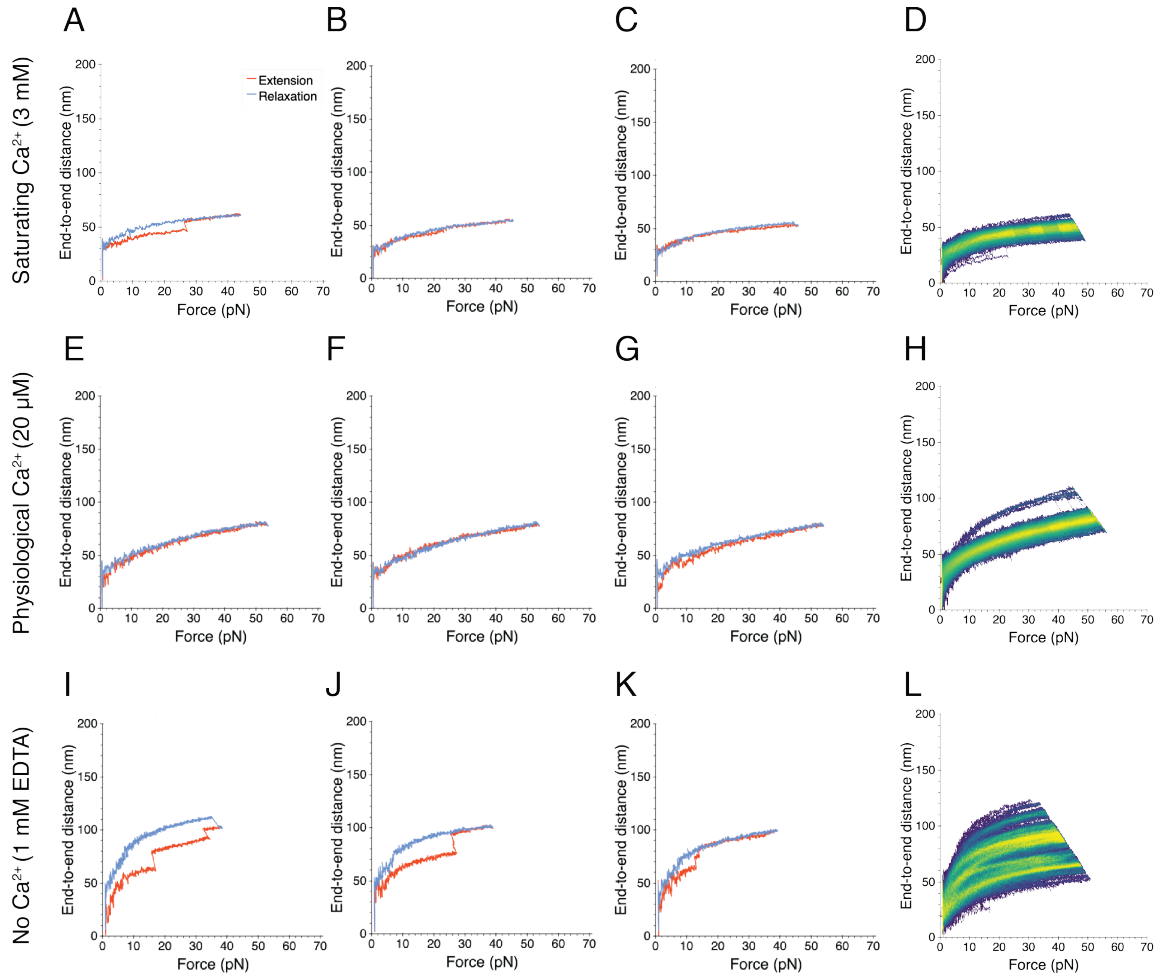


Figure 21. Summary of the response of dimeric PCDH15 to physiological forces across three important Ca^{2+} concentrations.

(A-C) Individual successive force ramp cycles of PCDH15 at a saturating level of Ca^{2+} revealed little unfolding and a fairly stiff molecule. (D) The single bright branch on the heatmap indicates that PCDH15 existed predominantly in one conformation at this level of Ca^{2+} . (E-G) At a physiological concentration of Ca^{2+} , PCDH15 extended more easily in response to force—meaning that it was softer—than at a higher Ca^{2+} level. (H) Despite the softer response of PCDH15 to force, it was largely in one conformation at this concentration of Ca^{2+} , as can be seen from the one bright branch on the heatmap. (I-K) When Ca^{2+} is removed completely, many unfolding events of various magnitudes occurred. (L) The numerous conformational states of PCDH15 in the absence of Ca^{2+} were evident from the many bright branches on the illustrative heatmap.

To quantify the unfolding changes that occurred, I used Equation 3.1 (reproduced here) to fit the data:

$$x = \frac{x_E}{1 + \frac{f_{HALF}}{F}} + \frac{F}{K}.$$

Here the maximal entropic extension of PCDH15 is given by x_E and f_{HALF} is the force at which entropic extension is halfway complete. The contribution of enthalpic stiffness is given by the second term, the extension of a linear spring of stiffness K under force F . The value of K was determined by averaging the inverse spatial derivatives at high force for every cycle of all data sets at each Ca^{2+} concentration. Details about the fitting are in Section 3.3.4. Each dataset was split into individual force ramp cycles, and each force ramp cycle was split into its constituent extension and relaxation phases (Figure 22A). Each extension and relaxation phase was further segmented by any unfolding changes that occurred using Equation 2.19 (Figure 22B). I fit each resultant segment using Equation 3.1. By finding the difference in x_E between subsequent segments, I could get the size of the conformational change that occurred (Figure 22C).

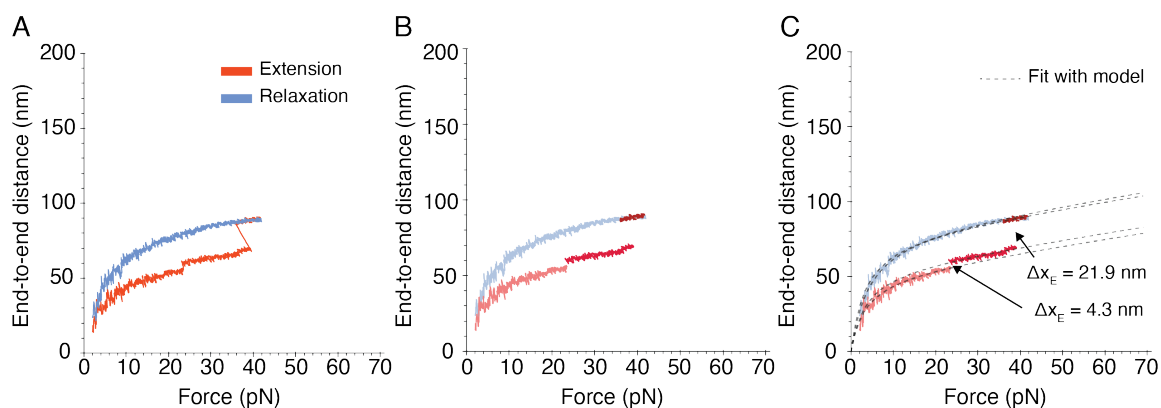


Figure 22. A saturation model with an enthalpic stiffness term can be used to fit segmented cycles to determine the size of unfolding events.

(A) After each dataset has been split into its constituent force ramp cycles, each cycle is further split into its extension (red) and relaxation (blue) phases. (B) Using Equation 2.19, each phase is then split by the conformational changes that occur. The different shades of red indicate different segments of the extension phase, demarcated by unfolding events. (C) Equation 3.1 can then be used to fit each segment in both the extension and relaxation phases of the force ramp cycle. By finding the difference in x_E between subsequent segments, we can determine the size of the unfolding event that occurred.

At a saturating concentration of Ca^{2+} , 3 mM, only a few discrete unfolding events occurred and their magnitudes were relatively small. These unfolding events separated into two classes, one at 2.0 ± 0.1 nm and the other at 6.6 ± 0.1 nm (means \pm SEMs; $N = 5$ datasets; $n = 140$ events; Figure 23A). I then asked whether these discrete unfolding events happened in succession within the same cycle, which would suggest the occurrence of a larger unfolding event through a multi-step process. I summed the total unfolding each cycle and found that the pattern of total unfolding per cycle was similar to the pattern of individual unfolding events. The events were predominantly below 20 nm, with events separating into two predominant classes: one at 1.8 ± 0.1 nm and the other at 6.3 ± 0.2 nm (means \pm SEMs; $N = 5$ datasets; $n = 131$ events; Figure 23B). The similarity of the

magnitude of discrete unfolding events compared to the summed unfolding per cycle suggests that the unfolding events in each cycle occurred primarily in single instances, rather than a multi-step unfolding process. The unfolding events could correspond to unfolding of the inter-domain linker regions, which—because they lack secondary structure—are likely to be the first components of PCDH15 to unfold under force. Individual linker regions measure between 1 nm and 3 nm when extended, so it is plausible that the unfolding of an individual or a few linker regions gave rise to the unfolding events that we observed. Furthermore, not all the linker regions bind three Ca^{2+} —some bind none whereas others bind one or two ions⁴¹—so that we might have observed extension of these linker regions even at a saturating level of Ca^{2+} . It is also possible that the small extensions reflected the straightening of the kinked EC9-10 linker⁷⁷, which does not bind Ca^{2+} and could extend up to 4 nm. I next asked whether there was any relationship between the size of individual unfolding events and the force at which they occurred. I found that unfolding events corresponding to the 2.0 nm and 6.6 nm classes occurred often between 10 pN and 20 pN, whereas events corresponding to the 2.0 nm class of unfolding events occurred across a broader range of forces (Figure 23C).

3.4.3 PCDH15 at a physiological Ca^{2+} concentration

Parts of this section have been adapted from Villasante *et al.* (2023), which I wrote in association with the listed co-authors⁵⁴.

As at a saturating concentration of Ca^{2+} , PCDH15 unfolded infrequently at a physiological Ca^{2+} concentration of 20 μM (Figure 21E-G). Nevertheless, at that

concentration PCDH15 was strikingly more extensible than at a saturating level of Ca^{2+} (Figure 21H). In other words, despite the scarcity of unfolding events, the dimer was softer at the lower concentration of Ca^{2+} . This finding was surprising, for we had expected an increase in compliance to emerge through more frequent unfolding events. This observation might reflect the differential Ca^{2+} -binding behaviors of the linker regions in PCDH15: the heterogeneity in the linkers, combined with the relatively low physiological concentration of Ca^{2+} and the dissociation constant of Ca^{2+} , might result in the overall softening. As was observed at a saturating Ca^{2+} concentration, the size of discrete unfolding events was relatively small, with peaks at 4.6 ± 0.1 nm and 8.4 ± 0.4 nm (means \pm SEMs; $N = 4$ datasets; $n = 187$ events; Figure 23D).

Again, the total unfolding per cycle was small, generally below 20 nm, a behavior that might also reflect extension of the linker regions (Figure 23E). The total unfolding per cycle grouped into two classes, one with an average of 4.5 ± 0.1 nm and the other with an average of 11.5 ± 0.1 nm (means \pm SEMs; $N = 4$ datasets; $n = 172$ events). Those values are similar in magnitude to the total unfolding per cycle that we observed at a saturating level of Ca^{2+} . The values are also similar to the magnitudes of the discrete unfolding events, which suggests that most unfolding events occurred in a single-step process at this level of Ca^{2+} . Again, it is not possible to discern the origin of these classes of unfolding events due to the repetitive nature of the structure of PCDH15. However, we conjecture due to the magnitude of the conformational change that these two classes arise

from the inter-domain linker regions of PCDH15 that, when unfolded, would give rise to 16 nm of additional length, assuming a length of 0.40 nm per amino acid⁷⁸. These results suggest that, at saturating and physiological Ca^{2+} conditions, unfolding of the linkers confers flexibility to PCDH15 and thereby allows modulation of its stiffness. The individual unfolding events were again distributed across a range of forces, with the 4.6 nm class of unfolding events occurring predominantly below 40 pN whereas the 8.4 nm class showed no clear pattern.

3.4.4 PCDH15 in the absence of Ca^{2+}

Parts of this section have been adapted from Villasante *et al.* (2023), which I wrote in association with the listed co-authors⁵⁴.

In the absence of Ca^{2+} , PCDH15 underwent many types of unfolding events that can be seen both in individual cycles (Figure 21I-K) and in numerous highly occupied branches on the heatmap (Figure 21L). There were far more unfolding events than were observed at higher Ca^{2+} concentrations, and among the discrete unfolding events there were three classes: 4.9 ± 0.1 nm, 16.1 ± 0.2 nm, and 26.5 ± 0.4 nm (means \pm SEMs; $N = 6$ datasets; $n = 868$ events; Figure 23G). The largest class of discrete unfolding in this level of Ca^{2+} , at 26.5 nm, is larger than the amount of unfolding expected from the linker regions alone, 16 nm, which suggests that another type of unfolding event is occurring. Upon the unfolding of an EC domain or the PICA domain, we would expect to see an extension of 33 nm to 45 nm, depending on the particular domain³⁹ and assuming a length of 0.40 nm per amino acid⁷⁸ less 4.5 nm to account for the loss of the folded cadherin domain²⁸. This

means that the 26.5 nm class of unfolding events does not correspond to unfolding of an entire domain. It is possible that it represents part of a domain unfolding, so next I looked at the sum of unfolding per cycle to see whether there was a peak at the expected length of an EC domain.

The sum of unfolding events per cycle, although peaking at 23.3 ± 0.6 nm (mean \pm SEM; $N = 6$ datasets; $n = 490$ events; Figure 23H), reached values as great as 100 nm. Because we did not observe a clear peak in the range of 33 nm to 45 nm, as would be expected for the unfolding of an entire EC domain, the unfolding of full domains was not the primary response to applied force. This result is surprising, because we had expected to see more frequent domain unfolding at this level of Ca^{2+} as was seen in PCDH15 monomers, but our results suggest that an alternative mechanism is in play. In the absence of Ca^{2+} , the three classes of discrete unfolding events occur across a range of forces with no evident patterns (Figure 23I).

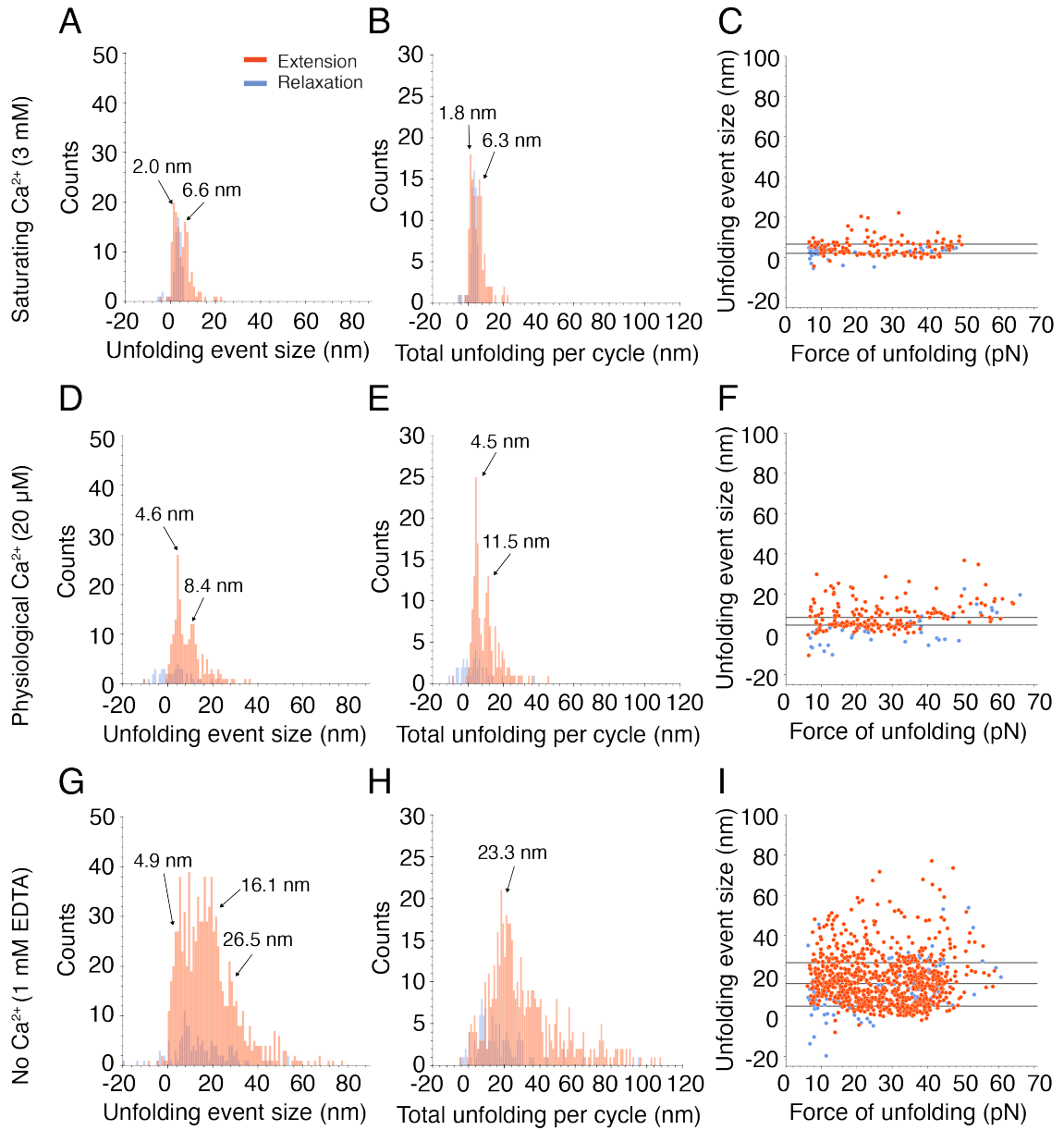


Figure 23. PCDH15 exhibited numerous unfolding behaviors across relevant Ca^{2+} concentrations.

(A) At a saturating level of Ca^{2+} , PCDH15 underwent discrete unfolding events of two predominant classes, 2.0 ± 0.1 nm and 6.6 ± 0.1 (means \pm SEMs; $N = 5$ datasets; $n = 140$ events). (B) The total unfolding per cycle at saturating Ca^{2+} is similar, with peaks at 1.8 ± 0.1 nm and 6.3 ± 0.2 nm (means \pm SEMs; $N = 5$ datasets; $n = 131$ events). (C) Many unfolding events occurred below 10 pN. The black lines indicate the location of the peaks from A. (D) At a physiological concentration of Ca^{2+} , individual unfolding events occurred in two main classes: 4.6 ± 0.1 nm and 8.4 ± 0.4 nm (means \pm SEMs; $N = 4$ datasets; $n = 187$ events). (E) The total unfolding per cycle is slightly greater, with peaks at 4.5 ± 0.1 nm and

11.5 ± 0.1 nm (means ± SEMs; $N = 4$ datasets; $n = 172$ events). (F) The 4.6 nm class of unfolding events predominantly occurred below 40 pN. The black lines indicate the location of the peaks from *D*. (G) In the absence of Ca^{2+} , three main types of discrete unfolding events occurred: 4.9 ± 0.1 nm, 16.1 ± 0.2 nm, and 26.5 ± 0.4 nm (means ± SEMs; $N = 6$ datasets; $n = 868$ events). (H) However, the total unfolding per cycle was unimodal in behavior, with a peak at 23.3 ± 0.6 nm (means ± SEMs; $N = 6$ datasets; $n = 490$ events). (I) The three major types of discrete unfolding events have a wide force distribution with no clear patterns. The black lines indicate the location of the peaks from *G*.

3.4.5 Enthalpic stiffness of PCDH15

Parts of this section have been adapted from Villasante *et al.* (2023), which I wrote in association with the listed co-authors⁵⁴.

I calculated the enthalpic stiffness of folded PCDH15 by finding the inverse spatial derivative of each cycle in the high force regime and averaging the value across all data for each Ca^{2+} condition. I chose 30 pN as the minimum cut-off for the high force regime, because after this the relationship between the force and extension became essentially linear. Because I was interested in calculating only the stiffness of folded PCDH15, I also excluded any segments that exhibited unfolding. At a physiological concentration of Ca^{2+} , 20 μM , I found that the enthalpic stiffness of PCDH15 alone, k_{PCDH15} —after accounting for the contribution of the anchors using Equation 3.2—to be 6.2 ± 0.4 $\text{mN}\cdot\text{m}^{-1}$ (mean ± SEM; $N = 4$ datasets; $n = 587$ segments).

If we assume that CDH23, which is approximately 2.3 times as long as PCDH15, has similar mechanical properties to PCDH15, its stiffness k_{CDH23} would be about 2.8 $\text{mN}\cdot\text{m}^{-1}$. The stiffness k_{TL} of the entire tip link can then be estimated by treating PCDH15 and CDH23 as springs in series:

$$\frac{1}{k_{TL}} = \frac{1}{k_{PCDH15}} + \frac{1}{k_{CDH23}} \quad (3.3)$$

Using this set of values, the enthalpic stiffness of the entire tip link in a normal animal is expected to be about 1.9 mN·m⁻¹. Measurements at 1.5 mM Ca²⁺ in the rat's cochlea have shown the stiffness of the gating spring to be between 0.5 mN·m⁻¹ and 4 mN·m⁻¹, depending on the characteristic frequency within the cochlea²², so the value I obtain for the enthalpic stiffness of PCDH15 lies within the expected stiffness range for the gating spring.

CHAPTER 4. Mechanics of a PCDH15 non-syndromic hearing loss mutation

4.1 Background

There are hundreds of mutations in the tip link that result in deafness, and these mutations are associated with either syndromic or non-syndromic deafness. PCDH15 harbors many members of these two classes of mutations, which cause Usher syndrome type 1F (USH1F) or autosomal recessive non-syndromic deafness type 23 (DFNB23). Those with USH1F develop vestibular dysfunction and retinitis pigmentosa in addition to deafness within the first decade of life⁷⁹. These conditions are presumably a result of the mutated PCDH15, which is also present in the retinal epithelium and the hair cells of the vestibular system. However, those with mutations in PCDH15 that result in DFNB23 present with only deafness, not vestibular or visual dysfunction, even though the mutated PCDH15 molecules occur in the vestibular system and the retina as well. I chose to study one such mutation to investigate whether its mechanics in comparison to the wild-type PCDH15 would give insight into this conundrum.

I investigated a point mutation of a highly conserved valine to aspartic acid in EC5, V528D (Figure 24A), which results in a pre-lingual onset of deafness without associated vestibular or visual dysfunction. The condition, which is inherited in an autosomal recessive pattern⁸⁰, was identified in a consanguineous family in Newfoundland whose members live in an isolated area with a high incidence of deafness and other heritable medical disorders. This mutation is unique because it occurs neither in one of the dimerization sites of PCDH15, nor

in an EC domain involved in the handshake interaction with CDH23, but is nevertheless deleterious enough to result in deafness. For further study, I used the murine homolog of V528D, V507D, and will refer to this mutation as V507D in the rest of the text. The V507 residue is located in the B strand of EC5 (Figure 24B). The change of a hydrophobic valine to a negatively charged aspartic acid in a β -sheet likely disrupts its structure, possibly destabilizing EC5 as a result. Studying the structural and mechanical effects of this mutation would give insight not only into the mechanism of deafness of those with this mutation, but also into what is important to the normal function of PCDH15 in the ear.

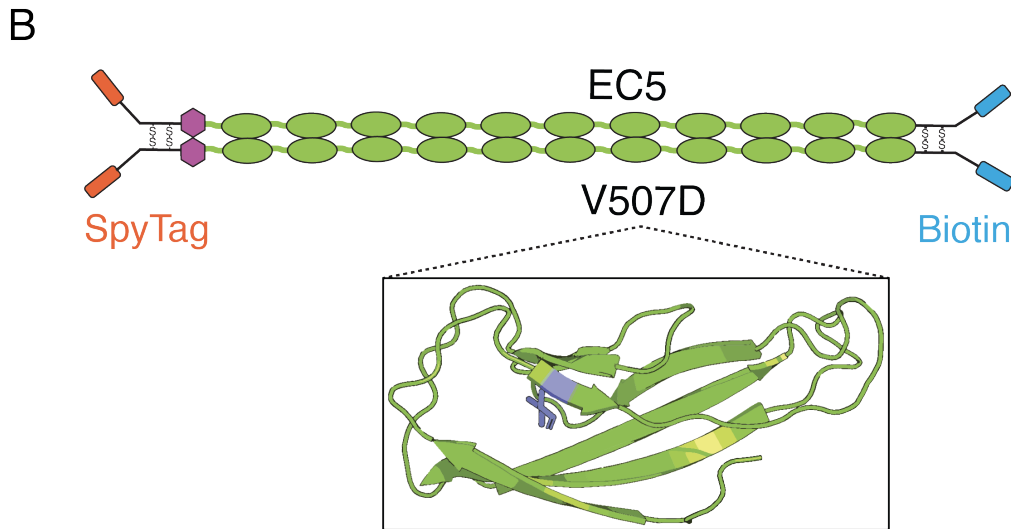
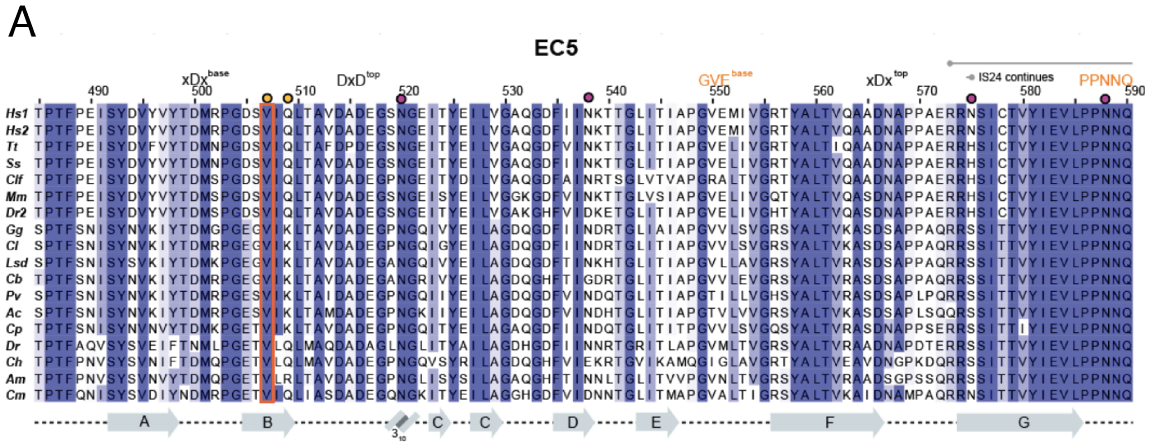


Figure 24. The V507D hearing loss mutation is at the site of a highly conserved valine in a β -sheet in EC5.

(A) Sequence alignment of EC5 for several species shows that V507 (orange box) is highly conserved. The Ca^{2+} -binding motifs are listed atop the sequence alignment, while the corresponding secondary structure elements are below. Residues in darker blue indicate more highly conserved amino acids, whereas those in white are the least conserved. Figure adapted from Choudhary *et al.* (2020). (B) The V507 residue (periwinkle) is located in the B strand β sheet of EC5. To study the mechanics of V507D, the mutation was inserted into the wild-type construct. The functional tags on either end allowed it to be studied using the optical trap set-up. PDB ID: 5W1D.

4.2 Materials and methods

The methods were identical to those for the wild-type protein, save for the plasmid design.

4.2.1 Plasmid design

The V507D mutation was introduced into the background of the PCDH15 wild-type plasmid by subcloning an insert containing the mutated residue into the wild-type vector, made with isoform 1 from *Mus musculus* (UniProt entry Q99PJ1) as the PCDH15 sequence.

4.3 Results

4.3.1 Negative-staining transmission electron microscopic studies of

PCDH15 V507D

I first examined the morphology of PCDH15 V507D by TEM to see whether it has a morphological dependence on Ca^{2+} similar to that of the wild type, and to what extent it differs from the structure of the wild type. At a saturating Ca^{2+} concentration of 3 mM, the two strands of the dimer in PCDH15 V507D already had a wide gap between them, causing them to bow outwards from each other (Figure 25A). This structure was in contrast to that of the wild type at the same level of Ca^{2+} , in which the two strands of the dimer were closely associated with each other. Because the only difference between the two proteins is the V507D point mutation, that change is presumably responsible for the drastic structural differences that I observed. Even at a saturating level of Ca^{2+} , at which PCDH15

should be the most stable, EC5 might be sufficiently disrupted by the mutation to result in increased dissociation between the two strands.

When Ca^{2+} was lowered to a physiological level of 20 μM , V507D displayed a pattern similar to that at saturating Ca^{2+} , in which the two strands of the dimer bowed outwards from each other (Figure 25B). The similarity between the appearance of the V507D molecules at saturating and physiological Ca^{2+} concentrations suggests that Ca^{2+} does not have a large stabilizing effect on the molecule.

When Ca^{2+} was removed completely, the V507D molecules appeared much more disorganized, with a larger gap between the strands than at higher Ca^{2+} levels (Figure 25C). But, unlike the wild type, in the V507D images it was difficult to see the structures clearly, suggesting that the mutant is folding inappropriately in the absence of Ca^{2+} . The structural differences between V507D and the wild type seen in TEM images suggest that there are also mechanical differences between the two, study of which might provide insight into the mechanism of deafness in those with the V507D mutation.

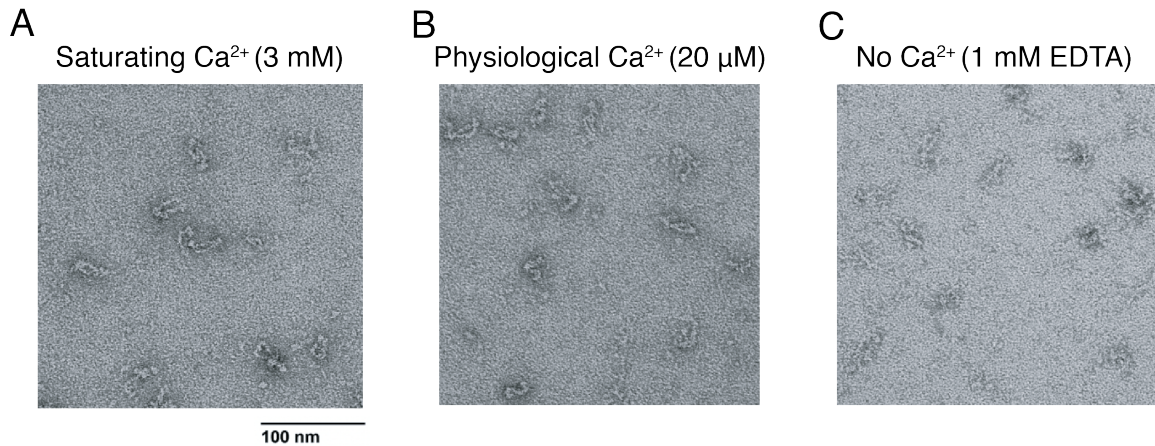


Figure 25. Transmission electron microscopy of PCDH15 V507D showed a high degree of conformational heterogeneity across three important Ca²⁺ concentrations.

(A) At a saturating concentration of Ca²⁺, there was already a large gap between the two strands of V507D that was not seen in the wild-type PCDH15. This alteration suggests that even at the most stabilizing level of Ca²⁺, there is significant perturbation of the overall structure due to the point mutation. (B) The pattern was similar at a physiological level of Ca²⁺: there was a large gap between the two strands of V507D, and the overall appearance of the molecules was more heterogeneous than at a saturating level of Ca²⁺. (C) In the absence of Ca²⁺, the molecules were much more disorganized than at the higher levels of Ca²⁺.

4.3.2 PCDH15 V507D at a saturating level of Ca²⁺

I then performed force-ramp experiments on PCDH15 V507D using the optical trap system described in Chapter 2 at three important Ca²⁺ concentrations: at a saturating (3 mM) concentration of Ca²⁺, at a physiological level of Ca²⁺ (20 μM), and in the absence of Ca²⁺. This approach allowed me to examine the Ca²⁺ dependence of PCDH15 V507D as well as compare the results to those of the wild type.

At a high Ca²⁺ concentration of 3 mM, there appeared to be two populations of V507D molecules. Some molecules appeared to behave more like the wild-type PCDH15 at the same level of Ca²⁺, with minimal unfolding observed in individual

cycles (Figure 26A-C). The population was reflected by the single bright branch on the corresponding heatmap (Figure 26D). Other molecules exhibited more unfolding during individual cycles (Figure 26E-G), which was also evidenced by the multiple bright branches on the heatmap (Figure 26H). We decided to include both populations in further analysis, because the tethering statistics for both populations gave us confidence they corresponded to single molecules rather than multiple tethers (see Section 2.10.7), and we observed both populations often enough to deem them significant.

We observed many more discrete unfolding events from V507D than from wild-type PCDH15 at the same level of Ca^{2+} , for which we observed only small unfolding events largely below 10 nm in magnitude. For V507D, we observed classes of unfolding events at 11.0 ± 0.1 nm, 22.4 ± 0.1 nm, 28.7 ± 0.02 nm, 32.7 ± 0.04 nm, 40.5 ± 0.1 nm, 49.6 ± 0.2 nm, and 70.5 ± 0.1 nm (means \pm SEMs; $N = 24$ datasets; $n = 1889$ events; Figure 27A). Because these unfolding events occurred at a Ca^{2+} level likely to saturate Ca^{2+} binding sites in the inter-domain linker regions, and because the only difference between V507D and the wild type is the point mutation, the unfolding probably stemmed from instability in EC5, where the mutated residue is located. The classes at 32.7 nm and 40.5 nm fall within the range expected for the unfolding of a full-length EC domain or the PICA domain, which would be between 33 nm and 45 nm. Those classes of unfolding could correspond to the unfolding of EC5, which would theoretically result in a 35.1 nm unfolding event, assuming a length of 0.40 nm per amino acid⁷⁸ less 4.5 nm to

account for the loss of the folded EC domain²⁸. The 11.0 nm class of unfolding could correspond to unfolding of the inter-domain linker regions, which would give rise to a 16 nm end-to-end distance change in total. The 22.4 nm, 28.7 nm, and 49.5 nm classes do not clearly correspond to unfolding of the linkers or an entire EC domain. It may be that EC5 unfolds in a two-step process due to the location of the mutation, or that portions of the domains adjacent to EC5 partially unfold as a result of EC5's instability and give rise to unfolding events of intermediate magnitudes. Finally, the 70.5 nm class of unfolding events may stem from the unfolding of two EC domains, which would give rise to an end-to-end distance increase between 66 and 90 nm.

The total unfolding per cycle peaked at 8.8 ± 0.1 nm, 50.0 ± 0.2 nm, and 66.3 ± 0.2 nm (means \pm SEMs; $N = 24$ datasets; $n = 1144$ events; Figure 27B). The 50.0 nm class of unfolding events is above the range of what would correspond to unfolding of an entire EC domain or the PICA domain, 33 nm to 45 nm, but less than the amount expected for the unfolding of two domains. This suggests that some intermediate unfolding event is occurring to give rise to this class. The 66.3 nm class of events may reflect the unfolding of two domains.

Many larger individual unfolding events happened at smaller forces, while smaller discrete unfolding events had a wider range of unfolding forces (Figure 27C). This pattern was an unexpected finding, and contrary to that of the wild type, which displayed a more uniform distribution of unfolding forces.

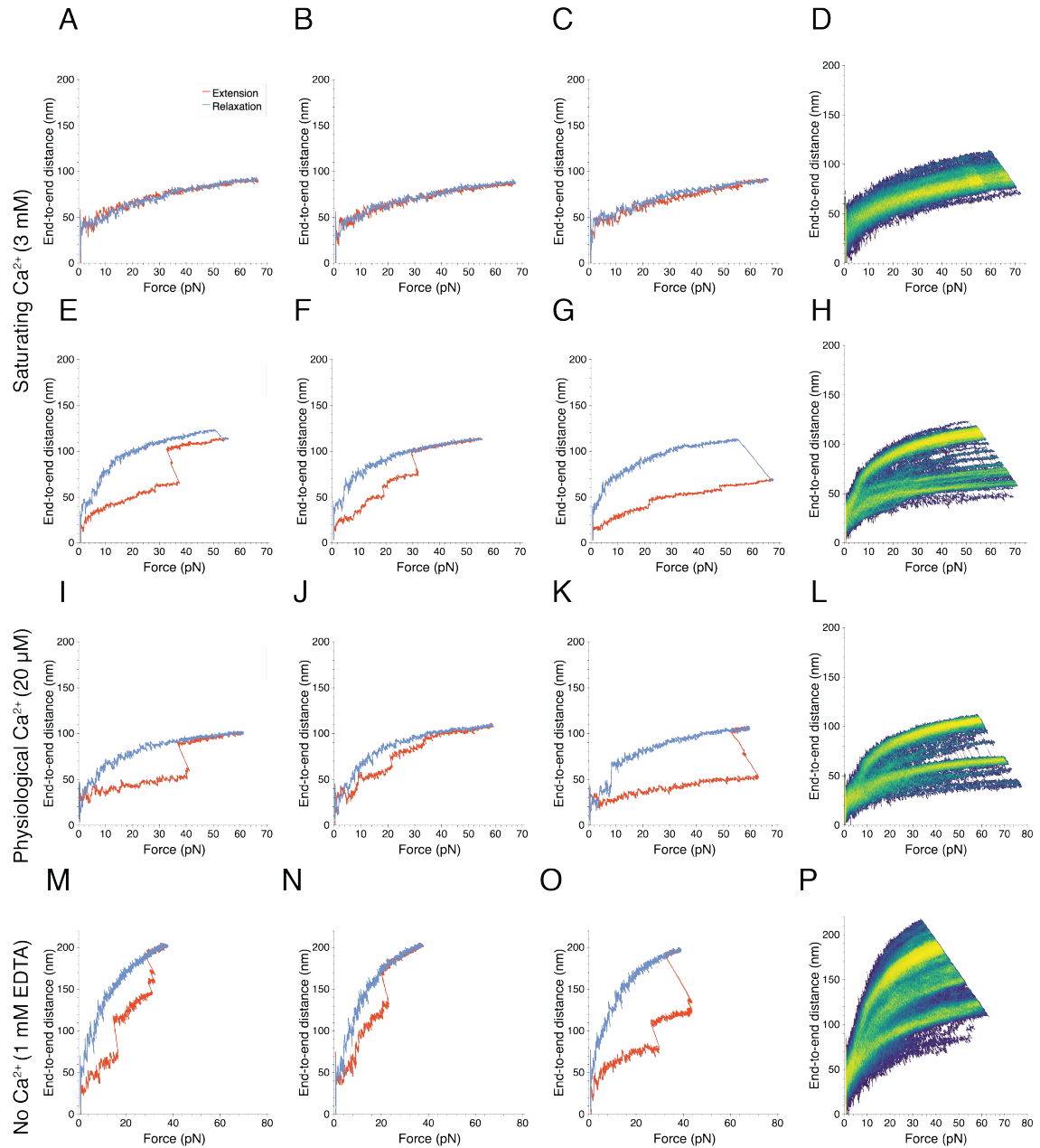


Figure 26. PCDH15 V507D exhibited rich unfolding events across relevant Ca^{2+} concentrations.

At a saturating level of Ca^{2+} , PCDH15 V507D molecules grouped into two different types. (A-C) In some datasets, V507D rarely unfolded, as evidenced by successive cycles as well as (D) the single bright branch on an illustrative heatmap. (E-F) In other datasets at a saturating level of Ca^{2+} , PCDH15 V507D unfolded frequently on the individual cycle level. (H) The bright branches on the illustrative heatmap reflect the frequent unfolding seen in individual cycles. (I-K) At a physiological concentration of Ca^{2+} , frequent unfolding is seen in subsequent individual cycles. (L) The unfolding seen in the individual cycles is reflected in the bright branches

on the illustrative heatmap. (M-O) Subsequent force-ramp cycles show that in the absence of Ca^{2+} , PCDH15 V507D extends easily, even in the absence of large unfolding events. (P) The bright branches on the illustrative heatmap reflect the unfolding behavior seen on the individual cycle level. The upper limits of the end-to-end distance at this level of Ca^{2+} exceed those seen at higher concentrations of Ca^{2+} , as well as those seen in the wild type at the same concentration of Ca^{2+} .

4.3.3 PCDH15 V507D at a physiological concentration of Ca^{2+}

When the Ca^{2+} concentration was decreased to a physiological level of 20 μM , V507D underwent unfolding events of varying magnitudes, as can be seen in individual cycles (Figure 26I-K) as well as on the illustrative heat map, which shows multiple bright branches (Figure 26L). The individual unfolding events at this level of Ca^{2+} fell into three predominant groups: 12.7 ± 0.2 nm, 27.0 ± 0.1 nm, and 39.0 ± 0.2 nm (means \pm SEMs; $N = 16$ datasets; $n = 1536$ events; Figure 27D). The class at 39.0 nm could correspond to the unfolding of an entire EC domain or the PICA domain, which would be in the range of approximately 33 nm to 45 nm. It is unclear what event gives rise to the smaller classes of unfolding events, though unfolding of the linker regions, which would result in a total 16 nm increase in end-to-end distance, could be contributing to these. In general, this behavior contrasted with that of the wild type at the same Ca^{2+} concentration, for which very few, small unfolding events were seen.

The total unfolding within each cycle was very similar to the discrete unfolding events, again separating into three classes: 14.2 ± 0.2 nm, 27.3 ± 0.1 , 39.4 ± 0.3 nm (means \pm SEMs; $N = 16$ datasets; $n = 1081$ events; Figure 27E). The similarity between the classes found from discrete unfolding events and from the total unfolding per cycle suggest that, at this level of Ca^{2+} , most events

occurred at once rather than in a multi-step process. The classes of unfolding at this level of Ca^{2+} did not reach such high magnitudes as at saturating Ca^{2+} , even though we predicted that V507D would be more unstable and exhibit more unfolding at this level of Ca^{2+} . This behavior suggests that V507D is partially unfolded at baseline due to the decreased stabilizing effect of Ca^{2+} , and hence unfolds less when force is applied. As at saturating Ca^{2+} , many larger individual unfolding events tended to occur at lower unfolding forces (Figure 27F).

4.3.4 PCDH15 V507D in the absence of Ca^{2+}

Like the wild-type dimer at the same level of Ca^{2+} , V507D underwent numerous unfolding events in the absence of Ca^{2+} , as evidenced by the multiple bright branches on the illustrative heat map (Figure 26P). However, the bright branch closest to the origin—which reflects the extension of the protein in the absence of any unfolding events—extended to approximately 100 nm at the highest applied forces, whereas for the wild-type protein this branch extended only to about 50 nm. Additionally, the largest end-to-end distances achieved for V507D extended beyond 200 nm, a distance greater than those observed for the wild type. In individual cycles, in many cases we did not observe drastic unfolding events (Figure 26M-O). Rather, the molecule appeared quite extended at baseline and lengthened easily with the application of force. This suggests that the protein is already unfolded, or misfolded, at this concentration of Ca^{2+} even in the absence of force.

The individual unfolding events peaked at 23.2 ± 0.5 nm (mean \pm SEM; $N = 4$ datasets; $n = 694$ events; Figure 27G), and the total unfolding per cycle peaked at 49.3 ± 1.4 nm (mean \pm SEM; $N = 4$ datasets; $n = 362$ events; Figure 27H), although sometimes as much as close to 150 nm unfolded in a single cycle. The total unfolding per cycle suggests that at least one full domain unfolded in the course of a force ramp. At this level of Ca^{2+} there was no clear relationship between the size of unfolding events and the force at which they occurred (Figure 27I). Returning to what we observed from the data at both the individual cycle and heat map levels, it is apparent that the end-to-end distance range of the V507D protein exceeded that at other levels of Ca^{2+} (Figure 26). This result suggests that, in the absence of Ca^{2+} , V507D does not fold properly even at low resting forces.

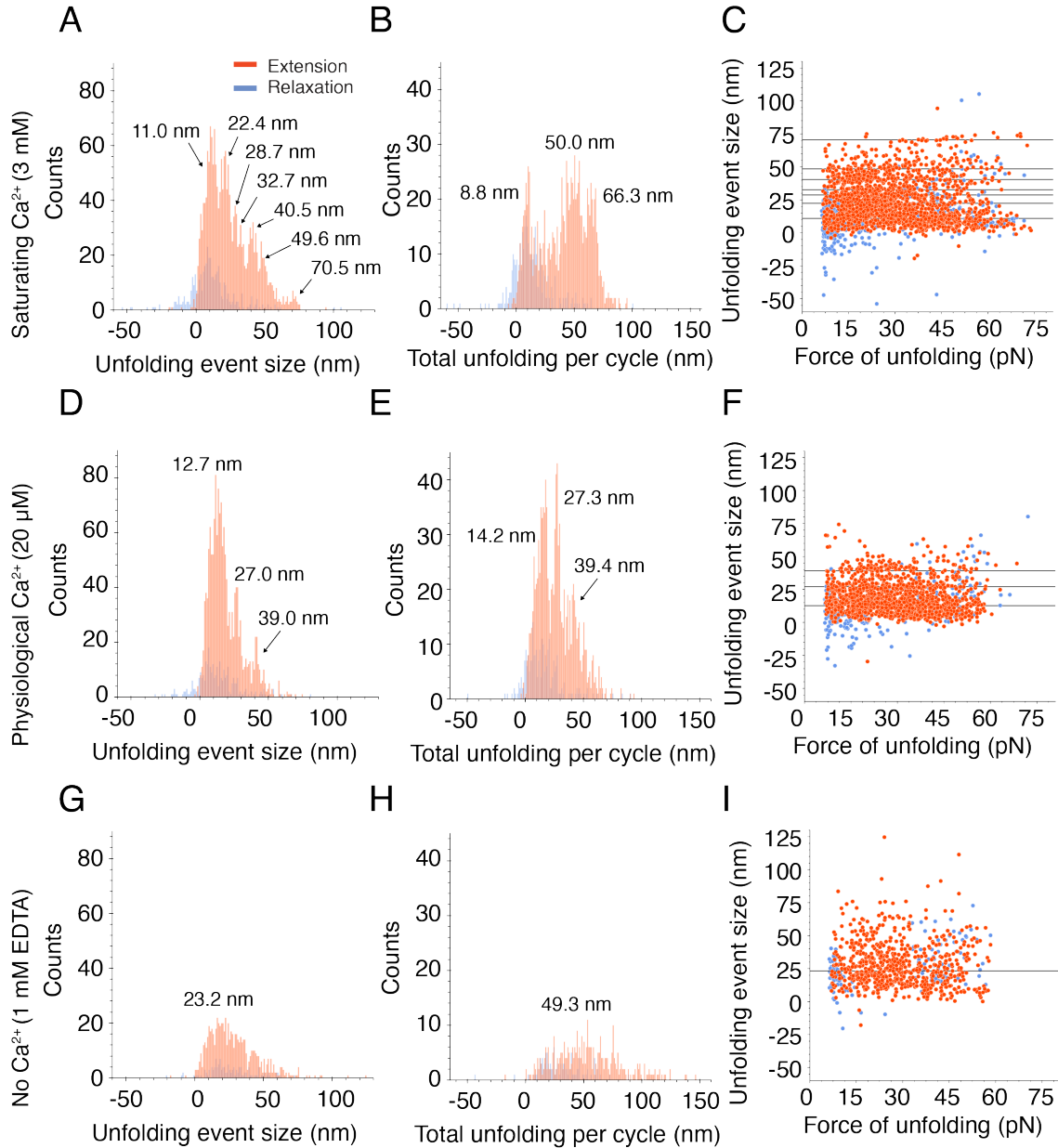


Figure 27. PCDH15 V507D displayed a variety of unfolding events across important concentrations of Ca^{2+} .

(A) At a saturating level of Ca^{2+} , PCDH15 V507D has peaks of discrete unfolding events at 11.0 ± 0.1 nm, 22.4 ± 0.1 nm, 28.7 ± 0.02 nm, 32.7 ± 0.04 nm, 40.5 ± 0.1 nm, 49.6 ± 0.2 nm, and 70.5 ± 0.1 nm (means \pm SEMs; $N = 24$ datasets; $n = 1889$ events). (B) The sum of total unfolding per cycle was predominantly around 8.8 ± 0.1 nm, 50.0 ± 0.2 nm, and 66.3 ± 0.2 nm (means \pm SEMs; $N = 24$ datasets; $n = 1144$ events). (C) The black lines indicate the peaks from A. As the size of the individual unfolding event gets larger, the force of unfolding tends to be lower, with many events occurring around 30 pN. (D) In a physiological concentration of Ca^{2+} , PCDH15 V507D grouped into individual unfolding events at 12.7 ± 0.2 nm, $27.0 \pm$

0.1 nm, and 39.0 ± 0.2 nm (means \pm SEMs; $N = 16$ datasets; $n = 1536$ events). (E) The magnitude of total unfolding per cycle was similar to that of the individual unfolding events, with peaks at 14.2 ± 0.2 nm, 27.3 ± 0.1 , 39.4 ± 0.3 nm (means \pm SEMs; $N = 16$ datasets; $n = 1081$ events). (F) The black lines indicate the peaks from *D*. As at a saturating level of Ca^{2+} , the larger unfolding events were associated with smaller forces of unfolding. (G) When Ca^{2+} was removed completely, the rich unfolding behavior seen at higher levels of Ca^{2+} disappeared, and instead only one peak of discrete unfolding was seen, at 23.2 ± 0.5 nm (mean \pm SEM; $N = 4$ datasets; $n = 694$ events). (H) The sum of unfolding per cycle was similarly unimodal, with one peak at 49.3 ± 1.4 nm (mean \pm SEM; $N = 4$ datasets; $n = 362$ events). (I) The black line indicates the peak from *G*. There was no clear relationship between the size of individual unfolding events and forces at which they occurred.

4.3.5 Enthalpic stiffness of PCDH15 V507D

As with wild-type PCDH15, I calculated the enthalpic stiffness of folded PCDH15 V507D by finding the inverse spatial derivative of each cycle in the high force regime and averaging the value across all data for each Ca^{2+} condition. At a physiological level of Ca^{2+} , I found the enthalpic stiffness of V507D alone to be 4.3 ± 0.2 mN \cdot m $^{-1}$ (mean \pm SEM; $N = 16$ datasets; $n = 1231$ segments). This stiffness value is significantly ($p=0.0001$) different from that of the wild-type PCDH15 at physiological Ca^{2+} , 6.2 ± 0.4 mN \cdot m $^{-1}$ (mean \pm SEM; $N = 4$ datasets; $n = 587$ segments). However, when this value is put into Equation 3.3 to determine the predicted stiffness of the entire tip link, I get a value of 1.7 mN \cdot m $^{-1}$, which remains within the range of experimentally determined gating spring stiffness values²².

That the calculated enthalpic stiffness of PCDH15 V507D still accords with the range of experimentally determined gating spring stiffness values raises the question: what is the mechanism of deafness in those with the V507D mutation if

the stiffness values for PCDH15, though significantly different from the wild type at the same level of Ca^{2+} , would still result in an appropriate overall gating-spring stiffness?

My hypothesis is that the answer lies in the differences between the unfolding behavior of the two proteins. At physiological Ca^{2+} , the wild-type PCDH15 unfolded infrequently and the magnitudes of its unfolding events were relatively small, predominantly below 20 nm. However, PCDH15 V507D unfolded much more frequently at the same level of Ca^{2+} , and the magnitude of the unfolding events that occurred reached as much as 50 nm. The difference in unfolding behavior implies that even though the stiffness of the folded V507D protein at physiological Ca^{2+} situated the tip link's stiffness in the range for the gating spring, the link spends less time in the fully folded state compared to the wild-type PCDH15. The functional implication is that the stiffness of V507D is less than the calculated value and a softer overall tip link is unable to convey appropriate tension to the MET channels.

CHAPTER 5. Investigations into the mechanism of tension regulation in PCDH15

5.1 Background

In both the wild-type and V507D PCDH15 results, there are numerous classes of unfolding events of various magnitudes. Some of these events fall within the range expected for unfolding of a full EC domain, whereas other events are what would be expected if the inter-domain linker regions were to come undone. There are yet additional events that fall within neither of those categories. What is the structural origin of these unfolding events? Are there certain regions of PCDH15 that serve as a release when force is applied, unfolding before other regions? What happens if these regions cannot unfold—how does PCDH15 respond to force? The answers to these questions may give insight into the mechanism of tension regulation in wild type PCDH15, as well as how this mechanism may be perturbed in the case of the V507D mutation.

Because PCDH15 consists of repeating structural motifs of similar sizes, it is difficult to know with certainty the specific structural origin of any particular unfolding event. However, there is variability in the Ca²⁺-binding capabilities of the inter-domain linker regions, with some linkers binding no Ca²⁺ at all, whereas others bind only one or two Ca²⁺ ions instead of three (Figure 28)⁴¹.

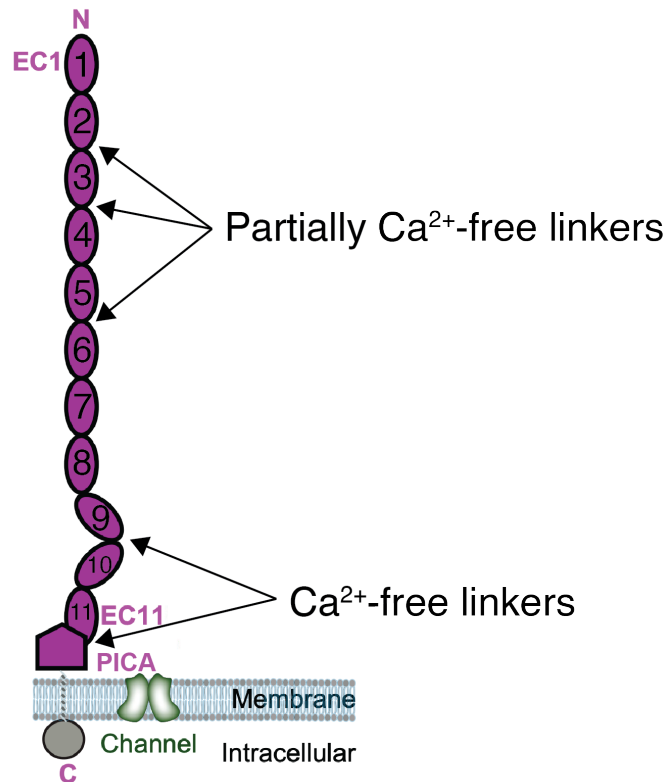


Figure 28. The inter-domain linker regions have differential Ca²⁺-binding properties.

Not all the linker regions within PCDH15 bind three ions of Ca²⁺. Some linkers bind fewer: the EC2-3 and EC3-4 linker regions each bind two ions of Ca²⁺ whereas EC5-6 binds only one. The EC9-10 and EC11-PICA domain linkers bind no Ca²⁺ ions. Adapted from Choudhary *et al.* (2020).

Based on this arrangement, it is plausible that some domains are more prone to unfolding than others depending on the amount of Ca²⁺ that can bind at neighboring linker regions. Perhaps the EC domains with minimal Ca²⁺ binding to flanking linker regions unfold more readily when force is applied, acting as a release for the system.

5.2 Materials and methods

Save for the plasmid design, the materials and methods were identical to those described in Chapter 3.

5.2.1 Plasmid design of monomeric PCDH15 with disulfide bonds in each EC domain

The plasmid encoding the monomeric murine PCDH15 with internal cysteines in each domain was constructed using Gibson assembly, yielding **signal peptide-QYDDDWQYED-AviTag-GSGSGS-PCDH15 (EC1-11; internal cysteines)-GSGSGS-SpyTag-8xHis**, in which the sequence QYDDDWQYED represents the first ten amino-acid residues of PCDH15. The native signaling peptide and the first ten residues ensured proper cellular trafficking of PCDH15 to the membrane for export. The AviTag had the sequence **GLNDIFEAQKIEWHE**. The SpyTag⁷⁵ had sequence **AHIVMVDAYKPTK**. The following residues were changed to cysteines: V23 and I114 (EC1), A133C and V232 (EC2), A263 and I362 (EC3), G381 and I476 (EC4), V495 and I582 (EC5), L602 and I684 (EC6), L704 and V788 (EC7), V805 and V893 (EC8), G912 and I1003 (EC9), V1024 and I1113C (EC10), and G1130 and V1219 (EC11). The residues were chosen such that one residue would be in the entering A' strand of the EC domain while its partner would be in the leaving G strand.

5.2.2 Plasmid design of shortened monomeric PCDH15

The shortened plasmid construct in Figure 31C was subcloned into the vector backbone with GenScript plasmid construction services (Piscataway, NJ, USA).

The final sequence was **signal peptide-QYDDDWQYED-AviTag- GSGSGS-EC4 (G381C, I476C)-EC5 (V507D)-EC6 (L602C, I684C)-GSGSGS-SpyTag-8xHis.**

5.3 A monomeric PCDH15 construct to probe the role of EC domain unfolding

I had initially proposed to make a construct in which each EC domain would be prevented from unfolding, with the goal of dissecting the contribution of the EC domain unfolding and linker region unfolding to the response of PCDH15 to force. I could then compare the data to those from the wild-type monomer. I hoped to be able to selectively prevent certain EC domains from unfolding to understand the role of specific EC domains in tension regulation. To accomplish this, I sought to use a construct in which a disulfide bond was engineered between the A' and G strands within each EC domain in monomeric PCDH15 (Figure 29). This would allow me to compare the results to those of the wild type monomeric PCDH15.

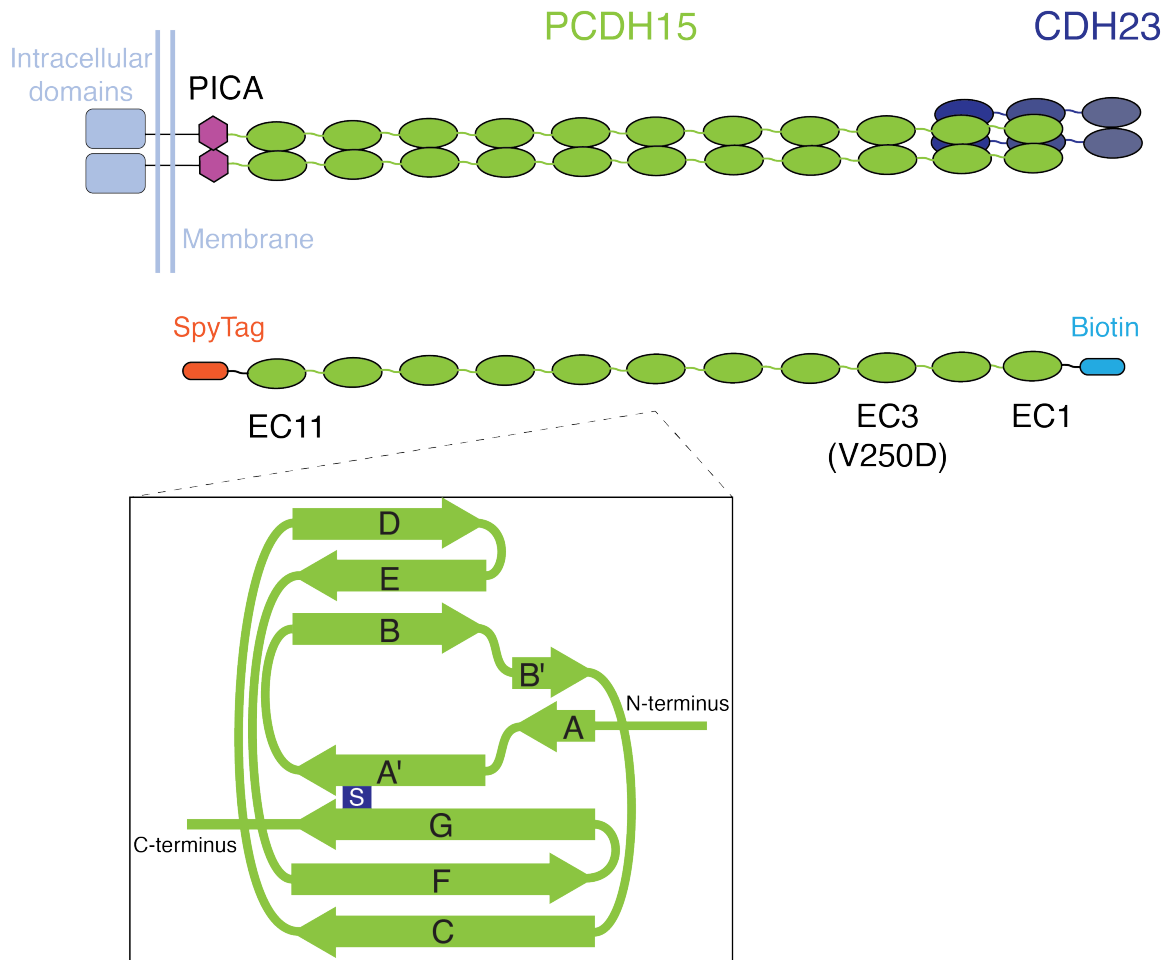


Figure 29. Creation of a monomeric PCDH15 construct with internal disulfide bonds in each EC domain.

In order to study the contribution of domain unfolding to the response of PCDH15 to force, we created a construct in which each EC domain had an internal disulfide bond to prevent unfolding. The disulfide bond between the entering A' strand and leaving G strand within each domain was meant to prevent unfolding when force is applied to the termini of the protein. This modification was done in the background of the monomeric PCDH15 construct⁶⁵.

However, this approach was marred by problems, foremost that the construct appeared to coil upon itself when viewed by TEM (Figure 30A), and many individual protein molecules even appeared to stack upon each other (Figure 30B). Rotating and superimposing the same image⁸¹ of one such coil yielded a seven-segmented ring (Figure 30C), with each segment measuring approximately the

length expected for a folded EC domain. This suggests that the construct coiled upon itself, which might be due to inappropriate inter-domain interactions of the added cysteines.

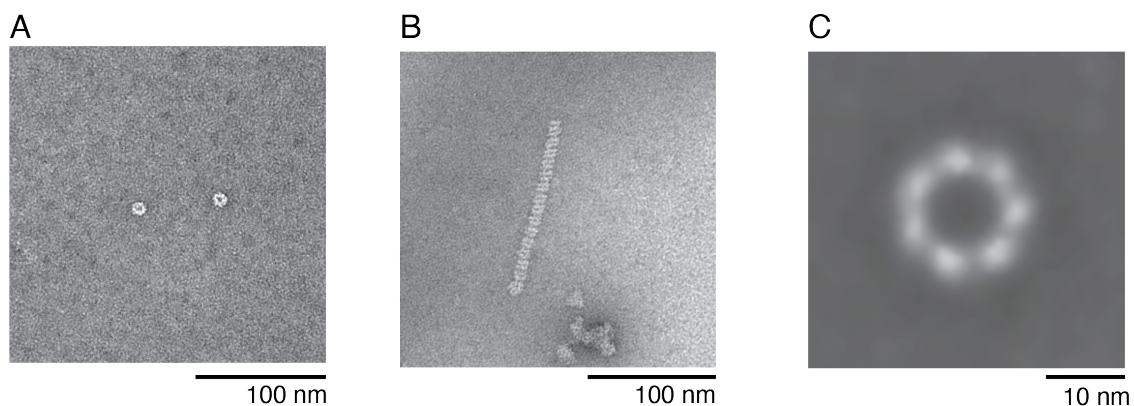


Figure 30. TEM showed that the monomeric PCDH15 construct with internal disulfide bonds behaved in unexpected ways.

(A) We often observed coiled forms of the protein. (B) These units appeared to stack upon themselves to form longer conglomerates when viewed from the side. (C) A sevenfold rotation and superposition of the image of one ring in order to enhance the contrast^{B1} yielded this image. The length of each individual segment is between about 3.4 nm and 4.3 nm. Image courtesy of A.J. Hudspeth.

5.4 Creation of a shortened PCDH15 construct to explore the role of EC domain unfolding

To counteract this problem, I proposed to make a shortened version of this construct in the hope of avoiding self-circularization in solution. I planned to make three constructs, each comprising only three EC domains: (1) A construct with a disulfide bond between the A' and G strands in each domain (Figure 31A), (2) a construct with a disulfide bond in the first and third EC domains but none in the middle EC domain (Figure 31B), and (3) a construct with a disulfide bond in the first and third EC domains but the V507D mutation in the middle EC domain (Figure 31C). The purpose of having two disulfide-bonded EC domains around the

middle domain is to ensure that the flanking Ca^{2+} -binding sites in the linker regions remain intact, for these stabilize the EC domains to which they are adjacent. Conducting force-ramp experiments on these three constructs and comparing the results should allow me to delineate how PCDCH15 unfolds in normal and pathological hearing, for I would hope to see how individual cadherin domains unfold.

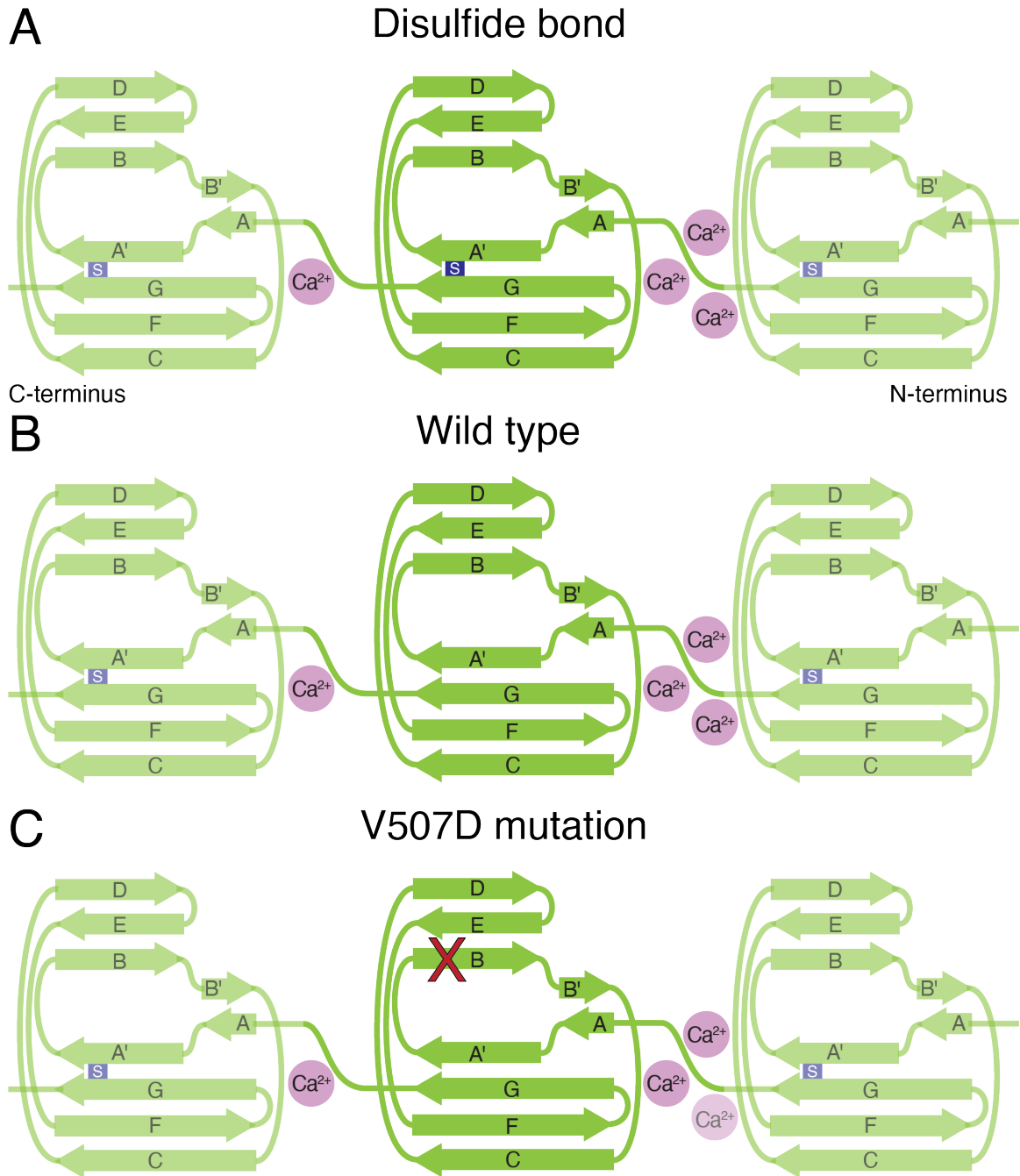


Figure 31. Proposed shortened constructs to avoid self-circularization.

In all constructs, each domain flanking the middle one has a disulfide bond. The EC4-5 linker binds two Ca^{2+} whereas the EC5-6 linker binds only one⁴¹. In (A), the central domain also has an internal disulfide bond. In (B), the middle domain is wild type—it has no disulfide bond. Finally, in (C) the central domain has the V507D mutation discussed in Chapter 4.

I started with the third construct, with the V507D mutation in the central EC domain. This construct would allow me to observe the isolated unfolding behavior of EC5 with the V507D mutation, which would allow for correlation to the result that I obtained in Chapter 4 on PCDH15 V507D across relevant Ca^{2+} concentrations. However, when the construct was expressed and purified, it resulted in a mixture of differently-sized protein products, none clearly corresponding to the expected size of the construct. Although I have not had the time to pursue this, further analysis would offer an intriguing avenue of study in the future. Deconstructing the role of EC domain unfolding in the response of PCDH15 to force would offer insight into how PCDH15 functions in both physiological and aberrant contexts.

CHAPTER 6. Discussion of results

The findings in this work indicate that PCDH15, in the dimeric form in which it exists within the cochlea, has the appropriate mechanical properties to serve as a significant portion of the gating spring. Furthermore, the results show that, at the physiological Ca^{2+} concentration and over the relevant force range, unfolding of entire EC domains is not the primary response of PCDH15 to force. Instead, the response likely comprises a series of smaller unfolding events that stem from the unfolding of the inter-domain linkers and possibly parts of EC domains. Meanwhile, in the same physiological Ca^{2+} concentration and force range, PCDH15 V507D undergoes large unfolding events, including unfolding that could correspond to entire EC domains.

6.1 Comparing the behavior of wild-type and V507D PCDH15

Comparing the behaviors of wild-type and V507D PCDH15 can offer insight into both the physiological functioning of PCDH15 as well as the mechanism of deafness in those with the V507D mutation. I will now highlight the differences in how the two proteins behave across the three relevant Ca^{2+} concentrations discussed in Chapters 3 and 4, and what might underlie these differences.

6.1.1 Saturating Ca^{2+}

At a saturating level of Ca^{2+} meant to fill all the available binding sites, PCDH15 should be its most stable. On TEM imaging, the wild-type PCDH15 molecules were fairly linear, with a small gap between the two strands of the dimer likely owing to the location of the dimerization sites within the molecule (Figure 32A). At the same

level of Ca^{2+} , PCDH15 V507D showed increased dissociation between the two strands of the dimer (Figure 32B). Because the two proteins differ by only a single amino acid—the V507D substitution—the structural differences were presumably a result of the mutation. This suggests that the structure of V507D is already perturbed in the absence of force: even at the most stabilizing level of Ca^{2+} , EC5 may be unfolded or misfolded, which results in increased dissociation between the two strands.

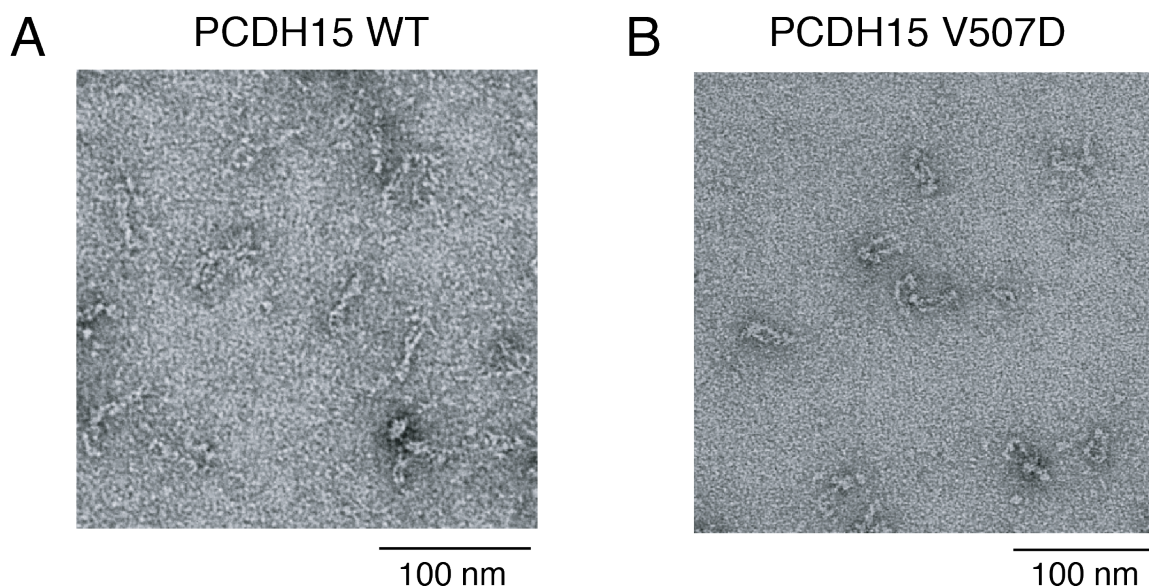


Figure 32. Comparison of wild-type and V507D PCDH15 at a saturating level of Ca^{2+} .

(A) At a saturating level (3 mM) of Ca^{2+} , the wild-type PCDH15 was predominantly linear, with only a small gap between the two strands of the dimer (extracted from Figure 20). (B) At the same concentration of Ca^{2+} , there was a larger gap between the two strands of the V507D dimer, likely a result of improper EC5 folding (extracted from Figure 25).

In wild-type PCDH15, the stabilizing effect of Ca^{2+} meant that there was very little unfolding as seen at the level of individual cycles (Figure 33A-C), reflected by the one bright branch on the illustrative heat map (Figure 33D). In

comparison, V507D molecules separated into two different classes at this level of Ca^{2+} : one that behaved more like the wild-type protein (Figure 33E-H) in that it unfolded infrequently—though it was more extensible than the wild type over the same force range—and one that unfolded frequently (Figure 33I-L). It may be that some molecules of V507D were folded properly, while other molecules were misfolded, resulting in the two classes of molecules we observed. That we did not observe such distinct groups of conformations in V507D at other levels of Ca^{2+} suggests that Ca^{2+} does stabilize V507D in some molecules but not others. The variability in the stabilizing effect of Ca^{2+} in turn suggests that in a population of tip links, some V507D molecules would be folded properly, while others would not.

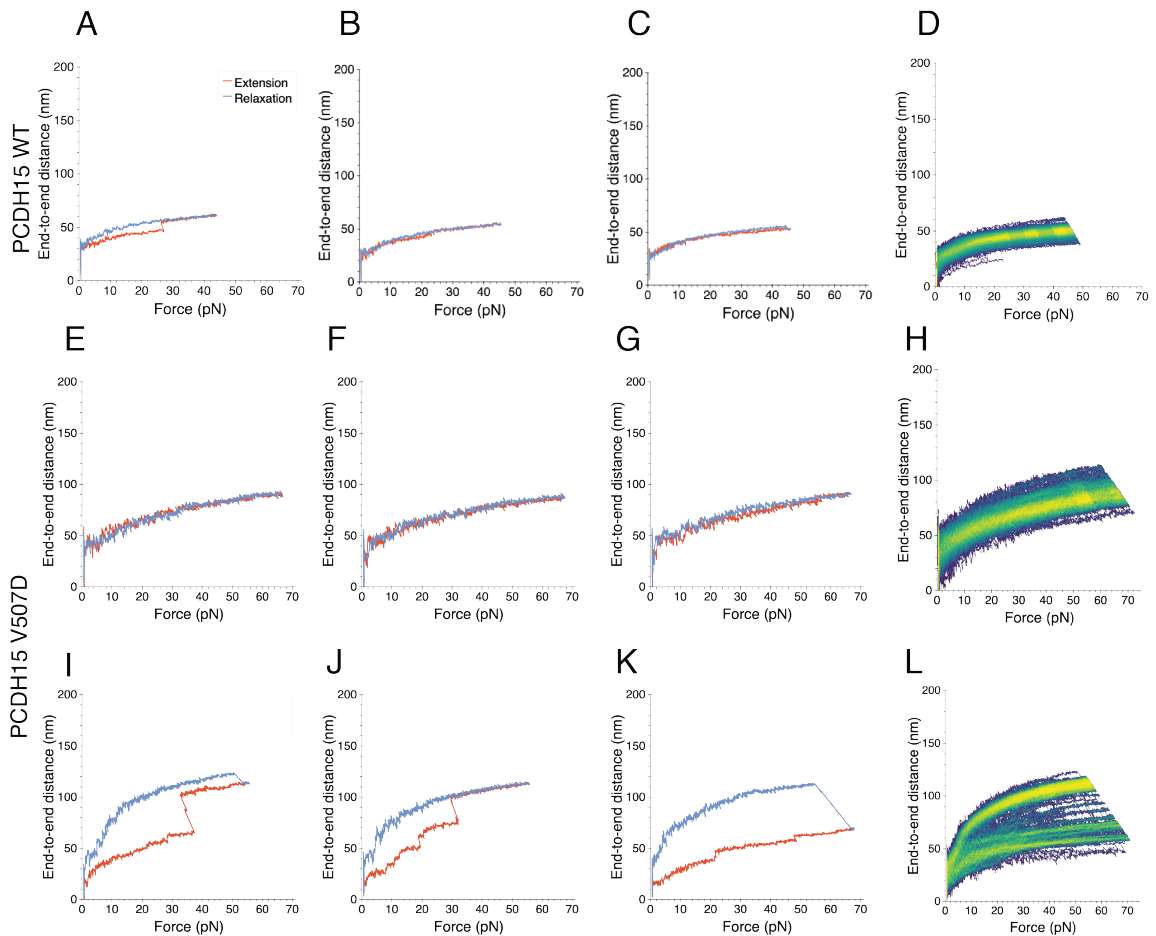


Figure 33. PCDH15 V507D at a saturating level of Ca^{2+} was more extensible and unfolded more frequently than the wild type.

(A-C) Successive cycles of the wild-type PCDH15 in 3 mM Ca^{2+} displayed infrequent unfolding. (D) The lack of unfolding and relative stiffness is exemplified in the representative heat map by the one bright branch of highly occupied state space (panels A-D extracted from Figure 21). (E-G) Subsequent cycles of one population of PCDH15 V507D molecules showed little unfolding, but the molecule was overall more extensible than the wild type at 3 mM Ca^{2+} . (H) The infrequent unfolding and the more relative extensibility are evidenced in the heat map. (I-K) Successive cycles of the other population of V507D at this concentration of Ca^{2+} exhibited frequent and large unfolding events. (L) The propensity of this population to unfolding is reflected in the numerous bright branches in the illustrative heat map (panels E-L extracted from Figure 26).

In the case of the wild type, only relatively small unfolding events occurred—in terms of the discrete events and of the total unfolding in a given cycle (Figure

34A, B). Although it is not possible to say with certainty what structural changes gave rise to those events, both values fit within the range of unfolding expected if the inter-domain linker regions were to come undone, which would result in 16 nm total of additional length. Because the linker regions lack secondary structure, it is plausible to expect that they will be the first to come undone when force is applied.

In contrast to this, at the same level of Ca^{2+} the two combined classes of V507D had many more types of unfolding events, most above the range expected for the unfolding of all of the linker regions. (Figure 34D, E). Three of the individual unfolding classes corresponded to magnitudes that might have stemmed from unfolding of one or two EC domains. Because of the location of the V507D mutation in EC5, it is reasonable to assume that in the mutant, EC5 is the most vulnerable portion of PCDH15 to unfolding, and that it gave rise to the unfolding we observed at this level of Ca^{2+} . The frequent unfolding and larger magnitude of unfolding events seen in V507D compared to the wild-type PCDH15 suggest that EC5 has lost its tension-bearing ability even at a saturating level of Ca^{2+} .

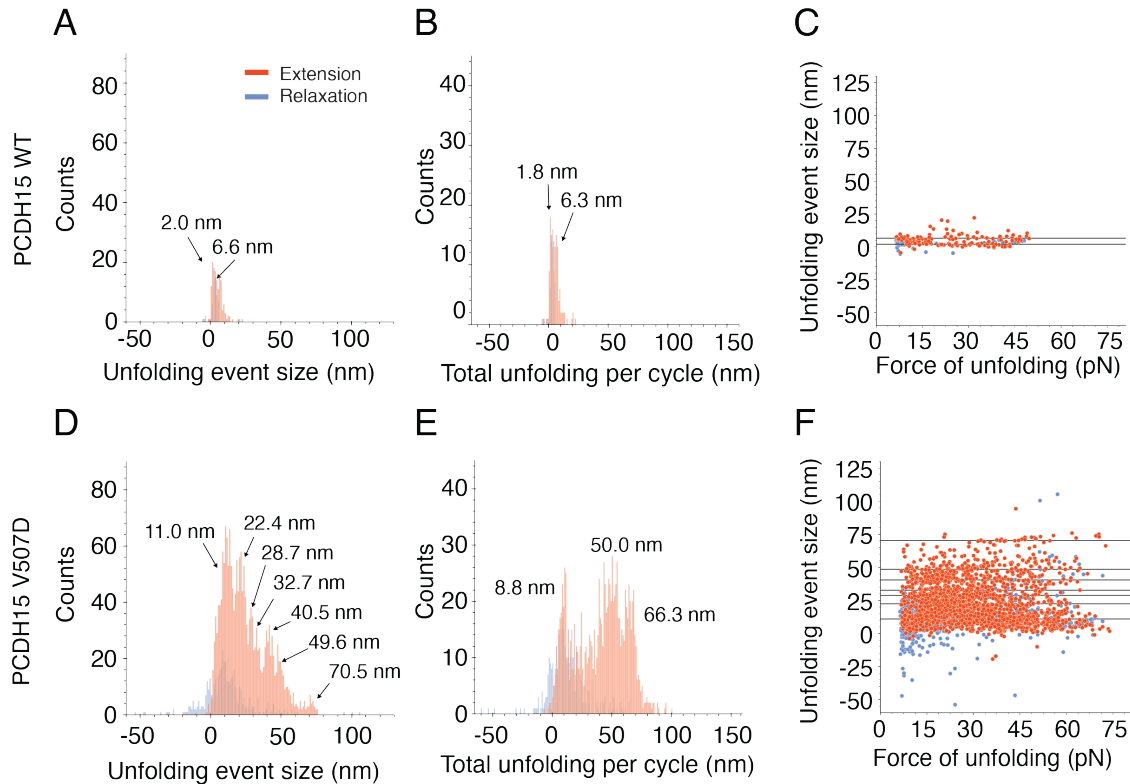


Figure 34. Wild-type PCDH15 underwent smaller magnitudes of unfolding events at saturating Ca^{2+} compared to V507D.

(A) In the wild type, discrete unfolding events occurred around 2.0 ± 0.1 nm and 6.6 ± 0.1 nm (means \pm SEMs; $N = 5$ datasets; $n = 140$ events). (B) The total unfolding per cycle was similar, with peaks at 1.8 ± 0.1 nm and 6.3 ± 0.2 nm (means \pm SEMs; $N = 5$ datasets; $n = 131$ events). (C) Many unfolding events occurred across a range of forces, though there was some preponderance of lower forces (panels A-C extracted from Figure 23). (D) At the same concentration of Ca^{2+} , V507D underwent numerous types of larger discrete unfolding events, with peaks at 11.0 ± 0.1 nm, 22.4 ± 0.1 nm, 28.7 ± 0.02 nm, 32.7 ± 0.04 nm, 40.5 ± 0.1 nm, 49.6 ± 0.2 nm, and 70.5 ± 0.1 nm (means \pm SEMs; $N = 24$ datasets; $n = 1889$ events). (E) The sum of unfolding per cycle reached values greater than those expected for unfolding of a full-length EC domain, with peaks at 8.8 ± 0.1 nm, 50.0 ± 0.2 nm, and 66.3 ± 0.2 nm (means \pm SEMs; $N = 24$ events; $n = 1144$ events). (F) The larger individual unfolding events tended to occur at lower forces (panels D-F extracted from Figure 27).

6.1.2 Physiological Ca^{2+}

At a physiological concentration of Ca^{2+} , $20 \mu\text{M}$, only about half of the Ca^{2+} binding sites in PCDH15 are expected to be occupied because the dissociation constant

of Ca^{2+} in the linker regions is close to the range of Ca^{2+} concentrations within the endolymph⁴¹. Therefore, I expected to see unique behavior of the wild-type and V507D PCDH15 at this level of Ca^{2+} . Upon inspection with TEM, they both had similar separation between the two strands of the dimer (Figure 35 A and B).

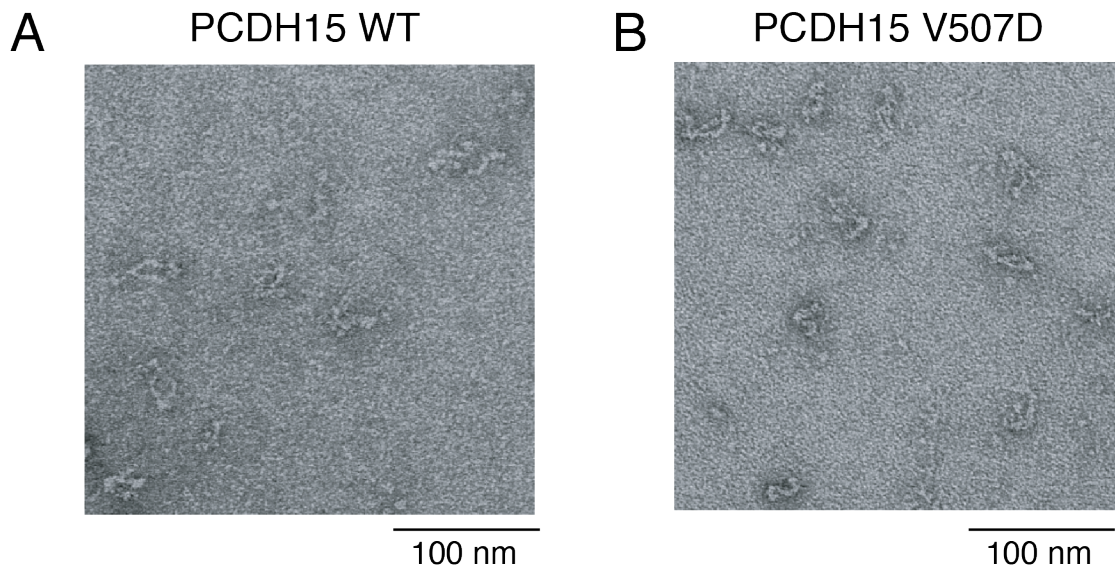


Figure 35. At a physiological level of Ca^{2+} , both the wild-type and V507D PCDH15 showed separation between the strands of the dimer on TEM.

(A) The wild-type PCDH15 molecules showed a gap between the two strands of the dimer, likely a result of the decreased stabilizing effect of Ca^{2+} (extracted from Figure 20). (B) The V507D molecules showed a similar bowing out of the two strands of the dimer at this level of Ca^{2+} (extracted from Figure 25).

Force ramp experiments on the wild type show that it underwent very few unfolding events at a physiological Ca^{2+} concentration (Figure 36A-D), but that it was softer than at a saturating Ca^{2+} concentration: it extended farther within the same force range. In contrast, V507D underwent many more types of unfolding events (Figure 36E-H), likely originating from instability in EC5.

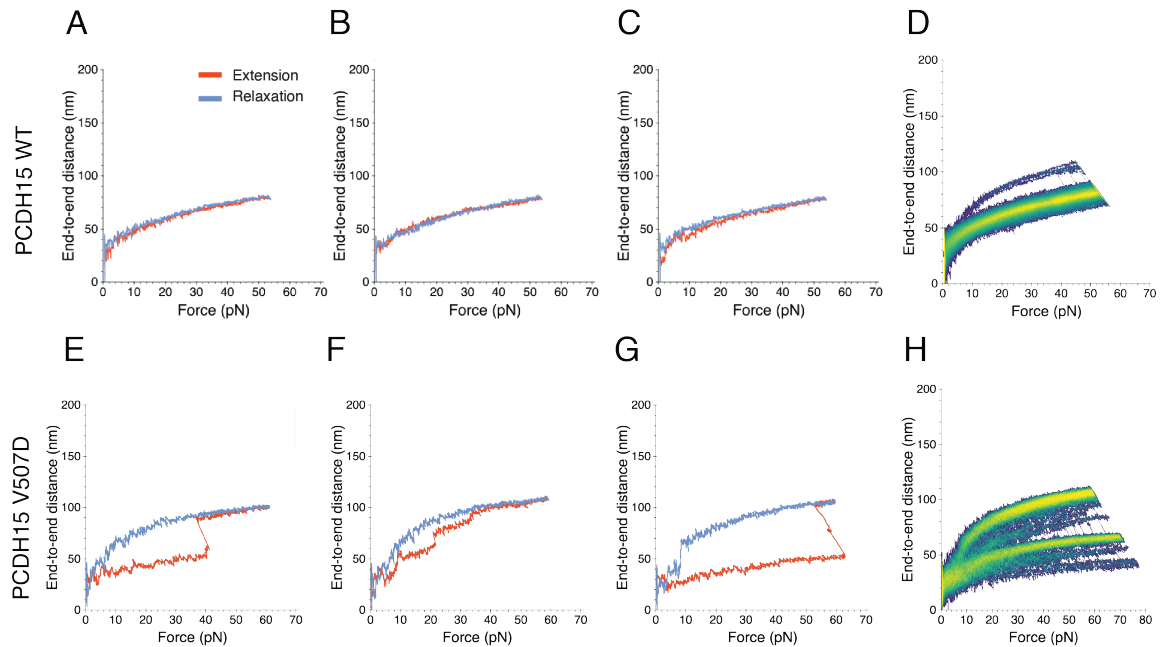


Figure 36. At a physiological concentration of Ca^{2+} , V507D unfolded more frequently than the wild-type PCDH15.

(A-C) Successive force ramp cycles of the wild-type protein show that it is more extensible than at higher Ca^{2+} , but that unfolding events are infrequent. (D) This behavior is reflected by the single bright branch on the illustrative heat map (panels A-D extracted from Figure 21). (E-G) Subsequent cycles of V507D show that it undergoes a unfolding events of different magnitudes. (H) The two bright branches on the heat map reflect the two main conformations accessed by V507D in this dataset, whereas the darker branches represent events that happened occasionally (panels E-H extracted from Figure 26).

In the wild-type protein, as at a saturating level of Ca^{2+} , both the size of discrete unfolding events and the total amount unfolded per cycle was below the range of unfolding expected from the linker regions, 16 nm. However, the wild type was more extensible at physiological Ca^{2+} than at saturating Ca^{2+} , despite a similar unfolding event pattern. It is possible that, because of the proximity of the dissociation constant of Ca^{2+} within the linker regions to the physiological range of Ca^{2+} , there is additional extension within the linker regions at baseline that resulted

in the softening of the wild type in the absence of additional unfolding events when force is applied.

In comparison, V507D at the same concentration of Ca^{2+} underwent unfolding events of higher magnitudes. The greatest of these peaks could correspond to the unfolding of an entire EC domain. Interestingly, we observed lower magnitudes of unfolding events in V507D at physiological Ca^{2+} than at a saturating level of Ca^{2+} , which is the opposite of what we expected. The reasons for this are unclear: perhaps at a physiological level of Ca^{2+} , the V507D protein is more reproducibly misfolded, resulting in less variability in unfolding events, while at a saturating level of Ca^{2+} the folding is more variable, resulting in a richer variety of unfolding behavior.

The enthalpic stiffnesses of the folded proteins are also significantly ($p = 0.0001$) different at this concentration of Ca^{2+} : the stiffness of the wild-type is $6.2 \pm 0.4 \text{ mN}\cdot\text{m}^{-1}$, whereas the stiffness of V507D is $4.3 \pm 0.2 \text{ mN}\cdot\text{m}^{-1}$. Although both of these values would result in overall tip-link stiffness values within the experimentally determined range of the gating spring, V507D unfolded much more frequently at a physiological level of Ca^{2+} compared to the wild type. The higher propensity of V507D to unfolding suggests that V507D functionally has a lower stiffness value than the calculated enthalpic stiffness value for the folded protein most of the time, which means that the overall stiffness of the tip link would be softer in the case of V507D. A softer overall tip link would then result in force being

transduced inappropriately to the MET channel, preventing channel opening and possibly resulting in deafness in those with this mutation.

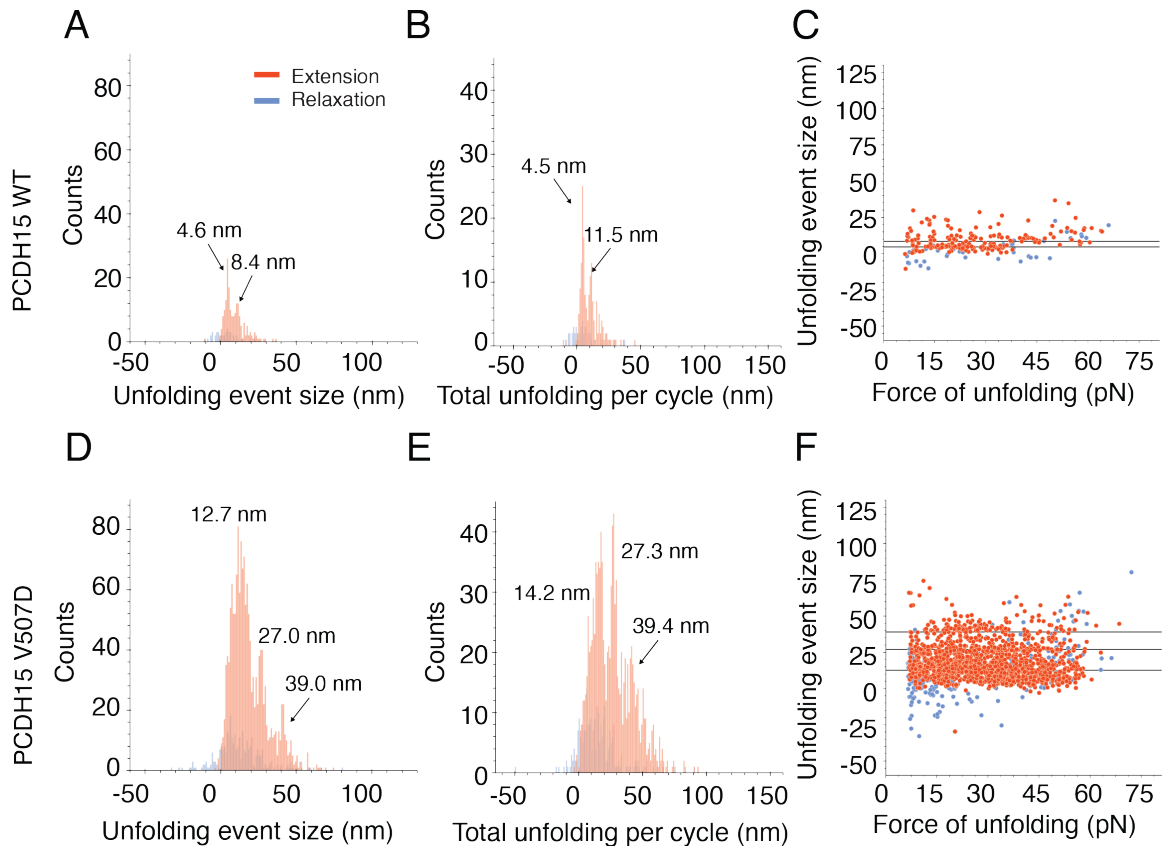


Figure 37. PCDH15 V507D underwent a larger variety and a higher magnitude of unfolding events at a physiological Ca^{2+} compared to the wild type.

(A) In the wild type, individual unfolding events were predominantly below 16 nm, the length expected for unfolding of the linker regions, with peaks at 4.6 ± 0.1 nm and 8.4 ± 0.4 nm (means \pm SEMs; $N = 4$ datasets; $n = 187$ events). (B) The total unfolding per cycle was also largely below 16 nm, with peaks at 4.5 ± 0.1 nm and 11.5 ± 0.1 nm (means \pm SEMs; $N = 4$ datasets; $n = 172$ events). (C) There was no clear relationship between the size of unfolding events and the force at which they occurred (panels A-C extracted from Figure 23). (D) In V507D, larger discrete events occurred, including events in the expected range for EC domain unfolding. The peaks occurred at 12.7 ± 0.2 nm, 27.0 ± 0.1 nm, and 39.0 ± 0.2 nm (means \pm SEMs; $N = 16$ datasets; $n = 1536$ events). (E) The magnitude of total unfolding per cycle was similar to the amount unfolding in individual events, with peaks at 14.2 ± 0.2 nm, 27.3 ± 0.1 nm, and 39.4 ± 0.3 nm (means \pm SEMs; $N = 16$ datasets; $n = 1081$ events). (F) There was a wide distribution of forces of unfolding, though larger unfolding events tended to occur at lower forces, whereas smaller unfolding

events had a more even distribution of unfolding forces (panels *D-F* extracted from Figure 27).

6.1.3 Absence of Ca^{2+}

When Ca^{2+} is removed completely, I expected both the wild-type and V507D PCDH15 to unfold more readily as a result of the complete loss of the stabilizing effect of Ca^{2+} . On TEM, both constructs exhibited a heterogeneous mix of molecules on the field of view. In the wild type, the two strands of the dimer were quite separated from each other, forming a large gap between them (Figure 38A). V507D showed similar separation between the strands (Figure 38B), but the structures are even more difficult to make out compared to the wild type, which could mean that V507D is folding improperly at this level of Ca^{2+} .

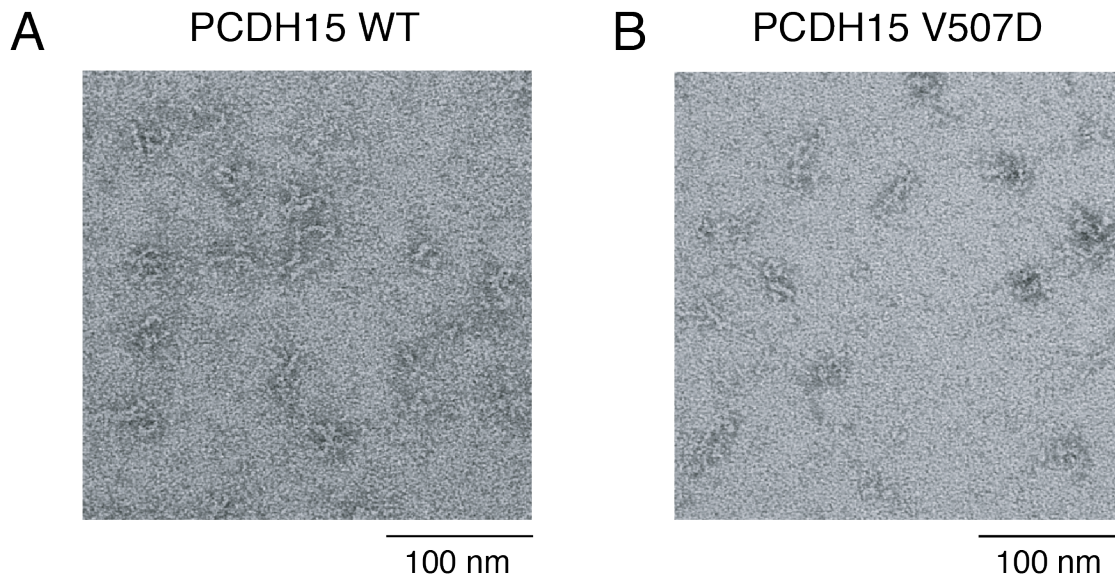


Figure 38. TEM imaging showed that both wild-type and V507D PCDH15 were conformationally heterogeneous in the absence of Ca^{2+} .

(A) In the wild-type protein, the two strands of the dimer bowed outwards from each other to a larger degree than at higher levels of Ca^{2+} (extracted from Figure 20). (B) In V507D, we also observed separation between the two strands of the dimer. However, the molecules themselves were more difficult to identify than at higher levels of Ca^{2+} (extracted from Figure 25).

In the absence of Ca^{2+} , both the wild-type and V507D PCDH15 underwent more frequent and larger unfolding events than compared to the higher levels of Ca^{2+} (Figure 39). However, the maximal end-to-end distances achieved by V507D far exceeded those visited by the wild type: at the highest forces, the end-to-end distance of V507D ranged from about 100 nm to as great as 200 nm (Figure 39H), whereas in the wild type the end-to-end distances at the highest forces ranged from 50 nm to about 100 nm (Figure 39D). The difference in magnitudes of maximal extension are impressive, considering that the only difference between these proteins is the V507D point mutation. This supports my proposed mechanism of deafness in those with the V507D mutation: there is a higher propensity to unfold to unusually large lengths, which likely results in decreased stiffness of PCDH15 and therefore the tip link overall and results in an inability to convey appropriate tension to the MET channels.

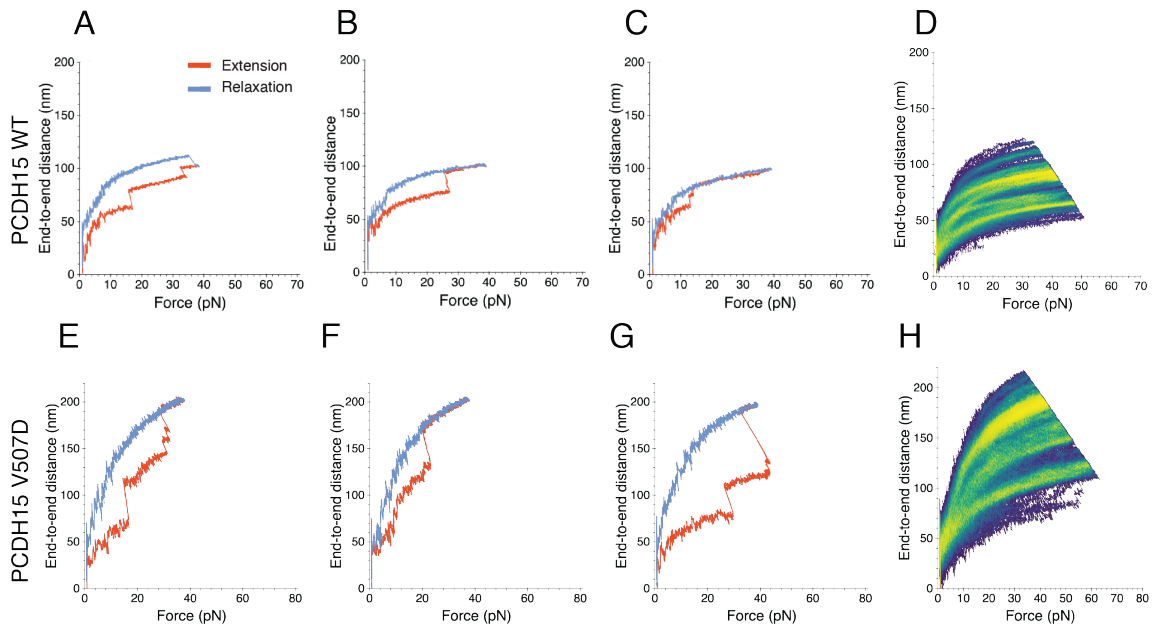


Figure 39. In the absence of Ca^{2+} , both the wild-type and V507D PCH15 exhibited a rich variety of unfolding behavior, though V507D was much more extended at baseline than the wild type.

(A-C) Subsequent cycles of the wild-type PCDH15 in the absence of Ca^{2+} show that it underwent various magnitudes of unfolding events. (D) The numerous bright branches on the illustrative heat map reflect the unfolding events seen in the individual cycles (panels A-D extracted from Figure 21). (E-G) V507D also exhibited significant unfolding, but extended more easily in response to force compared to the wild type. (H) The overall end-to-end distances reached by V507D were greater than that of the wild-type PCDH15 (panels E-H extracted from Figure 26).

In the wild type, the majority of both the discrete unfolding events (Figure 40A) and total unfolding per cycle (Figure 40B) fell below the range expected from full-length EC domain unfolding, which would be 33 nm to 45 nm, though events within and exceeding this range did still occur. This is in contrast to V507D, where the total unfolding per cycle was predominantly around 49.3 nm, greater than what would be expected for unfolding from an EC domain. However, that peak of unfolding does not correspond with the much greater range of end-to-

end distances observed in Figure 39H. Rather, the large range of end-to-end distances in the absence of corresponding unfolding events is likely a result of V507D being misfolded at baseline: when the applied force is low, such as during the resting period between force-ramp cycles, the two partially unfolded strands of the dimer might tangle with each other, resulting in a misfolded protein that extends easily when force is reapplied. This might happen because EC5 is more prone to unfolding due to the location of the mutation, which could then predispose the neighboring EC domains to unfold.

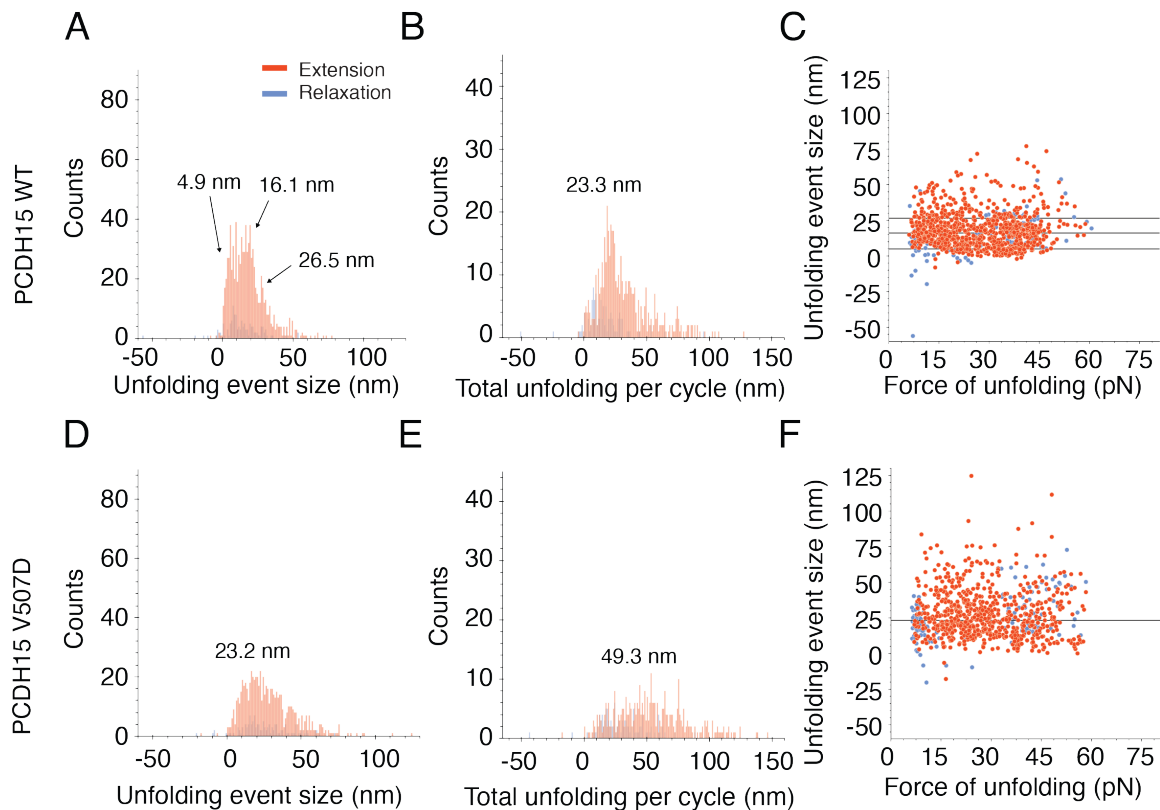


Figure 40. Wild-type PCDH15 had smaller magnitudes of unfolding events in the absence of Ca^{2+} compared to V507D.

(A) In the wild-type, discrete unfolding events peaked at 4.9 ± 0.1 nm, 16.1 ± 0.2 nm, and 26.5 ± 0.4 nm (means \pm SEMs; $N = 6$ datasets; $n = 868$ events). (B) The total unfolding per cycle was predominantly around $23.3 \text{ nm} \pm 0.6 \text{ nm}$ (means \pm SEMs; $N = 6$ datasets; $n = 490$ events), which is less than the length expected

from the unfolding of an entire EC domain. (C) There was no clear relationship between the size of an unfolding event and the force at which it occurred (panels *A-C* extracted from Figure 23). (D) In PCDH15 V507D, the individual unfolding events that occurred were largely around 23.2 ± 0.5 nm (means \pm SEMs; $N = 4$ datasets; $n = 694$ events). (E) The total unfolding per cycle peaked around 49.3 ± 1.4 nm (means \pm SEMs; $N = 4$ datasets; $n = 362$ events), but reached values as great as 150 nm. (F) There was no clear relationship between the size of unfolding event and its force of unfolding (panels *D-F* extracted from Figure 27).

6.2 Deafness-causing mutations in the tip link and therapeutic strategies

Though this work has focused on PCDH15, there are over 100 mutations in CDH23 that result in deafness²⁶. CDH23 is about 2.3 times as long as PCDH15, so we would expect there to be more deafness-mutations in CDH23 than PCDH15. However, there is also a higher rate of mutations in CDH23, which is not simply explained by the increased length^{26,82}. The reason for this is unclear, but evolutionary analyses suggest that CDH23 is more tolerant of mutations that reduce the stability of the protein—and cause deafness—but are not lethal⁸².

The behavior and predicted long-lasting effects of the V507D mutation contrasts with the *salsa* mutant identified in mice, which is an E737V point mutation in CDH23 that results in progressive non-syndromic deafness⁸³. The mutation interrupts a Ca^{2+} -binding site within CDH23, and the authors of the paper that identified the mutation conjectured that the mutation predisposed the tip links to breaking, and over time the tip link would not be able to regenerate quickly enough, resulting in progressive hearing loss. In the case of the V507D mutation in PCDH15, hearing loss is also non-syndromic but is not progressive, instead having a pre-lingual onset. Both of these point mutations cause non-syndromic hearing loss, but why one mutation—E737V, in a Ca^{2+} -binding site—results in progressive

hearing loss and the other mutation—V507D, in a β sheet—results in hearing loss from birth is not clear.

Gene therapy is a promising treatment strategy for deafness caused by genetic mutations. Adeno-associated viruses (AAVs) are often used because they have high infection efficiency, low toxicity, and because of their tropism certain strains can be used to target different cell types^{47,84,85}. One drawback is that at most 5 kb of genetic material can be packaged into the capsids, meaning that larger genes—such as PCDH15, at approximately 5.3 kb—are too large to fit into a single capsid⁴⁷. Alternative strategies include using dual-vector AAVs in which the gene of interest is split in between two capsids, but this can result in lower transduction efficiency due to the need to transduce cells with two plasmids^{47,86}. Another strategy involves creating shortened genes containing only the presumed essential components to create an adequately-functioning protein. This strategy has been used to create mini-dystrophin genes to attempt to treat Duchene muscular dystrophy⁸⁷. Recent work has used this mini-gene strategy to create shortened PCDH15 constructs to rescue hearing loss⁴⁷. Interestingly, rationally deleting 5 EC repeats not involved in the handshake or dimerization still resulted in tip link formation. The shortened PCDH15 constructs also rescued hearing loss and hair bundle morphology in mice with the R245X USH1F-causing mutation. These mini-PCDH15 results are encouraging from a treatment perspective, but are also interesting from a scientific perspective. What are the mechanical properties of these shortened constructs? Are they stiffer than the

wild type, or do the myosin motors at the upper end of the tip link work to keep the tip link at the same tension as the wild type despite the shorter construct? These answers to these questions are yet unanswered, and would be an interesting avenue of concurrent study with such mini-PCDH15 approaches.

6.3 Proposed mechanism of deafness with PCDH15 V507D

The Ca^{2+} concentration within the endolymph ranges from approximately 20 μM at the base to 40 μM at the apex⁷⁰. Furthermore, close to a transduction channel, the local depletion of Ca^{2+} might be significant: at a distance of 7 nm, the concentration of Ca^{2+} could fall to half its maximal value due to the flow of Ca^{2+} through the open channel⁸⁸. The length of a folded EC domain⁸⁹ is about 4.5 nm, so EC11 and the PICA domain could experience a significantly lower Ca^{2+} level: the behavior of PCDH15 in the distal domains might well lie between the results for physiological levels of Ca^{2+} and those in the ion's absence.

PCDH15 V507D is likely unable to refold on the appropriate timescale for normal hearing if such large unfolding events occur *in vivo*, resulting in a more compliant PCDH15 dimer and overall tip link (Figure 41A). Insufficient tension applied to the mechanotransduction channels might then be the mechanism of deafness in those with this mutation. More specifically, without an influx of Ca^{2+} through the MET channels, stereocilia within a hair bundle undergo remodeling, resulting in shorter stereocilia with a different tip shape⁹⁰. Moreover, if the MET current is abolished in inner hair cells, their innervation pattern changes over time: they become re-innervated by inhibitory efferent neurons, which normally

innervate inner hair cells only before the onset of hearing⁹¹. If PCDH15 V507D has insufficient ability to convey the appropriate tension to the MET channels and thus prevents their opening, this would result in stereociliary and neural remodeling over time, which could be the mechanism of long-term deafness in those with this mutation. Because of the multitudinous effects that MET channel closure has on hair cells, it would be revealing to examine the effects of the V507D mutation on hair bundle morphology and innervation *in vivo*. In particular, it would be necessary to understand whether PCDH15 V507D has any localization defects as a result of the mutation, though I do not expect such a disruption because those with the V507D mutation have appropriate vestibular and retinal function with the mutation.

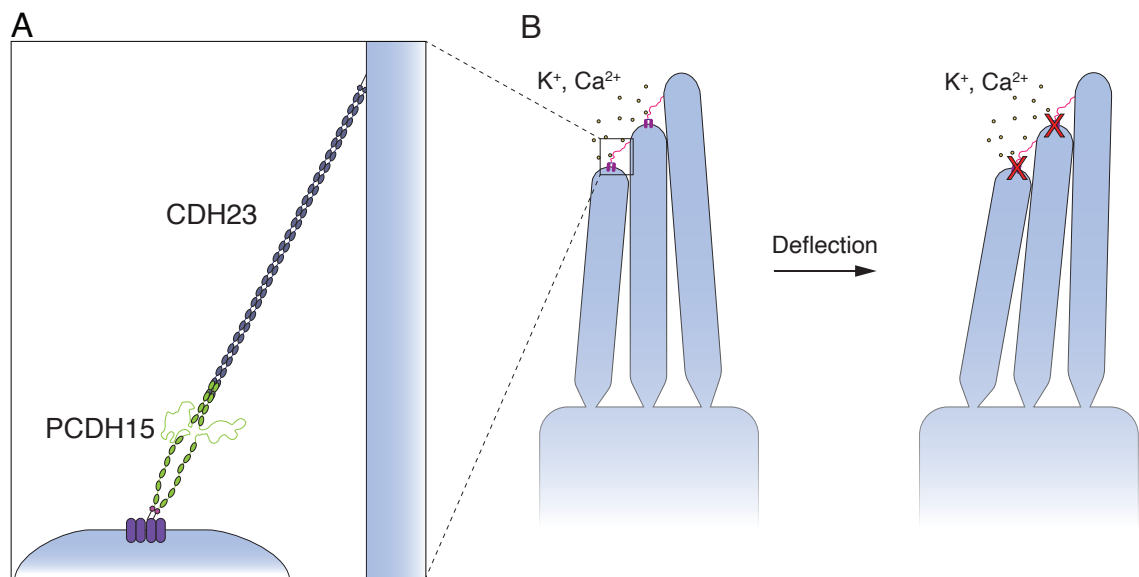


Figure 41. Proposed mechanism of deafness in PCDH15 V507D.

(A) Based on the data I gathered, PCDH15 V507D is likely to be partially unfolded, or misfolded, during the course of hearing. (B) As a result, the tip link has insufficient tension to open the MET channels when stimulated, preventing mechanotransduction and resulting in deafness.

If the V507D point mutation is so disruptive to the mechanics of PCDH15, why do individuals with this mutation have normal equilibrium and vision, despite the expression of PCDH15 in the vestibule and eye as well? It is possible that the higher concentration of Ca^{2+} in the vestibular labyrinth allows mutated PCDH15 to function adequately, whereas the lower concentration of Ca^{2+} in the cochlea precludes this. It is also possible that mutated protein can function adequately at the lower frequencies, less than 20 Hz, characteristic of the vestibular system⁹², but cannot perform well at the higher frequencies, up to 20 kHz, detected by the cochlea¹. It is likely that the mutated PCDH15 can no longer transmit the appropriate tension to the mechanotransduction channel, resulting in deafness. (Figure 41B).

Future work to elucidate the contributions of different parts of PCDH15 to the overall unfolding will be needed. It might be that, once one portion of the molecule unfolds, unfolding of the neighboring regions becomes more likely. This may be particularly true when the Ca^{2+} -binding sites are disrupted—because the Ca^{2+} ions are coordinated by residues in the linker region and the edges of the neighboring domains, if one of the neighboring domains unfolds then the coordinating residue in that domain may become displaced, resulting in the loss of that Ca^{2+} . The loss of the bound Ca^{2+} then predisposes the region to further unfolding. When the force on the protein is decreased, the end-to-end distance of the protein also decreases, which can allow for refolding to occur. However, if too much length has unfolded already, it is unlikely PCDH15 could refold properly.

The results presented in this work overall confirm that PCDH15 has the appropriate stiffness to form a component of the gating spring and that its physical properties can be modulated by Ca^{2+} . In the case of a hearing-loss mutation, PCDH15 unfolded much more frequently, was softer than the wild type, and had impaired refolding ability, three features that would likely result in inappropriate tension conveyed to the MET channels *in vivo*. These findings in this hearing loss mutation underscore how the tension conveyed to the MET channels is critical for normal hearing.

BIBLIOGRAPHY

1. Eric Kandel, John Koester & Mack, S. *Principles of Neural Science*. (McGraw Hill/Medical, 2021).
2. Holt, J. R. & Corey, D. P. Two mechanisms for transducer adaptation in vertebrate hair cells. *Proc. Natl. Acad. Sci.* **97**, 11730–11735 (2000).
3. Assad, J. & Corey, D. An active motor model for adaptation by vertebrate hair cells. *J. Neurosci.* **12**, 3291–3309 (1992).
4. Li, S. *et al.* Myosin-VIIa is expressed in multiple isoforms and essential for tensioning the hair cell mechanotransduction complex. *Nat. Commun.* **11**, 2066 (2020).
5. Holt, J. R. *et al.* A Chemical-Genetic Strategy Implicates Myosin-1c in Adaptation by Hair Cells. *Cell* **108**, 371–381 (2002).
6. Kurima, K. *et al.* TMC1 and TMC2 Localize at the Site of Mechanotransduction in Mammalian Inner Ear Hair Cell Stereocilia. *Cell Rep.* **12**, 1606–1617 (2015).
7. Pan, B. *et al.* TMC1 Forms the Pore of Mechanosensory Transduction Channels in Vertebrate Inner Ear Hair Cells. *Neuron* **99**, 736-753.e6 (2018).
8. Pan, B. *et al.* TMC1 and TMC2 Are Components of the Mechanotransduction Channel in Hair Cells of the Mammalian Inner Ear. *Neuron* **79**, 504–515 (2013).

9. Fettiplace, R., Furness, D. N. & Beurg, M. The conductance and organization of the TMC1-containing mechanotransducer channel complex in auditory hair cells. *Proc. Natl. Acad. Sci.* **119**, e2210849119 (2022).
10. Kawashima, Y. *et al.* Mechanotransduction in mouse inner ear hair cells requires transmembrane channel-like genes. *J. Clin. Invest.* **121**, 4796–4809 (2011).
11. Ge, J. *et al.* Structure of mouse protocadherin 15 of the stereocilia tip link in complex with LHFPL5. *eLife* **7**, e38770 (2018).
12. Wu, Z. & Müller, U. Molecular Identity of the Mechanotransduction Channel in Hair Cells: Not Quiet There Yet. *J. Neurosci.* **36**, 10927–10934 (2016).
13. Zhao, B. *et al.* TMIE is an essential component of the mechanotransduction machinery of cochlear hair cells. *Neuron* **84**, 954–967 (2014).
14. Qiu, X., Liang, X., Llongueras, J. P., Cunningham, C. & Müller, U. The tetraspan LHFPL5 is critical to establish maximal force sensitivity of the mechanotransduction channel of cochlear hair cells. *Cell Rep.* **42**, 112245 (2023).
15. Xiong, W. *et al.* TMHS is an Integral Component of the Mechanotransduction Machinery of Cochlear Hair Cells. *Cell* **151**, 1283–1295 (2012).
16. Corey, D. P. & Hudspeth, A. J. Response latency of vertebrate hair cells. *Biophys. J.* **26**, 499–506 (1979).

17. Howard, J. & Hudspeth, A. J. Compliance of the hair bundle associated with gating of mechano-electrical transduction channels in the Bullfrog's saccular hair cell. *Neuron* **1**, 189–199 (1988).
18. Kazmierczak, P. *et al.* Cadherin 23 and protocadherin 15 interact to form tip-link filaments in sensory hair cells. *Nature* **449**, 87–91 (2007).
19. Assad, J. A., Shepherd, G. M. G. & Corey, D. P. Tip-link integrity and mechanical transduction in vertebrate hair cells. *Neuron* **7**, 985–994 (1991).
20. Zhao, Y. -d., Yamoah, E. N. & Gillespie, P. G. Regeneration of broken tip links and restoration of mechanical transduction in hair cells. *Proc. Natl. Acad. Sci.* **93**, 15469–15474 (1996).
21. Alonso, R. G., Tobin, M., Martin, P. & Hudspeth, A. J. Fast recovery of disrupted tip links induced by mechanical displacement of hair bundles. *Proc. Natl. Acad. Sci. U. S. A.* **117**, 30722–30727 (2020).
22. Tobin, M., Chaiyasitdhi, A., Michel, V., Michalski, N. & Martin, P. Stiffness and tension gradients of the hair cell's tip-link complex in the mammalian cochlea. *eLife* **8**, e43473 (2019).
23. Ahmed, Z. M. *et al.* Gene structure and mutant alleles of PCDH15: nonsyndromic deafness DFNB23 and type 1 Usher syndrome. *Hum. Genet.* **124**, 215–223 (2008).
24. Ahmed, Z. M. PCDH15 is expressed in the neurosensory epithelium of the eye and ear and mutant alleles are responsible for both USH1F and DFNB23. *Hum. Mol. Genet.* **12**, 3215–3223 (2003).

25. Ahmed, Z. M. *et al.* Mutations of the Protocadherin Gene PCDH15 Cause Usher Syndrome Type 1F. *Am. J. Hum. Genet.* **69**, 25–34 (2001).
26. Jaiganesh, A., Narui, Y., Araya-Secchi, R. & Sotomayor, M. Beyond Cell–Cell Adhesion: Sensational Cadherins for Hearing and Balance. *Cold Spring Harb. Perspect. Biol.* **10**, a029280 (2018).
27. Maître, J.-L. & Heisenberg, C.-P. Three Functions of Cadherins in Cell Adhesion. *Curr. Biol.* **23**, R626–R633 (2013).
28. Shapiro, L., Fannont, A. M., Kwong, P. D. & Thompson, A. Structural basis of cell-cell adhesion by cadherins. **374**, 11 (1995).
29. Sotomayor, M., Weihofen, W. A., Gaudet, R. & Corey, D. P. Structure of a force-conveying cadherin bond essential for inner-ear mechanotransduction. *Nature* **492**, 128–132 (2012).
30. Mulhall, E. M. *et al.* Single-molecule force spectroscopy reveals the dynamic strength of the hair-cell tip-link connection. *Nat. Commun.* **12**, 849 (2021).
31. Jaiganesh, A. *et al.* Zooming in on Cadherin-23: Structural Diversity and Potential Mechanisms of Inherited Deafness. *Structure* **26**, 1210-1225.e4 (2018).
32. Pokutta, S., Herrenknecht, K., Kemler, R. & Engel, J. Conformational changes of the recombinant extracellular domain of E-cadherin upon calcium binding. *Eur. J. Biochem.* **223**, 1019–1026 (1994).

33. Maeda, R. *et al.* Tip-link protein protocadherin 15 interacts with transmembrane channel-like proteins TMC1 and TMC2. *Proc. Natl. Acad. Sci. U. S. A.* **111**, 12907–12912 (2014).
34. Grati, M. & Kachar, B. Myosin VIIa and sans localization at stereocilia upper tip-link density implicates these Usher syndrome proteins in mechanotransduction. *Proc. Natl. Acad. Sci.* **108**, 11476–11481 (2011).
35. Xu, Z., Ricci, A. J. & Heller, S. Rethinking How Hearing Happens. *Neuron* **62**, 305–307 (2009).
36. Ahmed, Z. M. *et al.* The Tip-Link Antigen, a Protein Associated with the Transduction Complex of Sensory Hair Cells, Is Protocadherin-15. *J. Neurosci.* **26**, 7022–7034 (2006).
37. PCDH15: Chr10 - Genome Data Viewer - NCBI.
<https://www.ncbi.nlm.nih.gov/genome/gdv/browser/gene/?id=65217>.
38. Dionne, G. *et al.* Mechanotransduction by PCDH15 Relies on a Novel cis-Dimeric Architecture. *Neuron* **99**, 480-492.e5 (2018).
39. Sotomayor, M. Communication about extracellular cadherin domain sequences. (2021).
40. Powers, R. E., Gaudet, R. & Sotomayor, M. A partial calcium-free linker confers flexibility to inner-ear protocadherin-15. *Struct. Lond. Engl.* **1993** **25**, 482–495 (2017).

41. Choudhary, D. *et al.* Structural determinants of protocadherin-15 mechanics and function in hearing and balance perception. *Proc. Natl. Acad. Sci.* **117**, 24837–24848 (2020).
42. De-la-Torre, P., Choudhary, D., Araya-Secchi, R., Narui, Y. & Sotomayor, M. A Mechanically Weak Extracellular Membrane-Adjacent Domain Induces Dimerization of Protocadherin-15. *Biophys. J.* **115**, 2368–2385 (2018).
43. Webb, S. W. *et al.* Regulation of PCDH15 function in mechanosensory hair cells by alternative splicing of the cytoplasmic domain. *Dev. Camb. Engl.* **138**, 1607–1617 (2011).
44. Maeda, R., Pacentine, I. V., Erickson, T. & Nicolson, T. Functional Analysis of the Transmembrane and Cytoplasmic Domains of Pcdh15a in Zebrafish Hair Cells. *J. Neurosci.* **37**, 3231–3245 (2017).
45. Mathur, P. & Yang, J. Usher syndrome: Hearing loss, retinal degeneration and associated abnormalities. *Biochim. Biophys. Acta BBA - Mol. Basis Dis.* **1852**, 406–420 (2015).
46. Schietroma, C. *et al.* Usher syndrome type 1–associated cadherins shape the photoreceptor outer segment. *J. Cell Biol.* **216**, 1849–1864 (2017).
47. Ivanchenko, M. V. *et al.* Mini-PCDH15 gene therapy rescues hearing in a mouse model of Usher syndrome type 1F. *Nat. Commun.* **14**, 2400 (2023).
48. Ashkin, A. Acceleration and Trapping of Particles by Radiation Pressure. *Phys. Rev. Lett.* **24**, 156–159 (1970).

49. Neuman, K. C. & Nagy, A. Single-molecule force spectroscopy: optical tweezers, magnetic tweezers and atomic force microscopy. *Nat. Methods* **5**, 491–505 (2008).
50. Bustamante, C., Chemla, Y., Liu, S. & Wang, M. Optical tweezers in single-molecule biophysics. <https://www.nature.com/articles/s43586-021-00021-6>.
51. Neuman, K. C. & Block, S. M. Optical trapping. *Rev. Sci. Instrum.* **75**, 2787–2809 (2004).
52. Tweezers LAB : The MiniTweezers. http://tweezerslab.unipr.it/cgi-bin/home.pl/View?doc=The_MiniTweezers.html.
53. Sotomayor, M., Corey, D. P. & Schulten, K. In Search of the Hair-Cell Gating Spring: Elastic Properties of Ankyrin and Cadherin Repeats. *Structure* **13**, 669–682 (2005).
54. Villasante, C. M., Deng, X., Cohen, J. E. & Hudspeth, A. J. Nanomechanics of wild-type and mutant dimers of the tip-link protein protocadherin 15. 2023.10.17.562769 Preprint at <https://doi.org/10.1101/2023.10.17.562769> (2023).
55. Tischer, C., Pralle, A. & Florin, E.-L. Determination and Correction of Position Detection Nonlinearity in Single Particle Tracking and Three-Dimensional Scanning Probe Microscopy. *Microsc. Microanal.* **10**, 425–434 (2004).
56. Volpe, G. & Volpe, G. Simulation of a Brownian particle in an optical trap. *Am. J. Phys.* **81**, 224–230 (2013).

56. Selvin, P. Optical Traps. Class lecture. University of Illinois at Urbana-Champaign.
[https://courses.engr.illinois.edu/phys475/fa2017/Lec15%20Spr12%20Optical TrapsII%20030712presented.pdf](https://courses.engr.illinois.edu/phys475/fa2017/Lec15%20Spr12%20Optical%20TrapsII%20030712presented.pdf)
58. 1.4: The Langevin Equation. *Chemistry LibreTexts*
[https://chem.libretexts.org/Bookshelves/Physical_and_Theoretical_Chemistry_Textbook_Maps/Non-Equilibrium_Statistical_Mechanics_\(Cao\)/01%3A_Stochastic_Processes_and_Brownian_Motion/1.04%3A_The_Langevin_Equation](https://chem.libretexts.org/Bookshelves/Physical_and_Theoretical_Chemistry_Textbook_Maps/Non-Equilibrium_Statistical_Mechanics_(Cao)/01%3A_Stochastic_Processes_and_Brownian_Motion/1.04%3A_The_Langevin_Equation) (2022).
59. Nelson, Philip. *Biological Physics: Energy, Information, Life*. (Chiliagon Science, 2020).
60. Bartsch, T. F. *et al.* Measurement of hindered diffusion in complex geometries for high-speed studies of single-molecule forces. *Sci. Rep.* **11**, 2196 (2021).
61. Pockels Cells. <https://www.thorlabs.com>.
62. Berg-Sørensen, K. & Flyvbjerg, H. Power spectrum analysis for optical tweezers. *Rev. Sci. Instrum.* **75**, 594–612 (2004).
63. Kauert, D. J., Kurth, T., Liedl, T. & Seidel, R. Direct Mechanical Measurements Reveal the Material Properties of Three-Dimensional DNA Origami. *Nano Lett.* **11**, 5558–5563 (2011).
64. Kellermayer, M. S. Z., Smith, S. B., Granzier, H. L. & Bustamante, C. Folding-Unfolding Transitions in Single Titin Molecules Characterized with Laser Tweezers. *Science* **276**, 1112–1116 (1997).

65. Bartsch, T. F. *et al.* Elasticity of individual protocadherin 15 molecules implicates tip links as the gating springs for hearing. *Proc. Natl. Acad. Sci.* **116**, 11048–11056 (2019).
66. Jeney, S., Stelzer, E. H. K., Grubmüller, H. & Florin, E.-L. Mechanical Properties of Single Motor Molecules Studied by Three-Dimensional Thermal Force Probing in Optical Tweezers. *ChemPhysChem* **5**, 1150–1158 (2004).
67. Bartsch, T. F. *et al.* Detecting Sequential Bond Formation Using Three-Dimensional Thermal Fluctuation Analysis. *ChemPhysChem* **10**, 1541–1547 (2009).
68. Ashkin, A. Forces of a single-beam gradient laser trap on a dielectric sphere in the ray optics regime. *Biophys. J.* **61**, 569–582 (1992).
69. Boshier, S. K. & Warren, R. L. Very low calcium content of cochlear endolymph, an extracellular fluid. *Nature* **273**, 377–378 (1978).
70. Salt, A. N., Inamura, N., Thalmann, R. & Vora, A. Calcium gradients in inner ear endolymph. *Am. J. Otolaryngol.* **10**, 371–375 (1989).
71. Ikeda, K., Kusakari, J., Takasaka, T. & Saito, Y. The Ca²⁺ activity of cochlear endolymph of the guinea pig and the effect of inhibitors. *Hear. Res.* **26**, 117–125 (1987).
72. Goldstein, D. A. Serum Calcium. in *Clinical Methods: The History, Physical, and Laboratory Examinations* (eds. Walker, H. K., Hall, W. D. & Hurst, J. W.) (Butterworths, 1990).

73. Sotomayor, M., Weihofen, W. A., Gaudet, R. & Corey, D. P. Structural Determinants of Cadherin-23 Function in Hearing and Deafness. *Neuron* **66**, 85–100 (2010).
74. Rayner, L. E. *et al.* The Solution Structures of Two Human IgG1 Antibodies Show Conformational Stability and Accommodate Their C1q and FcγR Ligands. *J. Biol. Chem.* **290**, 8420–8438 (2015).
75. Zakeri, B. *et al.* Peptide tag forming a rapid covalent bond to a protein, through engineering a bacterial adhesin. *Proc. Natl. Acad. Sci. U. S. A.* **109**, E690–E697 (2012).
76. Kepner, G. R. Saturation Behavior: a general relationship described by a simple second-order differential equation. *Theor. Biol. Med. Model.* **7**, 11 (2010).
77. Araya-Secchi, R., Neel, B. L. & Sotomayor, M. An elastic element in the protocadherin-15 tip link of the inner ear. *Nat. Commun.* **7**, 13458 (2016).
78. Ainaravapu, S. R. K. *et al.* Contour Length and Refolding Rate of a Small Protein Controlled by Engineered Disulfide Bonds. *Biophys. J.* **92**, 225–233 (2007).
79. Astuto, L. M. *et al.* Genetic Heterogeneity of Usher Syndrome: Analysis of 151 Families with Usher Type I. *Am. J. Hum. Genet.* **67**, 1569–1574 (2000).
80. Doucette, L. *et al.* Profound, prelingual nonsyndromic deafness maps to chromosome 10q21 and is caused by a novel missense mutation in the

- Usher syndrome type IF gene PCDH15. *Eur. J. Hum. Genet.* **17**, 554–564 (2009).
81. Markham, R., Frey, S. & Hills, G. J. Methods for the enhancement of image detail and accentuation of structure in electron microscopy. *Virology* **20**, 88–102 (1963).
82. Nisler, C. R. *et al.* Interpreting the Evolutionary Echoes of a Protein Complex Essential for Inner-Ear Mechanosensation. *Mol. Biol. Evol.* **40**, msad057 (2023).
83. Schwander, M. *et al.* A mouse model for nonsyndromic deafness (DFNB12) links hearing loss to defects in tip links of mechanosensory hair cells. *Proc. Natl. Acad. Sci.* **106**, 5252–5257 (2009).
84. Lustig, L. & Akil, O. Cochlear Gene Therapy. *Cold Spring Harb. Perspect. Med.* **9**, a033191 (2019).
85. Qi, J. *et al.* Current AAV-mediated gene therapy in sensorineural hearing loss. *Fundam. Res.* (2022) doi:10.1016/j.fmre.2022.08.015.
86. Akil, O. Dual and triple AAV delivery of large therapeutic gene sequences into the inner ear. *Hear. Res.* **394**, 107912 (2020).
87. Zhang, Y. & Duan, D. Novel Mini-Dystrophin Gene Dual Adeno-Associated Virus Vectors Restore Neuronal Nitric Oxide Synthase Expression at the Sarcolemma. *Hum. Gene Ther.* **23**, 98–103 (2012).
88. Hudspeth, A. J. Local modulation of the endolymphatic Ca²⁺ concentration by flow through mechanoelectrical - transduction channels. Unpublished.

89. Shapiro, L., Fannont, A. M., Kwong, P. D. & Thompson, A. Structural basis of cell-cell adhesion by cadherins. **374**, 11 (1995).
90. Vélez-Ortega, A. C., Freeman, M. J., Indzhukulian, A. A., Grossheim, J. M. & Frolenkov, G. I. Mechanotransduction current is essential for stability of the transducing stereocilia in mammalian auditory hair cells. *eLife* **6**, e24661 (2017).
91. Corns, L. F. *et al.* Mechanotransduction is required for establishing and maintaining mature inner hair cells and regulating efferent innervation. *Nat. Commun.* **9**, 4015 (2018).
92. Carriot, J., Jamali, M., Chacron, M. J. & Cullen, K. E. Statistics of the Vestibular Input Experienced during Natural Self-Motion: Implications for Neural Processing. *J. Neurosci.* **34**, 8347–8357 (2014).

APPENDIX A: Additional completed works

Bartsch, T.F., Villasante, C.M., Hengel, F.E. *et al.* Measurement of hindered diffusion in complex geometries for high-speed studies of single-molecule forces. *Sci Rep* **11**, 2196 (2021). <https://doi.org/10.1038/s41598-021-81593-x>

Villasante C.M., Deng X., Cohen J.E., Hudspeth A.J. Nanomechanics of wild-type and mutant dimers of the tip-link protein protocadherin 15. *BioRxiv*: <https://doi.org/10.1101/2023.10.17.562769>. October 2023.



OPEN

Measurement of hindered diffusion in complex geometries for high-speed studies of single-molecule forces

Tobias F. Bartsch^{1,4}, Camila M. Villasante^{1,4}, Felicitas E. Hengel^{1,2,4}, Ahmed Touré^{1,3}, Daniel M. Firester¹, Aaron Oswald^{1,3} & A. J. Hudspeth¹

In a high-speed single-molecule experiment with a force probe, a protein is tethered between two substrates that are manipulated to exert force on the system. To avoid nonspecific interactions between the protein and nearby substrates, the protein is usually attached to the substrates through long, flexible linkers. This approach precludes measurements of mechanical properties with high spatial and temporal resolution, for rapidly exerted forces are dissipated into the linkers. Because mammalian hearing operates at frequencies reaching tens to hundreds of kilohertz, the mechanical processes that occur during transduction are of very short duration. Single-molecule experiments on the relevant proteins therefore cannot involve long tethers. We previously characterized the mechanical properties of protocadherin 15 (PCDH15), a protein essential for human hearing, by tethering an individual monomer through very short linkers between a probe bead held in an optical trap and a pedestal bead immobilized on a glass coverslip. Because the two confining surfaces were separated by only the length of the tethered protein, hydrodynamic coupling between those surfaces complicated the interpretation of the data. To facilitate our experiments, we characterize here the anisotropic and position-dependent diffusion coefficient of a probe in the presence of an effectively infinite wall, the coverslip, and of the immobile pedestal.

A protein under tension exhibits both entropic and enthalpic elasticity, a behavior that can be measured by observing the elongation of a single molecule while applying mechanical force. In such an experiment, the molecule is placed between two substrates, at least one of which is part of an elastic transducer through which forces can be delivered, for example an optically trapped, micrometer-sized bead. To avoid non-specific interactions between the protein and the substrates to which it is attached, the protein is usually secured through long, flexible DNA or PEG spacers^{1,2}. As a consequence, the fluctuations in the protein's instantaneous position are filtered with a time constant of γ/κ , in which γ is the drag coefficient of the bead and κ is the total stiffness of the potential confining the bead, which comprises the spring constants of the optical trap, protein, and spacers. The position of the bead therefore reflects only the time-averaged end-to-end length of the protein. Moreover, information about the stiffness of the folded protein is concealed by the usually softer linker and often cannot be extracted from the measured force-extension relation. Resolving small structural changes and measuring the elasticity of folded proteins therefore remain challenging tasks that have recently been addressed through novel approaches. The fine structure of the energy landscape of DNA hairpins, for example, was measured with rigid DNA-origami spacers with a persistence length 50-fold as great as the commonly used double-stranded DNA linkers³. Rigid spacers couple the motion of the protein's ends tightly to the position of the bead, thereby increasing the bandwidth and precision of the experiment.

We developed a novel single-molecule assay that did not require long, flexible spacers⁴. The protein was instead stretched directly between a diffusing probe—a 1 μm -diameter plastic bead to which force could be applied by optical tweezers—and an immobile glass pedestal—a 2 μm -diameter bead fixed to the coverslip. The protein's ends were attached to the two beads through distinct, short, and relatively inelastic linkers. A similar

¹Howard Hughes Medical Institute and Laboratory of Sensory Neuroscience, The Rockefeller University, New York, NY 10065, USA. ²Present address: Faculty of Medicine, Ruprecht-Karls-Universität, 69120 Heidelberg, Germany. ³Present address: Weill Cornell Medical College, 1300 York Avenue, New York, NY 10065, USA. ⁴These authors contributed equally: Tobias F. Bartsch, Camila M. Villasante, and Felicitas E. Hengel. ✉email: tobias.bartsch@gmail.com; hudspaj@rockefeller.edu

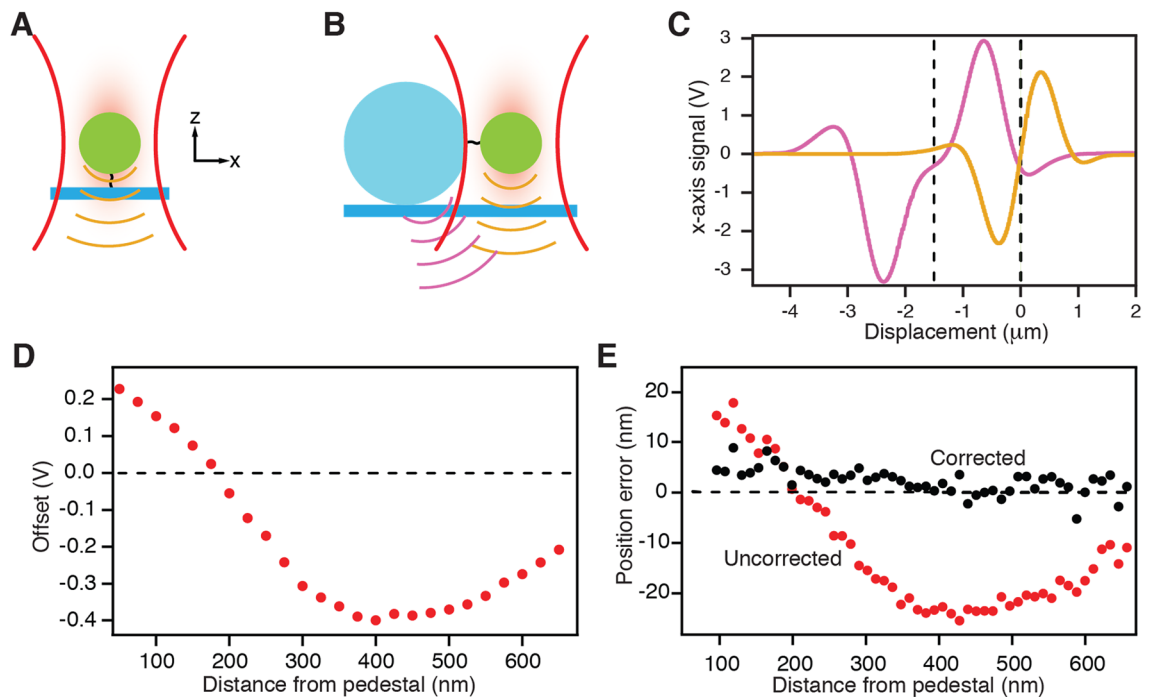


Figure 1. Apparatus and control experiments. **(A)** When a probe is held in an optical trap (red), its position can be measured along three axes by capturing transmitted and forward-scattered light (orange) on a quadrant photodiode. **(B)** A stationary pedestal, to which one end of a filamentous protein is attached, scatters a small fraction of the incident light and contaminates the desired signal for the probe. **(C)** Control measurements show the signals as a function of offset position due to the probe alone and to the pedestal alone. The two signals have been offset by 1.5 μm (dashed lines) to simulate the configuration during an actual experiment. **(D)** With the probe fixed in place, moving the pedestal nearby produces a spurious offset signal. The dashed line shows the reference signal for the probe far from the pedestal. **(E)** The systematic error in position measurements owing to the pedestal is reduced by the compensation procedure to a few nanometers.

approach was taken in previous work that studied the force-extension of whole titin molecules and of the molecular motor kinesin with optical tweezers^{5,6}. Force-extension studies with atomic-force microscopes also sometimes avoid flexible spacers, albeit usually at the expense of non-specific anchoring of the target protein to at least one of the confining surfaces⁷.

Our method allowed us to characterize the equilibrium mechanics of protocadherin 15 (PCDH15), a protein whose properties implicate it as part of a molecular spring important for hearing⁴. Determining the entropic and enthalpic stiffness of the protein is crucial for our understanding of the molecular basis of mechanotransduction by the inner ear. Human ears can detect sounds at frequencies up to 20 kHz, and some bats and dolphins have a hearing range exceeding 200 kHz. The protein machinery that underlies hearing must therefore be capable of responding to very fast stimuli that likely produce mechanical responses far from thermal equilibrium. For two reasons, this high-frequency behavior has not been explored through single-molecule experiments. First, in the presence of flexible linker molecules, high-frequency force stimuli are largely filtered before they can elongate a protein of interest. Second, even in the absence of flexible linkers, the mechanical response of a protein is filtered owing to the drag on the bead and the stiffness of the optical potential that confines it. If these filtering effects are not too large compared to the time constant of the protein's response, and if the diffusion coefficients at critical locations in the experimental volume are known, it is nevertheless possible to compensate for the filtering. In this study we characterize the anisotropic and position-dependent diffusion coefficient of a bead in our single-molecule assay in the presence of an effectively infinite wall, the coverslip, and of an immobile spherical obstacle, the pedestal. The results should facilitate analysis of high-speed studies of single-molecule forces relevant to auditory transduction.

Results

Correction of the position signal for light scattered by the pedestal. Determining the diffusion coefficients near a coverslip and pedestal requires high-precision measurement of the three-dimensional diffusion of a probe confined in a weak, position-sensing optical trap. The probe's position can be estimated with sub-nanometer precision and microsecond temporal resolution by interfering the light scattered forward by the probe with the unscattered portion of the trapping beam on a quadrant photodiode⁸ (Fig. 1A). The diode's difference signals are then linearly related to the probe's position along the two axes perpendicular to the optical axis, and the signal summed over all four quadrants is proportional to the probe's axial position.

When the probe and pedestal are in close proximity—as is the case in single-molecule experiments without long linkers—the position-sensing beam is scattered not only by the probe, but also by the pedestal (Fig. 1B).

Although this effect complicates estimation of the probe's position, the diode's total signal S_{total} can be approximated to first order as the sum of two independent signals^{9,10}: the signal $S_{pedestal}$ owing to the pedestal in the absence of the probe and the signal S_{probe} owing to the probe in the absence of the pedestal:

$$S_{total}(b_{pedestal}, b_{probe}) = S_{pedestal}(b_{pedestal}) + S_{probe}(b_{probe}) \quad (1)$$

Here the vectors b represent the position coordinates of the probe and pedestal, which are the displacements of the respective objects from their positions when the photodiode's output is zero. The offset $S_{pedestal}$ is sensitive to the precise value of the distance $b_{pedestal}$ as well as to the shape of the pedestal itself, and must therefore be determined at the beginning of each experiment.

In a typical experiment, the pedestal is fixed at least 1.5 μm from the focal spot of the position-sensing beam, a distance determined by the radii of the pedestal and probe. The probe's diffusion is confined by the beam's trapping potential and is centered on the focal spot. The pedestal's signal thus constitutes a constant offset added to the probe's signal. If the magnitude of this offset is known, it can be subtracted from the total signal to yield the signal of the probe alone⁴.

To visualize the contributions of the two independent signals, we independently recorded the signals for displacements of the probe and the pedestal, then displayed them offset by 1.5 μm relative to one another (Fig. 1C and Supplementary Information). This procedure reflected the case in which the probe was at the center of the position-sensing optical trap, defined as $x=0$, and just touched the pedestal. If the signal S_{probe} was held constant by fixing the probe's displacement b_{probe} from the focus of the position-sensing trap, then the offset could be determined by monitoring how the measured total signal S_{total} changed as the pedestal was brought progressively closer to the focal spot. Holding b_{probe} constant by means of a second optical trap that strongly confined the probe at a displacement of 100 nm with respect to the focus of the position-sensing beam, we then recorded the total detector signal while the pedestal was so distant that its signal was negligible ($S_{pedestal} \approx 0$). This signal served as a reference. As we moved the pedestal toward the focal spot of the position-sensing beam while keeping the probe confined at a constant position with the second trap, the deviation in S_{total} represented the signal $S_{pedestal}$ owing to the pedestal (Fig. 1D).

In order to demonstrate that we could successfully correct for the influence of the pedestal, we next used the stimulus trap to hold the probe at the center of the position-sensing trap ($x=0$). We recorded the photodiode's total signal and recovered the position of the probe by subtracting the offset caused by the pedestal. The position signal after compensation was nearly zero (Fig. 1E). If the offset correction was not performed and the total signal on the detector was calibrated without subtraction of the pedestal's influence, a significant systematic position error arose that depended sensitively on the distance between the pedestal and the center of the position-sensing optical trap. All the data presented in the remainder of this work were corrected by this means.

Localization of the pedestal's surface by thermal-noise imaging. Before assessing the diffusion coefficients near a pedestal, it was necessary to localize the pedestal's surface. We accomplished this by the super-resolution technique of thermal-noise imaging¹¹. The spatial probability density of a probe diffusing in a weak optical trap was a three-dimensional Gaussian distribution with an ovoid iso-probability surface (Fig. 2A). When a pedestal intersected the optical trap, a portion of its volume became inaccessible to the probe's diffusion: the forbidden volume in the probe's spatial probability density then provided a negative image of the pedestal (Fig. 2B). We computed a line profile along the x -axis through the probe's spatial probability density and converted the result by Boltzmann statistics to an energy landscape (Fig. 2E). We defined the wall of infinite energy as the impenetrable boundary of the pedestal and set $x=0$ at this location.

Diffusion was further restricted when the probe was attached to the pedestal by a short peptide that represented the concatenation of the two linkers used in an experiment to attach a PCDH15 monomer to the probe and pedestal (Fig. 2C). In an actual experiment, the monomer was attached at each end by one of the linker peptides (Fig. 2D). In both instances, the energy functions became steeper as the probe was confined both by the optical trap and by the tether (Fig. 2E). The slopes of the three energy functions defined the position-dependent forces exerted on the probe (Fig. 2F).

Determination of local diffusion constants. When a bead diffuses close to a boundary, its mean squared displacement becomes anisotropic and declines in comparison to that in bulk solution. Such hindered diffusion can be described by a position-dependent and anisotropic diffusion constant. Local diffusion constants have previously been measured by positioning an optically trapped bead at different distances from a boundary and computing the bead's mean squared displacement¹² or by inferring the diffusion coefficient from the power spectral density of the bead's motion^{13–15}. These methods average the diffusion coefficient's value over the spatial extent of the bead's diffusion in the relatively small volume of strong optical trapping. We instead confined a probe's motion by a weak optical trap within a larger trapping volume of 160 nm \times 140 nm \times 253 nm in respectively the x -, y -, and z -directions. The beam profile was Gaussian along each axis, and this volume represented three standard deviations in each direction from the center of the beam. We subdivided the trapping volume into voxels with edge lengths of 5 nm and computed the probe's mean squared displacement independently within each voxel for a time lag of 150 μs (Fig. 3A)^{16,17}. We then made use of the fact that, for each voxel, the slope relating the mean squared displacement along each axis to the time lag is twice the probe's local diffusion constant along that axis.

Our method constitutes a significant improvement in spatial resolution over previous approaches. Although those methods average over the entire trapping volume accessible to the bead's diffusion, typically on the order of 10 nm wide and 100 nm deep, we measured the diffusion constant in each 125 nm³ (5 nm \times 5 nm \times 5 nm) voxel within this volume. Such high spatial resolution is crucial for the constrained geometries in our single-molecule

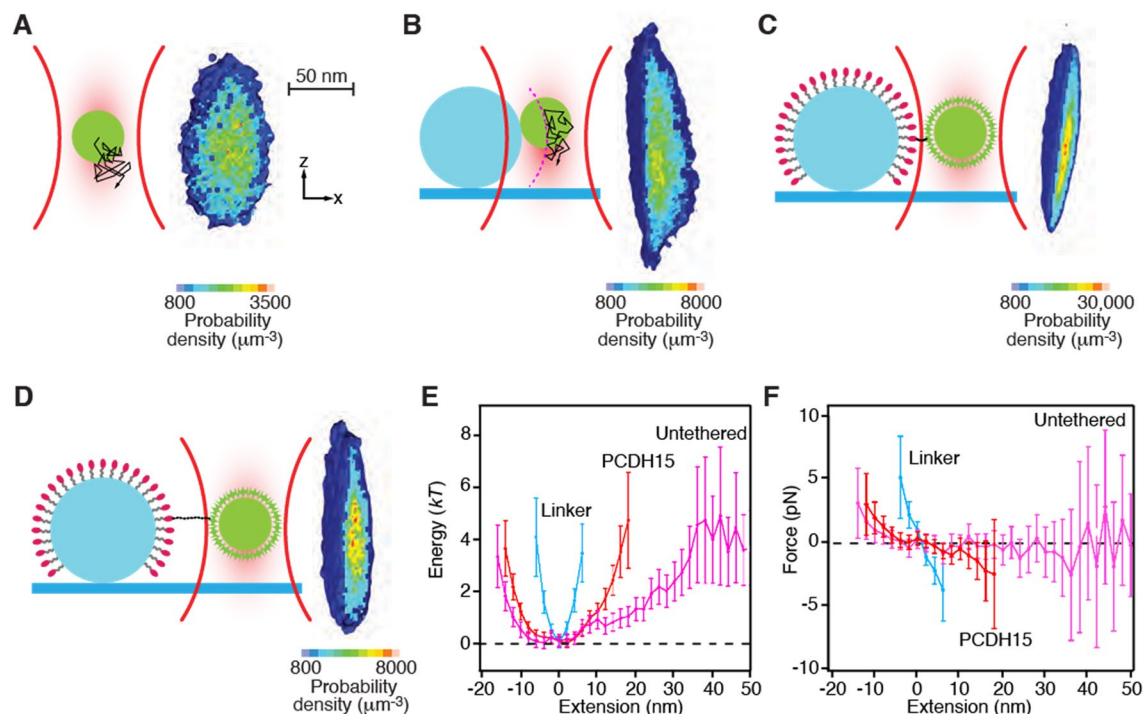


Figure 2. Determination of the pedestal's position and trap's strength. (A) A schematic diagram (left) portrays the thermal diffusion of the probe in an optical trap. A section through the experimentally measured three-dimensional probability density (right) reveals the positions explored by the diffusing probe. The distribution is roughly symmetrical along the x - and y -axes, but elongated owing to weaker trapping along the z -axis. Note the discrepancy in scale: the density distribution is magnified about 25X in comparison to the $1\ \mu\text{m}$ probe. The arrangements, definitions of axes, and spatial scales are identical in the following three panels. (B) When the probe is brought into contact with the fixed pedestal, its diffusion is restricted. Flattening of the experimental probability density demarcates the surface of the pedestal. (C) When the probe is affixed to the PEG-coated pedestal by a short linker, the linker further restricts diffusion of the probe. (D) In an actual experiment, the probe is attached to the pedestal by a PCDH15 monomer. The protein's extensibility allows the probe to explore a larger volume of space. (E) The experimentally determined probability distributions reflect the energy of the system for the probe at various positions. (F) The slopes of the displacement-energy relations in panel (E) represent the forces exerted on the probe by the optical trap and tethers. In both panels, the error bars show standard deviations calculated by means of correlated counting statistics²⁰, a technique used to estimate the errors for correlated datasets such as these. The occupancy counts range from 60 to 110 in the central regions of each dataset to one to three counts for the most extreme points.

experiments: our data clearly demonstrated that in close proximity to the coverslip and pedestal, the diffusion constant dramatically changed over the dimensions of the trapping volume. The spatial resolution of our technique was limited by the precision with which we could determine the probe bead's position, slightly below 1 nm along each axis, and by the duration of the diffusion measurement, for each voxel had to be visited sufficiently often to provide statistical significance. Although the resulting three-dimensional spatial map of diffusion constants was limited in spatial extent by the width of the trapping volume, larger volumes could be explored by displacing the optical trap in steps smaller than the width of the trapping volume and recording partially overlapping diffusion maps that were subsequently fused.

In our single-molecule assay of PCDH15 molecules, the protein was stretched along the x -axis. Because we were therefore mainly interested in how the associated diffusion constant D_x changed with extension from the pedestal, we moved the optical trap along that axis in 100 nm steps and determined the diffusion constant at each position (Fig. 3B). Although the focal spot of the optical trap remained fixed during each measurement, the trap was weak enough that the probe could diffuse along all three axes with respect to that point. We also computed the diffusion constants for motion along the y -axis, tangential to the pedestal but at a fixed height above the coverslip (D_y , Fig. 3C) as well as those along the z -axis, tangential to the pedestal but perpendicular to the coverslip (D_z , Fig. 3D). These results were determined for a probe maintained at a distance of 500 nm from the coverslip, so that the average z -position of the probe corresponded to the equator of the pedestal (Fig. 3E).

Assuming that the coverslip acted as an infinite wall to which the probe's diffusion coupled, we computed the diffusion constants expected in the absence of a pedestal for movements parallel and perpendicular to the coverslip as a function of the separation distance between the probe and coverslip. For positions far from the pedestal, we expected D_x and D_y —the diffusion constants parallel to the coverslip—to approximate the value computed by Faxen's law, which describes the diffusion constant of sphere at height h moving parallel to the surface of a wall¹⁸. In comparison, D_z —the diffusion constant normal to the coverslip—was predicted to follow Brenner's law^{18,19}, which describes the motion of a sphere moving perpendicularly above a plane. As expected,

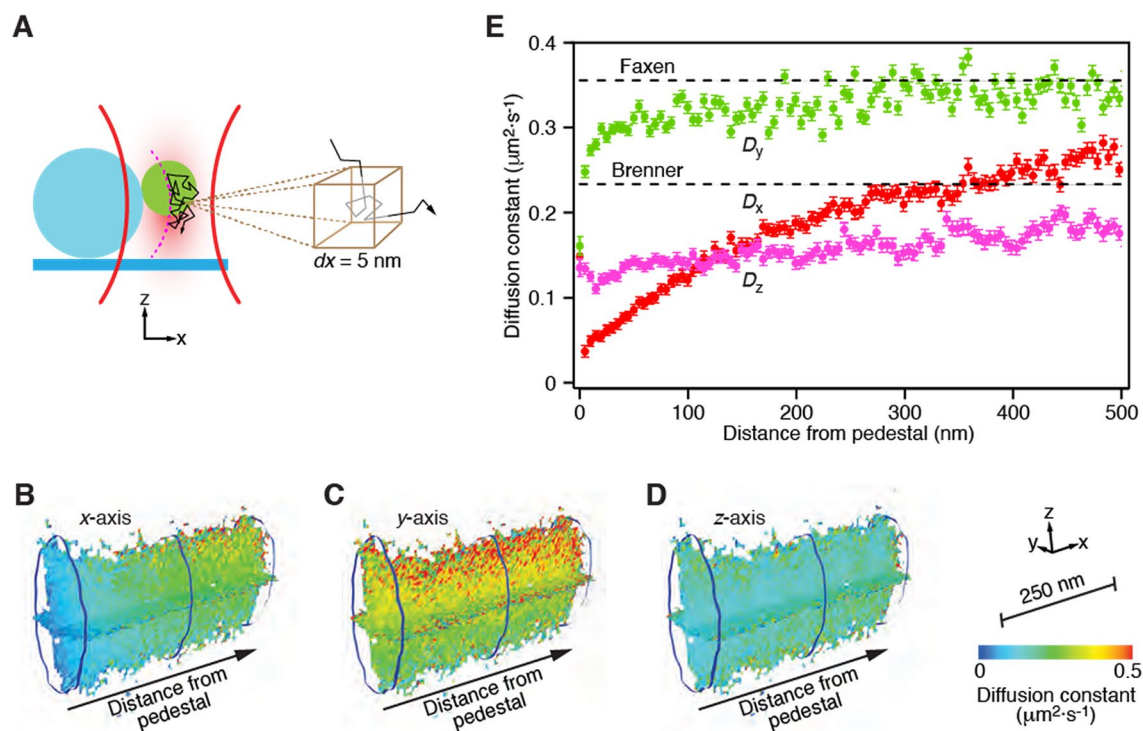


Figure 3. Measurement of local diffusion constants. (A) A schematic diagram depicts measurement of the mean squared displacement for a probe centered in a 5 nm voxel. (B) A heat map shows local diffusion constants along the x -axis as a function of the probe's position along each of the three indicated axes. The definition of axes, spatial scale, and calibration are shown at the bottom right of the figure and pertain to the next two panels as well. (C) Another map portrays the local diffusion constants along the y -axis. (D) A similar representation displays the local diffusion constants along the z -axis. (E) The local diffusion constants along the three axes display strikingly different behaviors. The values D_x for motion along the x -axis decrease sharply as the probe approaches the pedestal. Diffusion along the y -axis, parallel to the coverslip, yields values D_y relatively insensitive to position. The diffusion constants D_z for movement along the z -axis are reduced by proximity to the coverslip. These data are identical to those along the x -axes of the three preceding heat maps. The error bars represent weighted standard errors of the means.

the local diffusion constants progressively approached the analytical values with increasing distance between the probe and pedestal. The coupling of the probe's diffusion to the pedestal extended beyond 500 nm along the x -axis, well in excess of the two tangential couplings, 35 nm for the y -axis and 445 nm for the z -axis. The ranges of the coupling were determined by the distances at which the experimental values approached within 15% of the theoretical values. The diffusion constant along the x -axis declined by half upon extension from a separation distance of 50 nm to 200 nm, a range of particular interest for single-molecule experiments on the proteins that underlie auditory sensation.

Discussion

Precise characterization of the mechanical properties of a protein in a single-molecule experiment is dependent on accounting for factors that affect the measurements. In our experiments on the mechanical properties of PCDH15, a micrometer-sized probe serves as both a proxy for the position of the protein and the substrate through which forces are delivered to the protein. It is accordingly essential that measurements of the probe reflect the true mechanical response of the protein under study. The use of short, inelastic linkers reduces the filtering of the protein's instantaneous position. Even for relatively short linkers, however, accurately measuring the effect of force on a protein requires compensation for the proximity of the probe to the pedestal and coverslip.

The use of short linkers introduces the additional complication that proximity of the pedestal and coverslip distorts the position signal of the probe. Here we presented a technique to measure and compensate for the influence of the pedestal. The offset measurements obtained by this means recovered the position of a probe at a known displacement from the center of the position-sensing trap with minimal error. In addition to aiding the accurate measurement of anisotropic and position-dependent diffusion coefficients, this technique demonstrates that the benefit of short linkers in single-molecule experiments needs not be limited by optical interaction with the substrates.

We then characterized the diffusion coefficients near the coverslip and near the pedestal. Using these results, we could compensate for the restricted diffusion that the probe experiences. Our data show that the restricted diffusion of the probe when close to the pedestal is non-negligible in all directions. Of particular relevance to single-molecule experiments is the considerable restriction of diffusion along the x -axis, the direction of protein

extension. The reduced diffusion constants associated with such motions significantly filter the mechanical response of a protein. Moreover, the diffusion constant in the direction of extension changes substantially over the range of distances relevant to single-molecule experiments involving auditory proteins.

Voxel size contributed to the resolution of our measurements, for smaller voxels permitted a more granular mapping of the local diffusion constants. However, this benefit had to be balanced with the need to obtain sufficient data points from each voxel, the probability of which decreases as voxel size declines¹⁷. Another consideration for measurements of local diffusion constants was the choice of time lags at which to measure the mean squared displacement (Supplementary Information). This value plateaus beyond a characteristic autocorrelation time $\tau = \gamma / (2\kappa)$ as a result of the probe's confinement in the optical trap, resulting in a measured value smaller than that for a free particle. To capture the motion of the probe while it approximated free diffusion, the time lag accordingly had to be much smaller than this autocorrelation time.

A small time lag was also critical for another reason: the gradient force owing to the optical trap could result in drift. For a starting position far from the center of the trap, the gradient force causes the mean squared displacement to grow faster than free diffusion and therefore complicates measurements. The influences of the gradient force and of free diffusion can be compared by the relative mean-squared-displacement contribution¹⁷

$$RMSDC = \left(\frac{\kappa at}{\gamma} \right)^2 / (2Dt) = \kappa^2 a^2 t / (2\gamma k_B T) \quad (2)$$

in which κ is the spring constant of the optical trap along the relevant axis, a the displacement from the trap's center, t the time lag, γ the viscous drag coefficient of the probe given by Stokes' law, and D the local diffusion constant. k_B and T are respectively the Boltzmann constant and thermodynamic temperature. For the ratio to remain small such that essentially free diffusion occurs, the time lag had to be much smaller than the characteristic drift time $\tau_D = (2\gamma k_B T) / (\kappa^2 a^2)$. Combining the two effects of optical trapping, the minimum of τ and τ_D determines the timescale at which the probe's motion deviated from free diffusion. If $\tau < \tau_D$, as was the case in our system for excursions of less than 150 nm from the trap's center along any axis, then the influence of the gradient force on the mean squared displacement was negligible. If instead $\tau > \tau_D$, then the measured value would have exceeded that of a freely diffusing particle for intermediate time lags.

Methods

The Supplementary Information for this article includes detailed descriptions of the experimental apparatus and optical system. In brief, the photonic-force microscope was capable of measuring the position of a micrometer-sized probe bead with sub-nanometer precision for an integration time of 1 μ s and sampling at 10^5 s⁻¹. A weak optical trap was formed within the sample chamber by focusing a 1064 nm laser beam with a high-numerical-aperture water-immersion objective lens.

The three-dimensional position of the probe confined within the weak optical trap was obtained from the interference on a quadrant photodiode of light scattered forward from the probe with unscattered light. To hold the probe at a constant displacement from the center of weak optical trap, as was required for the correction owing to the pedestal, an optical trap was formed by an 852 nm laser. The position of this relatively strong optical trap with respect to the weak trap was adjusted by means of a beam-steering lens in the beam path of the strong laser.

Received: 2 July 2020; Accepted: 4 January 2021

Published online: 26 January 2021

References

- Gebhardt, J. C. M., Bornschlöggl, T. & Rief, M. Full distance-resolved folding energy landscape of one single protein molecule. *Proc. Natl. Acad. Sci.* **107**, 2013–2018 (2010).
- Cecconi, C. Direct observation of the three-state folding of a single protein molecule. *Science* **309**, 2057–2060 (2005).
- Pfytzner, E. *et al.* Rigid DNA beams for high-resolution single-molecule mechanics. *Angew. Chem. Int. Ed.* **52**, 7766–7771 (2013).
- Bartsch, T. F. *et al.* Elasticity of individual protocadherin 15 molecules implicates tip links as the gating springs for hearing. *Proc. Natl. Acad. Sci. USA* **116**, 11048–11056 (2019).
- Leake, M. C., Wilson, D., Gautel, M. & Simmons, R. M. The elasticity of single titin molecules using a two-bead optical tweezers assay. *Biophys. J.* **87**, 1112–1135 (2004).
- Jeney, S., Stelzer, E. H. K., Grubmüller, H. & Florin, E.-L. Mechanical properties of single motor molecules studied by three-dimensional thermal force probing in optical tweezers. *ChemPhysChem* **5**, 1150–1158 (2004).
- Lee, G. *et al.* Nanospring behaviour of ankyrin repeats. *Nature* **440**, 246–249 (2006).
- Pralle, A., Prummer, M., Florin, E. L., Stelzer, E. H. & Hörber, J. K. Three-dimensional high-resolution particle tracking for optical tweezers by forward scattered light. *Microsc. Res. Tech.* **44**, 378–386 (1999).
- Bartsch, T. F., Kochanzyk, M. D., Lissek, E. N., Lange, J. R. & Florin, E.-L. Nanoscopic imaging of thick heterogeneous soft-matter structures in aqueous solution. *Nat. Commun.* **7**, 1–9 (2016).
- Seitz, P. C., Stelzer, E. H. K. & Rohrbach, A. Interferometric tracking of optically trapped probes behind structured surfaces: A phase correction method. *Appl. Opt.* **45**, 7309 (2006).
- Bartsch, T. F. *et al.* Detecting sequential bond formation using three-dimensional thermal fluctuation analysis. *ChemPhysChem* **10**, 1541–1547 (2009).
- Pralle, A., Florin, E.-L., Stelzer, E. H. K. & Hörber, J. K. H. Local viscosity probed by photonic force microscopy. *Appl. Phys. Mater. Sci. Process.* **66**, S71–S73 (1998).
- Jannasch, A., Mahamdeh, M. & Schäffer, E. Inertial effects of a small brownian particle cause a colored power spectral density of thermal noise. *Phys. Rev. Lett.* **107**, 228301 (2011).
- Franosch, T. *et al.* Resonances arising from hydrodynamic memory in Brownian motion. *Nature* **478**, 85–88 (2011).

15. Schäffer, E., Nørrelykke, S. F. & Howard, J. Surface forces and drag coefficients of microspheres near a plane surface measured with optical tweezers. *Langmuir* **23**, 3654–3665 (2007).
16. Hsu, Y.-H. & Pralle, A. Note: Three-dimensional linearization of optical trap position detection for precise high speed diffusion measurements. *Rev. Sci. Instrum.* **85**, 076106 (2014).
17. Tischer, C., Pralle, A. & Florin, E.-L. Determination and correction of position detection nonlinearity in single particle tracking and three-dimensional scanning probe microscopy. *Microsc. Microanal.* **10**, 425–434 (2004).
18. Chio, C. C. & Tse, Y.-L.S. Hindered diffusion near fluid-solid interfaces: Comparison of molecular dynamics to continuum hydrodynamics. *Langmuir* **36**, 9412–9423 (2020).
19. Happel, J. & Brenner, H. *Low Reynolds Number Hydrodynamics* Vol. 1 (Springer, Dordrecht, 1981).
20. Straatsma, T. P., Berendsen, H. J. C. & Stam, A. J. Estimation of statistical errors in molecular simulation calculations. *Mol. Phys.* **57**, 89–95 (1986).

Acknowledgements

TFB was supported by a Junior Fellow award from the Simons Foundation and CMV by MSTP Grant T32GM007739 from the NIH. AT and DMF were supported by the F. M. Kirby Foundation. FEH received a Studienstiftung des Deutschen Volkes and AO a Medical Research Fellows Program grant from Howard Hughes Medical Institute, of which AJH is an Investigator.

Author contributions

T.F.B., C.M.V., F.E.H., A.T., and A.O. designed and conducted the experiments; T.F.B., C.M.V., F.E.H., A.T., D.M.F., and A.O. analyzed the data; T.F.B., C.M.V., F.E.H., A.T., D.M.F., A.O., and A.J.H. wrote the paper.

Competing interests

The authors declare no competing interests.

Additional information

Supplementary Information The online version contains supplementary material available at <https://doi.org/10.1038/s41598-021-81593-x>.

Correspondence and requests for materials should be addressed to T.F.B. or A.J.H.

Reprints and permissions information is available at www.nature.com/reprints.

Publisher's note Springer Nature remains neutral with regard to jurisdictional claims in published maps and institutional affiliations.



Open Access This article is licensed under a Creative Commons Attribution 4.0 International License, which permits use, sharing, adaptation, distribution and reproduction in any medium or format, as long as you give appropriate credit to the original author(s) and the source, provide a link to the Creative Commons licence, and indicate if changes were made. The images or other third party material in this article are included in the article's Creative Commons licence, unless indicated otherwise in a credit line to the material. If material is not included in the article's Creative Commons licence and your intended use is not permitted by statutory regulation or exceeds the permitted use, you will need to obtain permission directly from the copyright holder. To view a copy of this licence, visit <http://creativecommons.org/licenses/by/4.0/>.

© The Author(s) 2021

Nanomechanics of wild-type and mutant dimers of the tip-link protein protocadherin 15

Camila M. Villasante¹, Xinyue Deng¹, Joel E. Cohen^{2,3,4}, and A. J. Hudspeth^{1,5}

¹Laboratory of Sensory Neuroscience, The Rockefeller University, New York, NY 10065 USA;

²Laboratory of Populations, The Rockefeller University, New York, NY 10065 USA; ³Earth Institute and Department of Statistics, Columbia University, New York, NY 10027 USA;

⁴Department of Statistics, University of Chicago, Chicago, IL 60637 USA; ⁵Howard Hughes Medical Institute, The Rockefeller University, New York, NY 10065 USA

Abstract

Mechanical force controls the opening and closing of mechanosensitive ion channels atop the hair bundles of the inner ear. The filamentous tip link connecting transduction channels to the tallest neighboring stereocilium modulates the force transmitted to the channels and thus changes their probability of opening. Each tip link comprises four molecules: a dimer of protocadherin 15 and a dimer of cadherin 23, all of which are stabilized by Ca²⁺ binding. Using a high-speed optical trap to examine dimeric PCDH15, we find that the protein's configuration is sensitive to Ca²⁺ and that the molecule exhibits limited unfolding at a physiological Ca²⁺ concentration. PCDH15 can therefore modulate its stiffness without undergoing large unfolding events in physiological Ca²⁺ conditions. The experimentally determined stiffness of PCDH15 accords with published values for the stiffness of the gating spring, the mechanical element that controls the opening of mechanotransduction channels. When PCDH15 has a point mutation, V507D, associated with non-syndromic hearing loss, unfolding events occur more frequently under tension and refolding events occur less often than in the wild-type protein. Our results suggest that the maintenance of appropriate tension in the gating spring is critical to the appropriate transmission of force to transduction channels, and hence to hearing.

Introduction

The transformation of sound waves into neural signals, a process known as mechano-electrical transduction, occurs in the cochlea of the internal ear. To allow humans to hear with the range and precision that we do, this process must be both sensitive and adaptive. The apical surface of each hair cell bears actin-filled stereocilia arranged in order of height. Each stereocilium is connected by a filamentous tip link to its tallest neighbor¹. When the hair bundle is deflected towards its tall edge by a sound stimulus, the stereocilia pivot and tense the gating springs that control the opening of the mechano-electrical transduction channels atop each stereocilium. When sufficient tension has been conveyed, the channels open and allow cations within the endolymphatic fluid surrounding the hair bundles to flow into the cells and transduction to occur² (Figure 1A).

It is plausible that the gating springs are the filamentous tip links that connect the transduction channels of a stereocilium to its tallest neighbor. Each tip link comprises four protein molecules³: a dimer of protocadherin 15 (PCDH15) and a dimer of cadherin 23 (CDH23). Because abolishing the tip links halts mechanotransduction⁴ whereas allowing the tip links to regenerate restores sensitivity⁵, the tip link—or the attachments at its two ends—likely controls the opening and closing of the channels and serves as the gating spring. Moreover, the hundreds of mutations in tip-link proteins that result in human hearing loss^{6–10} underscore the role of the tip link in hearing.

The direct association of PCDH15 with the transduction-channel complex by way of its transmembrane and cytoplasmic domains¹¹ implicates the protein in channel gating. PCDH15 comprises 11 extracellular cadherin (EC) domains and a protocadherin 15-interacting, channel-associated (PICA) domain, also known as MAD12¹² or EL¹¹ (Figure 1B). The EC domains, which are composed of Greek key motifs, are similar in their folding patterns (Figure 1C). The intervening linker regions can bind up to three Ca²⁺ ions¹² and stabilize the entire molecule against unfolding by force¹³. The concentration of Ca²⁺ in the cochlear endolymph is approximately 20 μM, a value much lower than that in the rest of the body¹⁴. The dissociation constant of Ca²⁺ at the linker regions lies in the range of tens to hundreds of micromolar¹², a

range that might confer additional modulation of PCDH15 behavior at physiological Ca^{2+} concentrations.

Depending on the local characteristic frequency and whether measured in inner or outer hair cells, the enthalpic stiffness of gating springs in the rat's cochlea¹⁵ lies between $0.5 \text{ mN}\cdot\text{m}^{-1}$ and $4 \text{ mN}\cdot\text{m}^{-1}$. Although monomers of PCDH15 have an enthalpic stiffness of approximately $10 \text{ mN}\cdot\text{m}^{-1}$, the measured stiffness of monomeric PCDH15 is lower over the physiological range of forces¹⁶. This softening represents the contribution of entropic elasticity, which stems from the extension of the interdomain linker regions, the EC domains themselves, and any unfolded portions of the molecules. We asked here whether dimeric PCDH15 would exhibit a similar softening over the physiological range of forces and whether its enthalpic stiffness would accord with that of the gating spring. To understand whether PCDH15 has the appropriate properties to be a component of the gating spring, we measured its stiffness, inquired what factors control its mechanical responses, and examined how it softens under force.

Results

Experimental conditions

To probe the mechanical properties of PCDH15 directly, we used an optical trap with sub-nanometer spatial resolution and microsecond temporal resolution^{16,17} (Figure 1D). In a typical experiment, PCDH15 was tethered between two beads: at its carboxy terminal it was attached by a SpyTag-SpyCatcher bond¹⁸ to a pedestal bead covalently attached to a glass coverslip, and at its amino terminal it was linked thorough a biotin-streptavidin interaction to a probe bead in solution. The anchors that attached PCDH15 to the beads on either end were separated from the protein by short, unstructured peptides. Two lasers acted on the probe bead: a highly stable 1064 nm position-sensing laser, which detected the three-dimensional position of the probe bead and thus the extension of the construct, and an 852 nm force-producing laser, which exerted force on the probe bead and therefore on the protein.

To explore the range of physiological forces that PCDH15 experiences in the ear¹⁹, we conducted force-ramp experiments in which force was increased at a constant rate from a resting level of 1 pN and then decreased at the same rate to a resting level of 1 pN, where it was held for 2 s before the next cycle. During these extension-relaxation cycles, the protein sometimes underwent conformational changes. Such unfolding events could be seen as steps in the end-to-end distance (Figure 1F). After a force-ramp cycle had been repeated up to hundreds of times on a single protein molecule, all the cycles could be displayed as a heatmap in which lighter colors correspond to more frequently occupied states and darker colors represent trajectories that occurred only once or infrequently (Figure 1G).

Because of the importance of Ca^{2+} to the structure of PCDH15, we performed our experiments at three representative Ca^{2+} concentrations: 3 mM, a saturating level meant to populate all the Ca^{2+} -binding sites; 20 μM , a physiological concentration in the mammalian cochlea^{20–22}; and with no Ca^{2+} , but in the presence of the Ca^{2+} chelator EDTA. Previous studies on monomeric PCDH15 showed that its mechanical behavior changes with the Ca^{2+} concentration¹⁶, so we explored whether the dimer shows a similar Ca^{2+} dependence.

Ca^{2+} sensitivity of PCDH15 under physiological forces

PCDH15 naturally dimerizes at EC3 and the PICA domain²³. To ensure that force was distributed equally to both strands of each PCDH15 dimer, we devised a construct in which the monomers are attached to one another at each end by paired disulfide bonds derived from the Fc hinge region of human immunoglobulin²⁴ (Figure 1E). This study used murine PCDH15, which has high sequence homology²⁵ to human PCDH15.

As exhibited both by a representative cycle (Figure 2A) and by the single bright branch on a representative heatmap (Figure 2B), dimeric PCDH15 underwent little unfolding at a saturating level of Ca^{2+} . At low forces, PCDH15 extended easily in response to applied force, a behavior that reflects entropic elasticity owing to the straightening of the molecule's thermal undulations. At higher forces, after most entropic degrees of freedom had been pulled out, the

relationship between the end-to-end distance and the applied force became nearly linear. The remaining extensibility resulted from the enthalpic or Hookean stiffness of PCDH15.

To quantify and classify the unfolding changes that occurred, we used a saturation model augmented with a linear-spring term: if x is the end-to-end distance of the PCDH15 construct,

$$x = \frac{x_E}{1 + \frac{F_{HALF}}{F}} + \frac{F}{K} \quad (1)$$

The maximal entropic extension of PCDH15 is given by x_E ; F_{HALF} is the force at which entropic extension is halfway complete. The contribution of enthalpic stiffness is given by the second term, the extension of a linear spring of stiffness K under force F . The value of K was determined by averaging the inverse spatial derivatives at forces exceeding 30 pN for every cycle of all data sets at each Ca^{2+} concentration.

At a saturating concentration of Ca^{2+} , 3 mM, few discrete unfolding events occurred, and their magnitudes were relatively small. The frequency distribution of the size of these unfolding events was bimodal with peaks at 2.0 nm and 6.6 nm (Figure S6). We asked whether these individual unfolding events happened in succession within the same cycle, which would suggest the occurrence of a larger unfolding event through a multi-step process. We summed the total unfolding lengths in the extension phase of each cycle, during which the majority of unfolding events occurred. The total unfolding length per cycle was predominantly below 20 nm, with a bimodal frequency distribution peaking at 1.8 nm and 6.3 nm (Figure 2C). These events could correspond to unfolding of the inter-domain linker regions, which—because they lack secondary structure—are likely to be the first components of PCDH15 to unfold under force. Individual linker regions would give rise to an additional length between 1 nm and 2 nm when extended, so it is plausible that the unfolding of linker regions yielded the unfolding events that we observed. Furthermore, not all the linker regions bind three ions of Ca^{2+} —some bind none whereas others bind one or two ions¹²—so we might have observed extension of these linker regions even at a saturating level of Ca^{2+} . It is also possible that the small extensions reflected the straightening of the kinked EC9-10 linker^{12,26}, which does not bind Ca^{2+} and could extend up to 4 nm. We also asked whether there was any relationship between the size of individual unfolding events and the force at which they occurred. We found that unfolding events around the 2.0 nm and 6.6 nm

frequency peaks occurred more often at forces between 10 pN and 20 pN than at forces below and above this interval (Figure 2D).

PCDH15 also unfolded infrequently at a physiological Ca^{2+} concentration of 20 μM . Nevertheless, at that concentration PCDH15 was strikingly more extensible than at a saturating level of Ca^{2+} (Figure 2E,F). In other words, despite the scarcity of unfolding events, the dimer was softer at the lower concentration of Ca^{2+} . This finding was surprising, for we had expected an increase in compliance to emerge through more frequent unfolding events. This observation might reflect the differential Ca^{2+} -binding behaviors of the linker regions in PCDH15: the heterogeneity in the linkers, combined with the relatively low physiological concentration of Ca^{2+} and the binding affinity for Ca^{2+} , might result in the overall softening. As was observed at a saturating Ca^{2+} concentration, the frequency distribution of total unfolding length per cycle was bimodal with peaks at 4.5 nm and 11.5 nm (Figure 2G). These values were similar in magnitude to the peaks of total unfolding length per cycle that we observed at a saturating level of Ca^{2+} . It was not possible to discern the origin of these classes of unfolding events owing to the repetitive structure of PCDH15. However, from the magnitudes of the conformational changes and assuming a length of 0.40 nm per amino acid²⁷, we conjecture that these two classes arose from the inter-domain linker regions of PCDH15 that, when unfolded, would have given rise to 16 nm of additional length. The individual unfolding events were again distributed across a range of forces (Figure 2H). These results suggest that, at saturating and physiological Ca^{2+} conditions, unfolding of the linkers confers flexibility to PCDH15 and modulates its stiffness.

In the absence of Ca^{2+} , PCDH15 underwent many types of unfolding that can be seen both in individual cycles and in numerous highly occupied branches on the heatmap (Figure 2I,J). There were far more unfolding events than were observed at higher Ca^{2+} concentrations. The sum of the lengths of unfolding events per cycle, although peaking in frequency at 23.3 nm (Figure 2K), reached values above 100 nm. We would expect the unfolding of a full-length cadherin domain to extend the end-to-end length of PCDH15 by 33 nm to 45 nm, depending on the particular domain²⁸ that unfolded, and assuming a length of 0.40 nm per amino acid²⁹ less 4.5 nm to account for the loss of the folded domain³⁰. Because we do not observe a

clear peak in that range, we infer that the unfolding of full domains was not the primary response to applied force. The length of unfolding at peak frequency that we observed could correspond to partial domain unfolding: if the A and B strands of an individual EC domain were to come undone, the end-to-end distance would increase by approximately 17 nm. The individual unfolding events occurred over a range of forces, with no clear relationship between the size of the unfolding event and the force at which it occurred (Figure 2L). This result is surprising, because we had expected to see more frequent domain unfolding in the absence of Ca^{2+} , but our results suggest that an alternative mechanism is in play.

Effects of a hearing-loss mutation on PCDH15

Numerous mutations in the tip link result in hearing loss^{6,7,10,31}. Such mutations can cause either syndromic deafness, in which deafness is accompanied by other deficits such as blindness or vestibular dysfunction, or non-syndromic deafness, which involves exclusively hearing loss. Though PCDH15 is present in the retina and vestibular labyrinth as well as the cochlea, individuals with non-syndromic deafness retain normal retinal and vestibular function: only their hearing is affected, which raises interesting questions about the pathophysiology of these mutations.

We sought to understand how a deafness-causing mutation affects the mechanics of PCDH15. We chose to study V507D, the murine homolog of the human V528D variant that is associated in humans with non-syndromic, autosomal, recessive deafness type 23 (DFNB23)³¹. This point mutation of a highly conserved valine in EC5 was identified in a Newfoundland family whose members exhibit prelingual hearing loss. The V507 residue occurs in the β -sheet of the B strand of EC5 (Figure 1E), which is not a site of dimerization, nor part of the handshake interaction with CDH23, nor part of the Ca^{2+} -binding sites, any of which would result in obvious disruptions of tip link integrity. We then predicted the structures of wild-type and V507D EC5 domains using AlphaFold2 Colab³²⁻³⁶. Alignment of the crystal structure and AlphaFold2-predicted wild-type EC5 showed that the prediction was highly accurate (Figure S4A). The predicted structure of V507D EC5 indicates that the β -sheet structure of the B strand would be

disrupted by the substituted negatively charged aspartic acid residue (Figure S4B,C). This alteration could result in an easier unfolding of strands A and B, which in the native protein are stabilized by a parallel β -sheet interaction between the A and G strands and a stronger anti-parallel β -sheet interaction between the B and E strands (Figure 1C). Disruption of the β -sheet interaction of strands B and E could therefore cause an instability of strands A and B. We conjecture that the change of this hydrophobic valine to a negatively charged aspartic acid weakens the force-bearing ability of the β -sheet and thus compromises the structural integrity of EC5. Furthermore, the EC5-6 linker region binds only one Ca^{2+} ion, which might predispose EC5 to unfolding.

As the concentration of Ca^{2+} decreased from saturating to absent, PCDH15 V507D exhibited a striking pattern of increasing dysregulation. At a high Ca^{2+} concentration of 3 mM, and in contradistinction to the wild-type dimer, there were two populations of V507D molecules. Some V507D molecules appeared to behave more like wild-type PCDH15 at the same saturating level of Ca^{2+} , with the minimal unfolding observed in individual cycles reflected by the single bright branch on the heatmap (Figure S5A,B). Other V507D molecules exhibited more unfolding during individual cycles, revealed by multiple bright branches on the heatmap (Figure 3A,B). We included both kinds of force-extension trajectories in further analysis, for the tethering statistics (see Supplementary Information) gave us confidence that individual trajectories corresponded to individual molecules rather than multiple tethers, and we observed both kinds of trajectories often enough to deem them significant.

Considering both populations, we observed many more unfolding events per cycle from V507D than from wild-type PCDH15 at the same saturating concentration of Ca^{2+} , for which we largely observed only small unfolding events below 10 nm in magnitude. Because the numerous unfolding events in the mutant protein occurred at a Ca^{2+} level likely to saturate Ca^{2+} binding sites in the inter-domain linker regions, they likely stemmed from instability in EC5, where the mutated residue was located. The frequency of total unfolding length per cycle peaked at 8.8 nm, 50.0 nm, and 66.3 nm (Figure 3C). The 50.0 nm unfolding events exceeded the size expected for the unfolding of an entire EC domain or the PICA domain, 33-45 nm, but are smaller than

expected for the unfolding of two domains. This suggests that some intermediate unfolding event gave rise to this class. The 66.3 nm class of events might reflect the unfolding of two domains, which would yield an end-to-end distance increase of 66-90 nm. Many unfolding events occurred around 30 pN (Figure 3D), suggesting that V507D has a diminished ability to resist applied force compared to the wild-type protein, which has a more uniform distribution of unfolding forces.

At a physiological Ca^{2+} concentration of 20 μM , PCDH15 V507D again underwent unfolding events of varying magnitudes (Figure 3E,F). This behavior contrasted with that of the native protein at the same physiological Ca^{2+} concentration, for which very few, small unfolding events were seen. The frequency distribution of total unfolding length within each cycle peaked at 14.2 nm, 27.3 nm, and 39.4 nm (Figure 3G). As the location of the mutation, EC5 is the domain of V507D most likely to unfold. If EC5 and its neighboring linker regions were to unfold, we would expect an increase in end-to-end distance of 39.1 nm. The class at 39.4 nm therefore might well correspond to the unfolding of EC5. It is unclear what gave rise to the smaller classes of unfolding events, though unfolding of the linker regions, which would result in a total 16 nm increase in end-to-end distance, could contribute. Although we predicted that V507D would be more unstable and exhibit more unfolding at this level of Ca^{2+} , the unfolding lengths did not reach such high magnitudes as at a saturating Ca^{2+} concentration. This result suggests that V507D was extended more than the wild-type protein prior to the application of force (Figure S13D). The partial unfolding at baseline means that the unfolding we observed after applying force occurs in addition to the baseline unfolding, which explains the unexpected difference in unfolding range between physiological and saturating levels of Ca^{2+} (Figure 3H).

Like the wild-type dimer, V507D underwent numerous unfolding events in the absence of Ca^{2+} as evidenced by the illustrative cycle and multiple bright branches on the illustrative heat map (Figure 3I,J). However, the bright branch closest to the origin—which reflects the extension of the protein in the absence of any unfolding events—extended to approximately 100 nm at the highest applied forces, whereas for the wild-type protein this branch reached only 50 nm. In addition, the largest end-to-end distances achieved for V507D exceeded 200 nm, a distance greater than the 125 nm characteristic of the wild-type molecule. In many individual cycles we

did not observe drastic unfolding events (Figure 3I). Instead, the molecule appeared quite extended at baseline and lengthened easily with the application of force. This result suggests that the protein was already unfolded, or misfolded, at this concentration of Ca^{2+} even in the absence of force.

In the absence of Ca^{2+} , although sometimes as much as 150 nm unfolded in a single cycle for V507D, the total unfolding length varied widely and the frequency peaked at 49.3 nm (Figure 3K). The average total unfolding per cycle suggests that at least one full domain unfolded during the extension phase of a cycle. At this concentration, we were likely observing unfolding events similar to those at the higher levels of Ca^{2+} , along with additional events stemming from the complete lack of Ca^{2+} binding at the linker regions. There was again no clear relationship between size of unfolding events and the force at which they occurred, but many unfolding events of different sizes occurred around 30 pN (Figure 3L). Although by these metrics the behavior of V507D in the absence of Ca^{2+} resembled that at higher concentrations of Ca^{2+} , the end-to-end distance range of the protein exceeded that at other levels of Ca^{2+} . This result suggests that, in the absence of Ca^{2+} , V507D did not fold properly even at low resting forces but was already extended at the resting force of 1 pN. Because V507D displayed behavior that was not entirely captured by our modeling approach, we next sought a method of classifying the extension patterns across different experimental conditions.

Clustering of data by conformational state

To understand PCDH15 in various concentrations of Ca^{2+} with or without the V507D mutation, we analyzed all results from each construct and condition. The data fell into six classes, which we term "states" because, we believe, they represent different conformations of PCDH15 (Figure 4A). The defining characteristics of each state are the average value of its x_E parameter and the difference between that value and those of the contiguous states (Figure 4B). Notwithstanding the substantial overlap in x_E values of trajectories that we classify as belonging to different states, the average x_E values clearly differ. For example, the difference between the average x_E values for the first two states is 12.5 ± 0.3 nm (mean \pm SEM, $n = 2314$ trajectories

for state 1; $n = 1826$ trajectories for state 2), a distance consistent with the range of unfolding expected from the inter-domain linker regions. Because the difference between states 1 and 2 is smaller than what we would expect for unfolding of an entire EC cadherin, we call states 1 and 2 the folded states—that is, the states in which all EC domains and the PICA domain apparently remain folded. The differences between states 2 and 3 and between states 3 and 4 are respectively 29.9 ± 0.7 nm (mean \pm SEM, $n = 1372$ trajectories for state 3) and 30.0 ± 1.3 nm (mean \pm SEM, $n = 692$ trajectories for state 4), values consistent with the expectation for unfolding of a complete EC or PICA domain. The difference between states 4 and 5 is 17.6 ± 2.0 nm (mean \pm SEM, $n = 585$ trajectories for state 5), a value that does not accord with unfolding of a whole domain but might represent partial unfolding of a domain. Finally, the difference between states 5 and 6 is 72.2 ± 6.0 nm (mean \pm SEM, $n = 123$ trajectories for state 6), a value similar to that expected for the unfolding of two entire EC or PICA domains.

To understand the effect of the Ca^{2+} concentration and V507D mutation on how PCDH15 traversed the accessible state space, we segmented a molecule's trajectory during each cycle by the conformational changes that occurred and assigned each segment to a state through k -nearest-neighbor classification ($k = 3$; see Supplementary Information for details). To generate transition maps for each construct and condition, we analyzed the percentage of time that the molecule spent in each state and examined the states visited by subsequent segments within one cycle. In saturating Ca^{2+} conditions, the wild-type protein remained predominantly within state 1, with a few visits to state 2 (Figures 4C, S11A, S12A). At a physiological Ca^{2+} concentration, the native dimer spent much more time in state 2 and occasionally visited state 3, a behavior suggestive of unfolding of linker regions and one EC or PICA domain (Figures 4D, S11C, S12A). In the absence of Ca^{2+} , the wild-type dimer progressed up to state 5, with cycles beginning primarily in state 2 or above rather than in state 1 (Figures 4E, S11E, S12A). Under this condition, entire EC domains were likely unfolding.

In contrast to the wild-type dimer in saturating Ca^{2+} conditions, V507D at the same saturating level reached state 5 (Figures 4F, S11B, S12B). At a physiological Ca^{2+} level, V507D

visited up to state 5 and exhibited transition behaviors similar to those in the saturating Ca^{2+} condition (Figures 4G, S11D, S12B). In the absence of Ca^{2+} , V507D spent little time in states 1 and 2 and frequently started in higher states (Figures 4H, S11F, S12B), such as state 3, in which one EC domain was apparently already unfolded. The V507D dimer in the absence of Ca^{2+} favored higher states, unlike the wild-type protein at any Ca^{2+} concentration or V507D at greater Ca^{2+} concentrations. These results suggest that V507D had up to four unfolded EC domains in the absence of Ca^{2+} . For both the native dimer and V507D, as the Ca^{2+} concentration decreased, the state space explored by the protein increased, as expected from the stabilizing effect of Ca^{2+} .

Effect of Ca^{2+} concentration on refolding

At the start of a force-ramp cycle after a large unfolding event, the protein sometimes did not return to the starting position that it had occupied at the outset of the previous cycle: the protein either did not refold at all or refolded only partially within the 2 s inter-cycle resting period. To discern any patterns in the refolding ability of PCDH15 for each construct and Ca^{2+} concentration, we compared the highest state accessed in each cycle with the state of the first segment of the subsequent cycle. If the first segment of the next cycle was in state 1 or 2, we considered this cycle to be a full refolding because the average x_E values in states 1 or 2 were not consistent with the complete unfolding of any EC or PICA domain. We then analyzed the percentage of cycles with full refolding across all Ca^{2+} concentrations.

For the wild-type protein, we found that at a saturating level of Ca^{2+} PCDH15 never unfolded beyond state 2, so we obtained no refolding data for this condition. At a physiological Ca^{2+} concentration, PCDH15 refolded back to state 1 or 2 in 84.2 ± 15.8 % (mean \pm SEM, $N = 4$ datasets) of the instances. In the absence of Ca^{2+} , however, PCDH15 refolded back to state 1 or 2 only 62.9 ± 10.5 % ($N = 6$ datasets) of the time (Table 1).

In the V507D mutant at a saturating level of Ca^{2+} , PCDH15 fully refolded on 82.2 ± 5.7 % ($N = 24$ datasets) of the occasions. At a physiological level of Ca^{2+} this value decreased to 59.3 ± 8.0 % ($N = 16$ datasets) in stark contrast with the wild-type protein, for which refolding to state 1 or 2 occurred in most instances at the same concentration of Ca^{2+} . Finally, in the absence

of Ca^{2+} , PCDH15 V507D refolded to state 1 or state 2 in only $24.0 \pm 16.2\%$ ($N = 4$ datasets) of the cases, which signified a severe reduction in refolding ability compared to the native protein. The differences in refolding rates between wild-type and V507D dimers suggest that the point mutation disrupts the refolding ability of PCDH15. V507D dimers unfolded more often than wild-type dimers and refolded properly less often.

Linear stiffness of PCDH15

We calculated the enthalpic stiffness for PCDH15 and PCDH15 V507D by finding the inverse spatial derivative of each cycle in the high force regime—above 30 pN, the force at which the relationship between force and extension became essentially linear—and averaging the values across all data for each Ca^{2+} condition. In 587 determinations at physiological Ca^{2+} levels, PCDH15 had an enthalpic stiffness of $6.4 \pm 0.4 \text{ mN}\cdot\text{m}^{-1}$. If we assume that CDH23, which is approximately 2.3 times as long as PCDH15, has mechanical properties similar to those of PCDH15, its stiffness would be about $2.8 \text{ mN}\cdot\text{m}^{-1}$. For both proteins in series, the stiffness K_{TL} of the tip link can then be calculated:

$$\frac{1}{K_{TL}} = \frac{1}{K_{PCDH15}} + \frac{1}{K_{CDH23}}. \quad (2)$$

Using the values above, the enthalpic stiffness of the entire tip link in a normal animal is expected to be about $1.9 \text{ mN}\cdot\text{m}^{-1}$. Measurements have shown the stiffness of the gating spring to be between $0.5 \text{ mN}\cdot\text{m}^{-1}$ and $4 \text{ mN}\cdot\text{m}^{-1}$, depending on the characteristic frequency along the cochlea¹⁵, so our value for the enthalpic stiffness of PCDH15 lies within the expected stiffness range of the gating spring. Furthermore, the entropic stiffness of each state is less than the calculated enthalpic stiffness (Figure 5), which implies that PCDH15 is softer over the range of physiological forces than previously thought. Because the entropic stiffness of each state is lower than the calculated enthalpic stiffness, entropic elasticity is responsible for most of the mechanical response of PCDH15 over the range of physiological forces.

Discussion

Our findings indicate that PCDH15, in the dimeric form in which it exists within the cochlea, has the appropriate mechanical properties to serve as a portion of the gating spring. Further, at the physiological Ca^{2+} concentration and over the relevant force range, unfolding of entire EC domains is not the primary response of PCDH15 to force. Instead, the response likely comprises a series of smaller unfolding events that stem from the unfolding of the inter-domain linkers and possibly parts of EC domains.

The Ca^{2+} concentration within the endolymph ranges from approximately 20 μM at the base to 40 μM at the apex²⁰. Furthermore, the local depletion of Ca^{2+} might be significant near an open transduction channel: at a distance of 7 nm, the concentration of Ca^{2+} could fall to half its maximal value. The length of a folded EC domain³⁰ is about 4.5 nm, so EC10, EC11, and the PICA domain could experience a significantly lower Ca^{2+} level: the behavior of PCDH15 in the distal domains might well lie between the results for physiological levels of Ca^{2+} and those in the ion's absence. In particular, for a Ca^{2+} concentration of 0-20 μM Ca^{2+} , PCDH15 could extend around 20-100 nm. The most extreme tip link extensions observed experimentally³⁷ are around 120 nm, but because mechanotransduction is very sensitive—even hair bundle deflections of 1 nm can produce a response—it is likely that the tip link ordinarily extends much less.

The V507D mutation yields significant unfolding even at a saturating concentration of Ca^{2+} , and unfolds to a still more striking extent in the absence of Ca^{2+} . Because the end-to-end distance at low force is far greater for the mutant dimer than for the native dimer, V507D is apparently misfolded at the baseline of 1 pN force. When the applied force is low, such as during the resting period between force-ramp cycles, the two partially unfolded strands of the dimer might tangle with each other, resulting in a misfolded protein that extends easily when force is reapplied. This behavior might occur because EC5 is more prone to unfolding due to the location of the mutation, which could then predispose the neighboring EC domains to unfold by disrupting the stability of the interdomain linkers. Furthermore, the refolding ability of V507D is significantly lower than that of the native protein at physiological and no Ca^{2+} concentrations for which the comparison is possible. If V507D is unable to refold on a timescale appropriate for normal

hearing, on the order of microseconds to milliseconds, a more compliant PCDH15 dimer might underlie a softer overall tip link (Figure 6). Insufficient tension applied to the mechanotransduction channels might then be the mechanism of deafness in people with this mutation. More specifically, without an influx of Ca^{2+} through transduction channels, a hair bundle undergoes remodeling, resulting in shorter stereocilia with abnormal tip shapes³⁸. Moreover, if transduction is abolished in inner hair cells, their innervation changes: they become re-innervated by inhibitory efferent neurons, which normally contact inner hair cells only before the onset of hearing³⁹. If V507D cannot convey the appropriate tension to transduction channels and thus prevents their opening, changes in stereociliary structure and synaptic connectivity could underlie deafness.

While the V507D point mutation disrupts the mechanics of PCDH15, individuals with this mutation retain normal equilibrium and vision, despite the expression of PCDH15 in the vestibule and eye. It is possible that the higher concentration of Ca^{2+} in the vestibular labyrinth allows mutated PCDH15 to function adequately, whereas the lower concentration of Ca^{2+} in the cochlea precludes this. It is also plausible that mutated protein can function adequately at the lower frequencies, less than 20 Hz, characteristic of the vestibular system⁴⁰, but cannot perform well at the higher frequencies, up to 20 kHz, detected by the cochlea². PCDH15 V507D might be able to refold on the timescale of low-frequency stimulation in the vestibular system, but not at the higher frequencies experienced in the cochlea. As a result, it is likely that the mutated PCDH15 cannot transmit the appropriate tension to the mechanotransduction channel, resulting in deafness in people carrying this mutation. A similar mechanism might underlie the hearing loss associated with many other mutations¹⁶ in PCDH15 and CDH23.

Because PCDH15 consists of repeating structural motifs, it is impossible to ascertain the specific structural origin of any unfolding event. It seems likely that, once a particular part of the molecule has unfolded, the neighboring regions become more vulnerable to unfolding, especially when Ca^{2+} -binding sites are disrupted: because the Ca^{2+} ions are coordinated by residues both in the linkers and at the edges of the neighboring domains, unfolding of a neighboring domain could disrupt one or more binding sites and liberate Ca^{2+} . The loss of the bound Ca^{2+} would then

predispose the region to further unfolding. Although reducing the force on the protein might allow refolding to occur, proper refolding might become impossible after excessive unfolding.

These results confirm that PCDH15 has the appropriate stiffness to form a component of the gating spring and that its physical properties can be modulated by Ca^{2+} . In the case of a hearing-loss mutation, PCDH15 unfolds much more frequently, is softer than the wild-type protein, and has impaired refolding ability, three features that would likely result in inappropriate tension conveyed to the transduction channels *in vivo*. The findings concerning the V507D hearing-loss mutation underscore how the tension conveyed to transduction channels is critical for normal hearing.

Acknowledgments

The authors thank Tobias Bartsch and Ahmed Touré for assistance with establishing and calibrating the experimental apparatus; Brian Fabella, Maria Vologodskaja, Anna Kaczynska, and Sanyukta Oak for technical assistance; and Vadim Sherman for high-precision engineering of experimental chambers. CMV was supported by NIH MSTP Grant T32GM007739 and NIDCD F30 fellowship 5F30DC020104-03 and XD by Rockefeller University Institutional Funds. AJH is an Investigator of Howard Hughes Medical Institute.

References

1. Gillespie, P. G. & Müller, U. Mechanotransduction by Hair Cells: Models, Molecules, and Mechanisms. *Cell* **139**, 33–44 (2009).
2. Eric Kandel, John Koester & Mack, S. *Principles of Neural Science*. (McGraw Hill/Medical, 2021).
3. Kazmierczak, P. *et al.* Cadherin 23 and protocadherin 15 interact to form tip-link filaments in sensory hair cells. *Nature* **449**, 87–91 (2007).

4. Assad, J. A., Shepherd, G. M. & Corey, D. P. Tip-link integrity and mechanical transduction in vertebrate hair cells. *Neuron* **7**, 985–994 (1991).
5. Zhao, Y. -d., Yamoah, E. N. & Gillespie, P. G. Regeneration of broken tip links and restoration of mechanical transduction in hair cells. *Proc. Natl. Acad. Sci.* **93**, 15469–15474 (1996).
6. Ahmed, Z. M., Riazuddin, S., Riazuddin, S. & Wilcox, E. R. The molecular genetics of Usher syndrome. *Clin. Genet.* **63**, 431–444 (2003).
7. Ahmed, Z. M. *et al.* Mutations of the Protocadherin Gene PCDH15 Cause Usher Syndrome Type 1F. *Am. J. Hum. Genet.* **69**, 25–34 (2001).
8. Astuto, L. M. *et al.* Genetic Heterogeneity of Usher Syndrome: Analysis of 151 Families with Usher Type I. *Am. J. Hum. Genet.* **67**, 1569–1574 (2000).
9. Kimberling, W. J. *et al.* Genetic Studies of Usher Syndrome. *Ann. N. Y. Acad. Sci.* **630**, 167–175 (1991).
10. Jaiganesh, A. *et al.* Zooming in on Cadherin-23: Structural Diversity and Potential Mechanisms of Inherited Deafness. *Structure* **26**, 1210-1225.e4 (2018).
11. Ge, J. *et al.* Structure of mouse protocadherin 15 of the stereocilia tip link in complex with LHFPL5. *eLife* **7**, e38770 (2018).
12. Choudhary, D. *et al.* Structural determinants of protocadherin-15 mechanics and function in hearing and balance perception. *Proc. Natl. Acad. Sci.* **117**, 24837–24848 (2020).
13. Oroz, J. *et al.* Nanomechanics of the Cadherin Ectodomain. *J. Biol. Chem.* **286**, 9405–9418 (2011).
14. Krebs, J. Calcium Biochemistry. in *Encyclopedia of Molecular Cell Biology and Molecular Medicine* (ed. Meyers, R. A.) mcb.200300010 (Wiley-VCH Verlag GmbH & Co. KGaA, 2006). doi:10.1002/3527600906.mcb.200300010.

15. Tobin, M., Chaiyasitdhi, A., Michel, V., Michalski, N. & Martin, P. Stiffness and tension gradients of the hair cell's tip-link complex in the mammalian cochlea. *eLife* **8**, e43473 (2019).
16. Bartsch, T. F. *et al.* Elasticity of individual protocadherin 15 molecules implicates tip links as the gating springs for hearing. *Proc. Natl. Acad. Sci.* **116**, 11048–11056 (2019).
17. Bartsch, T. F. *et al.* Measurement of hindered diffusion in complex geometries for high-speed studies of single-molecule forces. *Sci. Rep.* **11**, 2196 (2021).
18. Zakeri, B. *et al.* Peptide tag forming a rapid covalent bond to a protein, through engineering a bacterial adhesin. *Proc. Natl. Acad. Sci. U. S. A.* **109**, E690–E697 (2012).
19. Sotomayor, M., Corey, D. P. & Schulten, K. In Search of the Hair-Cell Gating Spring: Elastic Properties of Ankyrin and Cadherin Repeats. *Structure* **13**, 669–682 (2005).
20. Salt, A. N., Inamura, N., Thalmann, R. & Vora, A. Calcium gradients in inner ear endolymph. *Am. J. Otolaryngol.* **10**, 371–375 (1989).
21. Ikeda, K., Kusakari, J., Takasaka, T. & Saito, Y. The Ca²⁺ activity of cochlear endolymph of the guinea pig and the effect of inhibitors. *Hear. Res.* **26**, 117–125 (1987).
22. Boshier, S. K. & Warren, R. L. Very low calcium content of cochlear endolymph, an extracellular fluid. *Nature* **273**, 377–378 (1978).
23. Dionne, G. *et al.* Mechanotransduction by PCDH15 Relies on a Novel cis-Dimeric Architecture. *Neuron* **99**, 480-492.e5 (2018).
24. Rayner, L. E. *et al.* The Solution Structures of Two Human IgG1 Antibodies Show Conformational Stability and Accommodate Their C1q and FcγR Ligands. *J. Biol. Chem.* **290**, 8420–8438 (2015).
25. Alagramam, K. N. *et al.* Promoter, Alternative Splice Forms and Genomic Structure of Protocadherin 15. *Genomics* **90**, 482–492 (2007).

26. Araya-Secchi, R., Neel, B. L. & Sotomayor, M. An elastic element in the protocadherin-15 tip link of the inner ear. *Nat. Commun.* **7**, 13458 (2016).
27. Ainavarapu, S. R. K. *et al.* Contour Length and Refolding Rate of a Small Protein Controlled by Engineered Disulfide Bonds. *Biophys. J.* **92**, 225–233 (2007).
28. Sotomayor, M. Communication about extracellular cadherin domain sequences. (2021).
29. Ainavarapu, S. R. K. *et al.* Contour Length and Refolding Rate of a Small Protein Controlled by Engineered Disulfide Bonds. *Biophys. J.* **92**, 225–233 (2007).
30. Shapiro, L., Fannont, A. M., Kwong, P. D. & Thompson, A. Structural basis of cell-cell adhesion by cadherins. **374**, 11 (1995).
31. Doucette, L. *et al.* Profound, prelingual nonsyndromic deafness maps to chromosome 10q21 and is caused by a novel missense mutation in the Usher syndrome type IF gene PCDH15. *Eur. J. Hum. Genet.* **17**, 554–564 (2009).
32. Jumper, J. *et al.* Highly accurate protein structure prediction with AlphaFold. *Nature* **596**, 583–589 (2021).
33. Mirdita, M. *et al.* ColabFold: making protein folding accessible to all. *Nat. Methods* **19**, 679–682 (2022).
34. Mitchell, A. L. *et al.* MGnify: the microbiome analysis resource in 2020. *Nucleic Acids Res* (2019) doi:10.1093/nar/gkz1035.
35. Mirdita, M., Steinegger, M. & Soding, J. MMseqs2 desktop and local web server app for fast, interactive sequence searches. *Bioinformatics* **35**, 2856–2858 (2019).
36. Mirdita, M. *et al.* Uniclust databases of clustered and deeply annotated protein sequences and alignments. *Nucleic Acids Res* **45**, D170–D176 (2017).
37. Shepherd, G. & Corey, D. The extent of adaptation in bullfrog saccular hair cells. *J. Neurosci.* **14**, 6217–6229 (1994).

38. Vélez-Ortega, A. C., Freeman, M. J., Indzhukulian, A. A., Grossheim, J. M. & Frolenkov, G. I. Mechanotransduction current is essential for stability of the transducing stereocilia in mammalian auditory hair cells. *eLife* **6**, e24661 (2017).
39. Corns, L. F. *et al.* Mechanotransduction is required for establishing and maintaining mature inner hair cells and regulating efferent innervation. *Nat. Commun.* **9**, 4015 (2018).
40. Carriot, J., Jamali, M., Chacron, M. J. & Cullen, K. E. Statistics of the Vestibular Input Experienced during Natural Self-Motion: Implications for Neural Processing. *J. Neurosci.* **34**, 8347–8357 (2014).

Table

Construct	[Ca ²⁺]	Percentage of full refolding
Wild type	3 mM	—
	20 μM	84.2 ± 15.8
	0 M (1 mM EDTA)	62.9 ± 10.5
V507D	3 mM	82.2 ± 5.7
	20 μM	59.3 ± 8.0
	0 M (1 mM EDTA)	24.0 ± 16.2

Table 1. Full refolding by construct and condition. The percentage of cycles in which the dimer refolded fully are those that returned to state 1 or state 2 by the beginning of the subsequent cycle after an excursion to some higher state in the previous cycle. The wild-type PCDH15 at a saturating level of Ca²⁺, 3 mM, did not visit any state higher than state 2, so there are no data on complete refolding for that condition.

Figures and figure legends

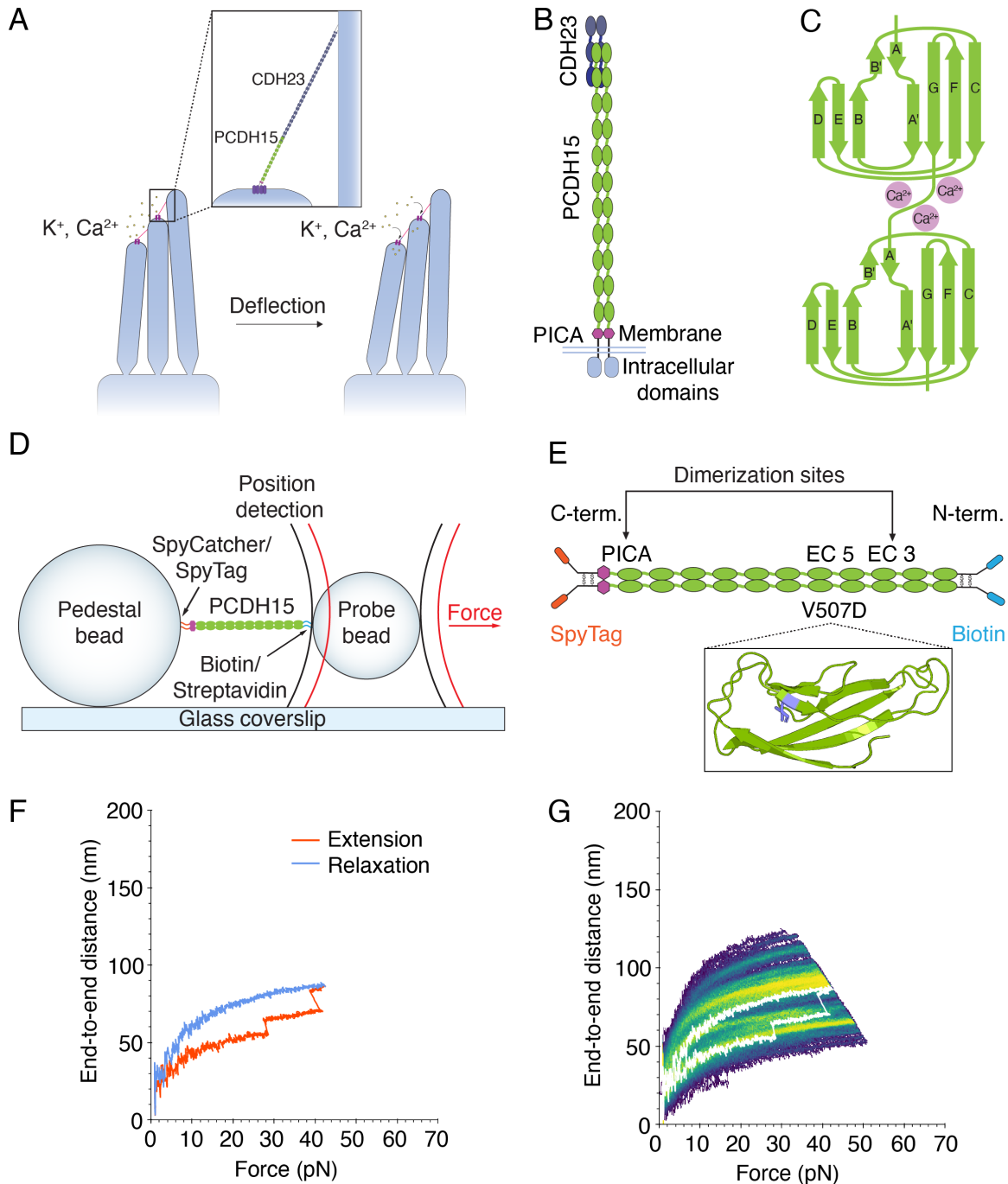


Figure 1. The structure of PCDH15 and measurements with an optical trap. (A) When stereocilia are deflected towards the tall edge of a hair bundle, the tip links (inset) connecting them stretch, opening the mechanotransduction channels (purple) atop each stereocilium and allowing the ions within the endolymph to flow into the cell, resulting in depolarization. (B) PCDH15 comprises 11 EC domains and a PICA domain at its carboxy terminus. PCDH15 binds

with CDH23 at its amino terminus in a handshake interaction. (C) EC domains are composed primarily of β -sheets. Ca^{2+} binding in the linker regions and at the edges of the domains stabilizes the structure against unfolding. (D) In our apparatus, the protein is tethered between two beads and two laser beams act on the probe bead to measure its position and exert force on it. (E) In our experimental construct, we maintained the dimerization sites in PCDH15 while adding two disulfide bonds to each end in addition to the distinct molecular tags at each end. The V507D construct was identical to the wild-type construct save for the insertion of the mutation in place of V507 (purple in inset). (F) A force-ramp experiment comprises the extension phase of the cycle, during which force is increased at a constant rate, and the relaxation phase of the cycle, during which force is decreased back to a minimum at the same constant rate. In these experiments, the minimum force is 1 pN and 2 s elapse between successive cycles. Unfolding events can be seen as sudden steps during an individual extension. (G) Repetition of a force-ramp cycle hundreds of times on the same protein molecule yields a heat map in which the brighter colors represent more highly occupied states. The heatmap superimposes both extension and relaxation phases of every cycle. The illustrative cycle from panel F is overlaid in white.

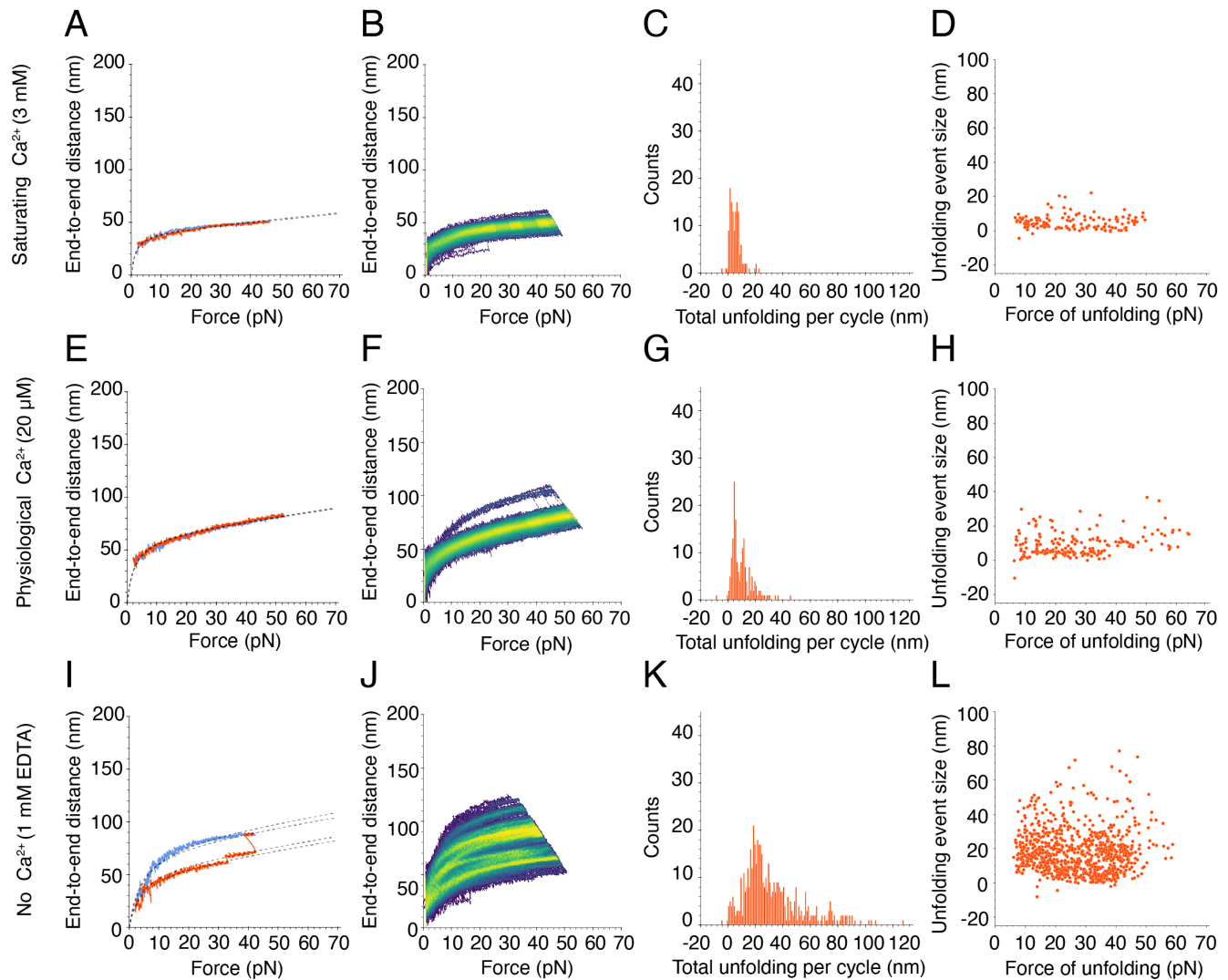


Figure 2. Force-ramp responses of wild-type PCDH15 at three Ca^{2+} concentrations. (A) At a saturating Ca^{2+} concentration of 3 mM, PCDH15 unfolds infrequently. The dashed line represents a fit of our model, Equation (1), to the extension and relaxation phases of the illustrative cycle. (B) In a heatmap for a saturating level of Ca^{2+} , 3 mM, the single bright branch indicates one highly occupied state that reflects the infrequent and small unfolding events. (C) The total unfolding length during the extension phases of all cycles in all datasets at 3 mM Ca^{2+} peaked at 1.8 ± 0.1 nm and 6.3 ± 0.2 nm (means \pm SEMs; $N = 5$ datasets; $n = 131$ events). (D) Many unfolding events occurred at forces below 10 pN at 3 mM Ca^{2+} . (E) At a physiological Ca^{2+} concentration of 20 μM , PCDH15 often does not unfold and is more extensible than under 3 mM Ca^{2+} in the same force range. (F) The illustrative heatmap has one bright branch indicative of the infrequent and small unfolding events at 20 μM Ca^{2+} . (G) At 20 μM Ca^{2+} , the total unfolding

per cycle was slightly greater than at a saturating level of Ca^{2+} , with peaks at 4.5 ± 0.1 nm and 11.5 ± 0.1 nm (means \pm SEMs; $N = 4$ datasets; $n = 172$ events). (H) At $20 \mu\text{M}$ Ca^{2+} , individual unfolding events with a mean of 4.6 ± 0.1 nm occurred predominantly at forces below 40 pN. (I) An illustrative force-ramp cycle in the absence of Ca^{2+} and in the presence of 1 mM EDTA shows a small unfolding event followed by a larger one. In this case, our protein model, Equation (1), is fitted separately to each segment demarcated by the unfolding events. (J) The numerous bright branches in the heatmap reflect the multiple preferred conformational states of PCDH15 in the absence of Ca^{2+} and in the presence of 1 mM EDTA. (K) The total unfolding per cycle peaked at 23.3 ± 0.6 nm (mean \pm SEM; $N = 6$ datasets, $n = 490$ events), but many larger events occurred in the absence of Ca^{2+} and in the presence of 1 mM EDTA. (L) There is no clear relationship between the size of individual unfolding events and the corresponding forces in the absence of Ca^{2+} and in the presence of 1 mM EDTA.

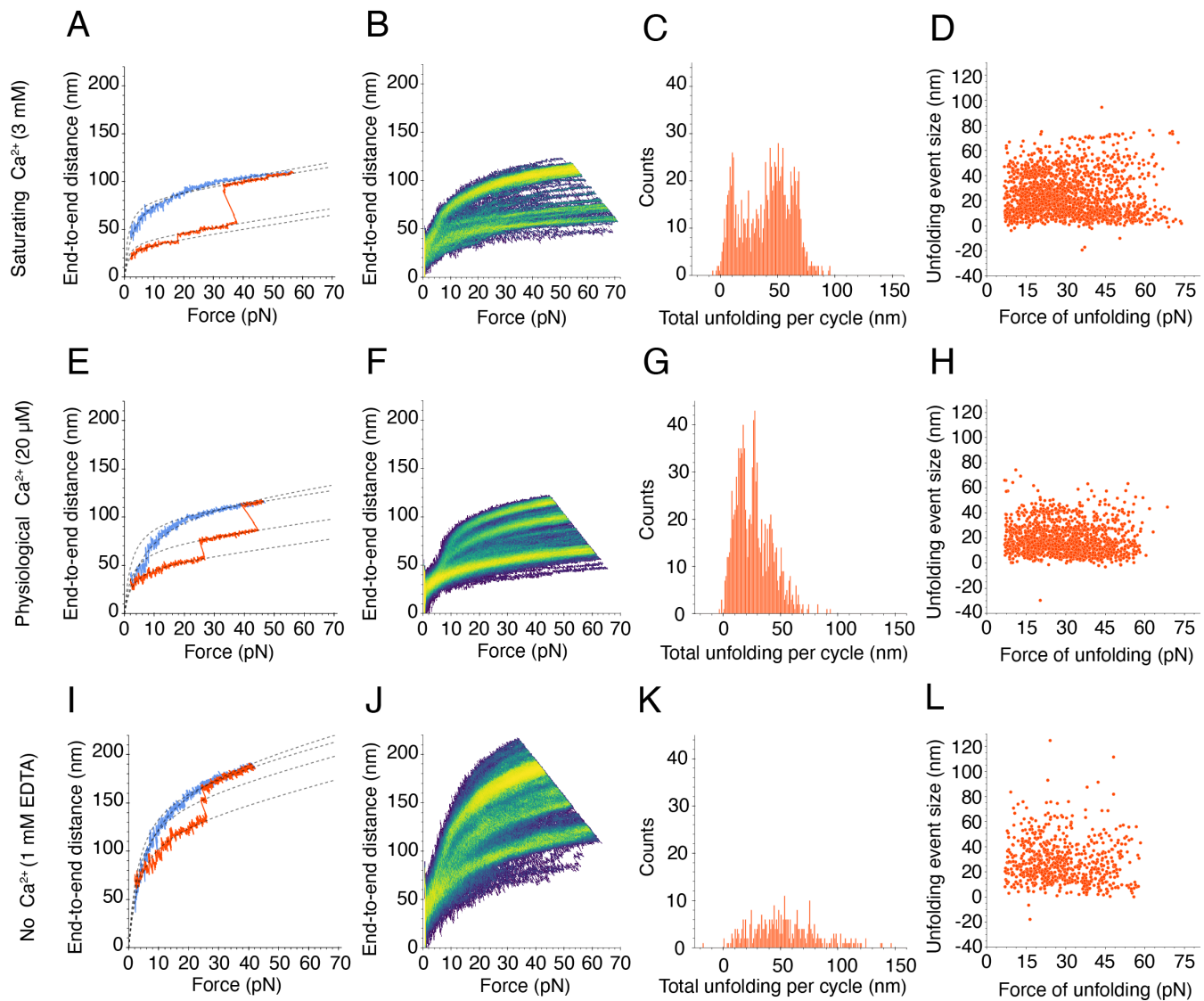


Figure 3. Force-ramp responses of V507D at three Ca^{2+} concentrations. (A) At a saturating level of Ca^{2+} , 3 mM, a subset of V507D molecules underwent only small unfolding events while another subset had more frequent unfolding (Figure S5A). The dashed line represents the fit of our model, Equation (1), to the segmented extension and relaxation phases. (B) The bright branches on the heatmap reflect the frequent unfolding seen in the individual cycle. (C) The frequency distribution of total unfolding length per cycle peaked around 8.8 ± 0.1 nm, 50.0 ± 0.2 nm, and 66.3 ± 0.1 nm (means \pm SEMs; $N = 24$ datasets; $n = 1889$ events). (D) As the size of the individual unfolding event got larger, the force of unfolding tended to be lower, with many events occurring around 30 pN. (E) At a physiological concentration of Ca^{2+} , 20 μM , frequent unfolding was seen on the single cycle level. (F) The unfolding seen in the individual cycles is

reflected by the bright branches on the exemplary heatmap. (G) The frequency distribution of total unfolding length per cycle during the extension phase peaked around 14.2 ± 0.2 nm, 27.3 ± 0.1 nm, and 39.4 ± 0.3 nm (means \pm SEMs; $N = 16$ datasets; $n = 1081$ events). (H) As at a saturating level of Ca^{2+} , the larger unfolding events were associated with smaller forces of unfolding. (I) When Ca^{2+} was absent, V507D extended easily, even without large unfolding events. (J) The bright branches on the illustrative heatmap reflect the unfolding behavior seen on the individual cycle level. The upper limits of the end-to-end distance at this level of Ca^{2+} exceeded those seen at higher concentrations of Ca^{2+} . (K) The frequency distribution of total unfolding length per cycle was unimodal, with one peak at 49.3 ± 1.4 nm (mean \pm SEM; $N = 4$ datasets; $n = 362$ events). (L) In the absence of Ca^{2+} , there was no clear relationship between the size of individual unfolding events and the forces at which they occurred.

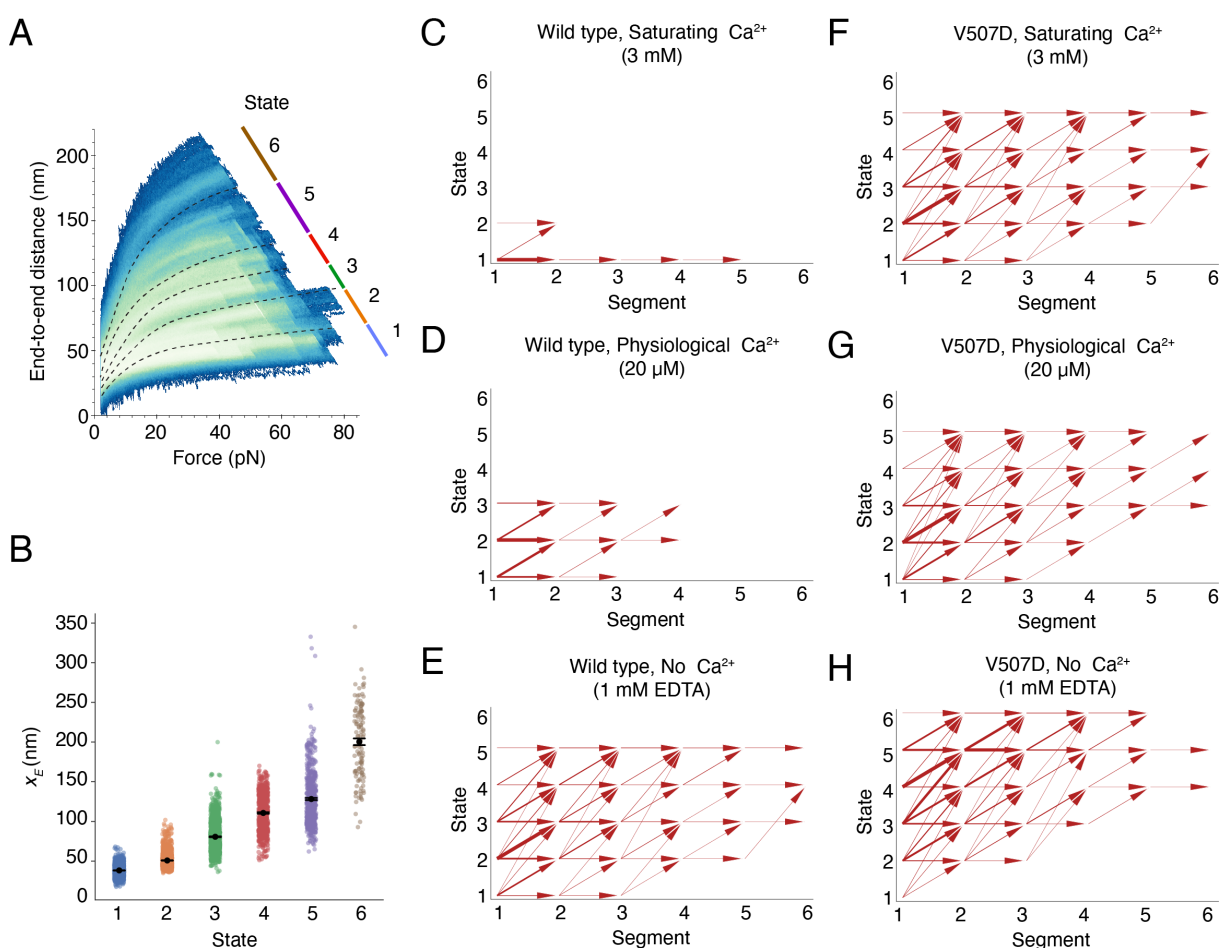


Figure 4. Clustering of force-ramp trajectories and inter-state transitions. (A) In a heatmap representing the relaxation-phase trajectories from all Ca^{2+} conditions and both PCDH15 constructs the lines with different colors demarcate the six conformational states. (B) The fitted x_E values for individual trajectories at different conformational states are shown in the scatter plot. The data represent means \pm SEMs. (C-H) Conformational transition maps summarize the trajectories of the two PCDH15 constructs at different Ca^{2+} concentrations. Segmented by conformational changes, the values along the abscissa denote individual segment within a trajectory in ascending order of force. The thickness of each arrow shaft denotes the frequency of a specific state transition. The horizontal arrows indicate conformational changes within a state, whereas the arrows pointing up and to the right denote conformational changes made between distinct states.

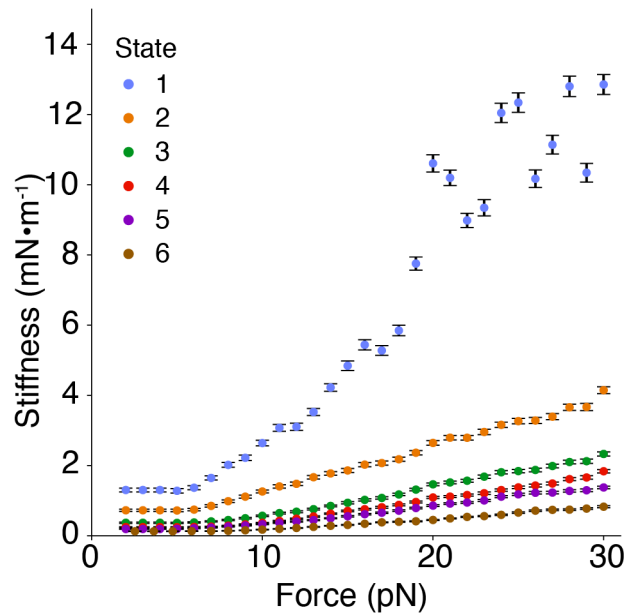


Figure 5. Entropic elasticity of PCDH15's states as a function of force. The stiffnesses of the states were calculated by finding the inverse of the mean slope of each state. In state 1, when PCDH15 is fully folded, the stiffness approached the enthalpic values above 15 pN. In states 2-6, in which PCDH15 had some unfolded portions, the stiffness of PCDH15 remained below the enthalpic limit. State 1 largely comprises trajectories of the wild-type protein at a saturating level of Ca^{2+} , whereas the remaining states predominantly contain trajectories at lower Ca^{2+} concentrations and from the V507D mutant. The results suggest that, under physiological conditions, the effective stiffness of PCDH15 is lower than its enthalpic limit of $40 \text{ mN}\cdot\text{m}^{-1}$ at a saturating concentration of Ca^{2+} . Error bars represent SEMs.

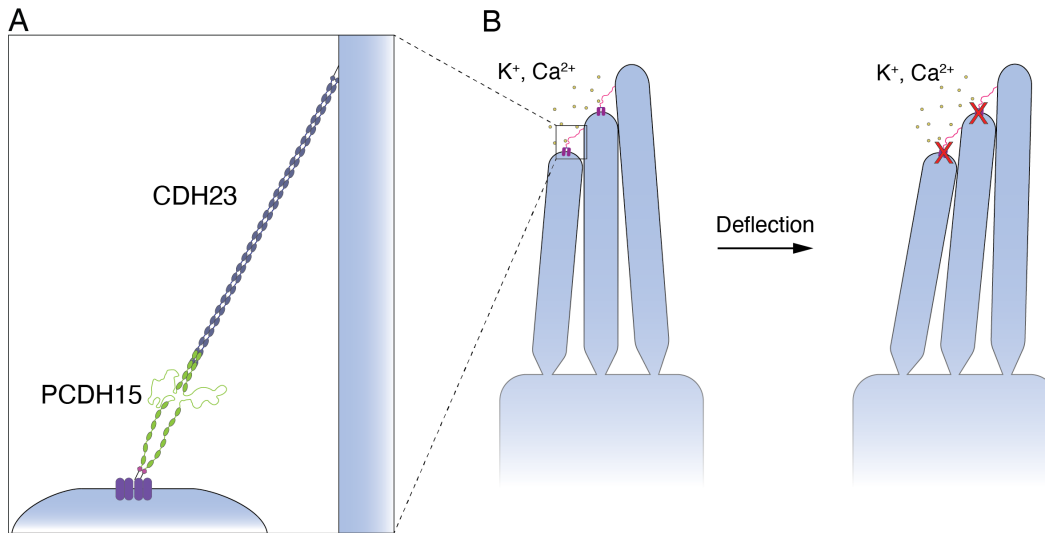


Figure 6. Proposed mechanism of deafness for mutated V507D. (A) Our data suggest that V507D is misfolded or partially unfolded over the physiological range of forces experienced in the cochlea. (B) If the tip links lack sufficient tension to open the mechanosensitive ion channels when stimulated, the ensuing deficit of Ca^{2+} in the stereocilia would cause their degeneration.